UNIVERSITY OF

KWAZULU-NATAL

FABRICATION OF HIGH EFFICACY SELECTIVE SOLAR ABSORBERS

By

Ngcali Tile

A dissertation submitted in fulfilment of the requirements for the degree of

Master of Science in Physics

School of Chemistry and Physics

Supervisor: Prof. Andrew Forbes

Co-supervisor: Dr. Kittessa Roro

March 2012

ABSTRACT

High efficiency tandem selective solar absorber materials of carbon in nickel oxide (C-NiO) composite were fabricated on an aluminium substrate using a simple and cost effective sol-gel process. The process involved preparation of carbon and nickel oxide precursor sols which were homogeneously mixed to form a final C-NiO precursor sol. The carbon precursor sol was prepared by dissolving sucrose (SUC) in 8 ml of distilled water. The NiO precursor sol was prepared by dissolving 7.5 g nickel acetate in 50 ml ethanol, then adding 6.3 g diethanol amine (DEA) to stabilise the solution followed by addition of a structure directing template of polyethylene glycol (PEG). The final C-NiO precursor sol was spin coated on pre-cleaned aluminium substrate to form thin films which were then heat treated in nitrogen ambient inside a tube furnace.

The final heat treatment temperature of the sols was determined by thermal studies using thermo gravimetric analytic (TGA) and differential scanning calorimetric (DSC) techniques. TGA and DSC studies of the final precursor sol showed that the weight loss of the precursors stabilised at around 450 °C.

The impact of the sol-gel process parameters namely heat treatment temperature, PEG content, SUC content as well as spin coating speed on the optical properties i.e. solar absorptance (α_{sol}) and thermal emittance (ε_{therm}) was investigated. It was found that the optical properties as well as photo-thermal conversion efficiency, $\eta = \alpha_{sol} - \varepsilon_{therm}$, improved with an increase in heat treatment temperature in the range studied (300-550 °C). This is in good agreement with the results obtained from thermo-gravimetric analysis which showed the weight loss of the precursor to stabilise around a temperature of 450 °C. Results obtained from the Raman studies showed a progressive increase in the graphitic domain in C-NiO samples with an increase in temperature. Heat treatment temperatures above 450 °C gave the best optical properties. Scanning electron microscopy (SEM) results showed that samples that did not have PEG in the precursor sol were compact and an addition of PEG in the precursor sol caused an increase in the size and density of pores in the films produced which affected the optical properties. As a result, the optical properties increased with an increase in PEG content from 0 g to 2 g then decreased with further increase in PEG content. It was found that addition of SUC of up to 8 g in the sol did not change the optical properties of the fabricated materials because SUC contributed little carbon to the final composite material. Further increase in SUC content resulted in materials with poor photo-thermal conversion efficiency.

An increase in spin coating speed did not change the absorptance of the materials but it improved their thermal emittance. The best spin coating speed was found to be 7000 RPM.

A solar absorptance of 0.81 and thermal emittance of 0.06 have been achieved for an optimum sample in this study yielding a photo-thermal conversion efficiency of 0.75. The optimum sample fabricated in this study showed superior optical properties compared to the widely used commercial solar absorber paint. This suggests that the C-NiO composite material has the potential for possible use as a selective solar absorber in a solar collector.

DECLARATION 1

The experimental work described in this dissertation was carried out at the Council for Scientific and Industrial Research, National Laser Centre, while registered with the School of Chemistry and Physics, University of KwaZulu-Natal, Durban, Westville, from February 2010 to February 2012, under the supervision of Professor Andrew Forbes and Dr Kittessa Roro.

This study represents original work by the author and has not otherwise been submitted in any form for any degree or diploma to any tertiary institution. Where use has been made of the work of others it is duly acknowledged in the text.

Signed: _____

Ngcali Tile

On this _____day of September 2012

As the candidate's supervisors we have approved this dissertation for final submission.

_____

Prof. Andrew Forbes

_____

Dr. Kittessa Roro

On this _____day of September 2012

DECLARATION 2 - PLAGIARISM

I, _____ declare that

1. The research reported in this thesis, except where otherwise indicated, is my original research.
2. This dissertation has not been submitted for any degree or examination at any other university.
3. This dissertation does not contain other persons' data, pictures, graphs or other information, unless specifically acknowledged as being sourced from other persons.
4. This dissertation does not contain other persons' writing, unless specifically acknowledged as being sourced from other researchers. Where other written sources have been quoted, then:
    a. Their words have been re-written but the general information attributed to them has been referenced
    b. Where their exact words have been used, then their writing has been placed in italics and inside quotation marks, and referenced.
5. This dissertation does not contain text, graphics or tables copied and pasted from the Internet, unless specifically acknowledged, and the source being detailed in the thesis and in the References sections.

Signed: ……

DECLARATION 3 - PUBLICATIONS

Peer-Reviewed Journal Papers:

K.T. Roro, **N. Tile**, B.W. Mwakikunga, B. Yalisi, A. Forbes (2012). *Solar absorption and thermal emission properties of Multiwall carbonnanotube/nickel oxide nanocomposite thin films synthesized by sol-gel process*, Materials Science and Engineering B 177,581– 587.

K.T. Roro, **N. Tile**, A. Forbes (2012), *Preparation and characterization of carbon/nickel oxide nanocomposite coatings for solar absorber applications*, Applied Surface Science 258, 7174– 7180.

K.T. Roro, B.W. Mwakikunga, **N. Tile,** B. Yalisi, A. Forbes (2012). *Effect of accelerated thermal ageing on the selective solar thermal harvesting properties of multiwall carbon nanotube/nickel oxide nanocomposite coatings*, International Journal of Photo energy Volume 2012, Article ID 678394.

International Conference Papers:

K.T. Roro, **N. Tile**, A. Forbes (2010). *Optical Properties of Selectively Absorbing C/NiO Nanocomposite Coatings*, International Workshop on Advanced Materials and Technologies for Global Energy and Environmental Changes, Pretoria, South Africa.

N. Tile, K.T. Roro, A. Forbes (2010). *Sol-gel fabrication and solar absorption properties of sol-gel C/NiO nanocomposite coatings*, International workshop on Advanced Materials and Technologies for Global Energy and Environmental Challenges, Pretoria, South Africa.

K.T. Roro, **N. Tile**, B. Yalisi, M. De Gama, T. Wittes, T. Roberts, A. Forbes *Selective solar absorber coating research at the CSIR (South Africa)* (published in Linköping University Electronic Press).

N. Tile, K.T. Roro, B. Yalisi, A. Forbes (2011). *Optimization of optical absorption properties of spectrally selective C-NiO composite coatings*, 11th International Conference on Frontiers of Polymers and Advanced Materials, Pretoria, South Africa.

B. Yalisi, K.T. Roro, **N. Tile**, A. Forbes (2011), *Properties of pulsed laser deposited C-NiO thin films*, 11th International Conference on Frontiers of Polymers and Advanced Materials, Pretoria, South Africa.

K.T. Roro, **N. Tile**, B. Yalisi, A. Forbes (2011). *Effects of heating temperature on the optical properties of sol-gel synthesized C/NiO nanocomposite thin films*, 11th International Conference on Frontiers of Polymers and Advanced Materials, Pretoria, South Africa.

K.T. Roro, B. Mwakikunga, **N. Tile**, A. Forbes, *Scanning and transmission electron microscopy investigation of Multiwall carbon nanotube/nickel oxide nanocomposite thin films*, Proc. Microsc. Soc. South. Africa 41(2011) 76.

National Conference Papers:

K.T. Roro, B.W. Mwakikunga, A. Forbes, **N. Tile**, B. Yalisi (2010). *Carbon nanotube/nickel oxide nanocomposite thin films for selective solar absorber*, 55th Annual Conference of the South African Institute of Physics, Pretoria, 27 September - 1 October, 2010. ISBN: 978-0-620-46211-2.

N. Tile, K.T. Roro, A. Forbes, B. Yalisi (2010). *Spray deposited C-NiO thin films for selective solar absorber applications*, 55th Annual Conference of the South African Institute of Physics, Pretoria, 27 September - 1 October, 2010. ISBN: 978-0-620-46211-2.

B. Yalisi, K.T. Roro, A. Forbes, **N. Tile** (2010). *Effect of film thickness on pulsed laser deposited optically selective solar absorber*, 55th Annual Conference of the South African Institute of Physics, Pretoria 27 September - 1 October, 2010. ISBN: 978-0-620-46211-2.

K.T. Roro, B. Yalisi, **N. Tile** B.W. Mwakikunga, T. Roberts, A. Forbes (2011). *Fabrication of MWCNT/NiO nanocomposite thin films for optically selective solar absorbers*, 56th Annual Conference of the South African Institute of Physics, 302.

N. Tile, K.T. Roro, B. Yalisi, T. Roberts, A. Forbes, *Carbon-Nickel Oxide Nanocomposite coatings: Preparation and characterization*, 56th Annual Conference of the South African Institute of Physics, 243.

B. Yalisi, K.T. Roro, A. Forbes, **N. Tile**, *Pulsed laser deposition of multiwall carbon nanotubes/NiO nanocomposite thin films,* 56th Annual Conference of the South African Institute of Physics, 240.

K.T. Roro, **N. Tile**, B. Yalisi, A. Forbes, *Multiwall carbon nanotube/nickel oxide nanocomposite coatings: Sol-gel deposition and characterization,* ASSAf-DST-NRF Second Annual South African Young Scientists' Conference, 26 September- 28 September 2011

ACKNOWLEDGEMENTS

I would like to express my sincere thanks to:

- My supervisors Prof. Andrew Forbes and Dr Kittessa Roro for their guidance and support throughout this project.
- The late Dr Gift Katumba who together with Prof. Andrew Forbes and others was instrumental in the establishment of the solar group at the National Laser Centre.
- All the current and former members of the solar group (Brian Yalisi, Mapule De Gama, Thobeka Wittes and Ted Roberts) at the NLC for sharing this learning journey with me.
- Prof. Ewa Wäckelgård at Angstrom Laboratories, Uppsala University, Sweden for giving the opportunity to use their world class equipments and hosting me during my visit to their laboratories.
- Council for Scientific and Industrial Research, National Laser Centre for the financial support and many learning opportunities.
- My friends (Aaron Malape and Mfundi Biyela), for the emotional support.
- And most importantly my family, particularly my mother Bukeka for the love and encouragement.

TABLE OF CONTENTS

ABSTRACT II
DECLARATION 1 IV
DECLARATION 2 - PLAGIARISM V
DECLARATION 3 - PUBLICATIONS VI
ACKNOWLEDGEMENTS IX
TABLE OF CONTENTS X
LIST OF FIGURES XIII
LIST OF TABLES XVII
CHAPTER 1 : INTRODUCTION 1

1.1 Solar thermal collectors 2

1.2 Spectrally Selective solar absorber surfaces 6

1.2.1 Understanding spectrally selective absorber surfaces 6

1.2.2 Optical characterisation of selective solar absorbers 8

1.2.3 Selective solar absorber efficiency criteria 9

1.3 Selective solar absorber designs 10

1.3.1 Intrinsic absorber 10

1.3.2 Semiconductor-metal tandem 10

1.3.3 Multilayer absorber 11

1.3.4 Solar transmitting coating/blackbody-like absorber 12

1.3.5 Textured surfaces 13

1.3.6 Metal-dielectric composite 13

1.3.7 Thickness sensitive selective solar paint coatings 14

1.4 Fabrication methods for selective solar absorbers 14

1.4.1 Vacuum thermal evaporation 15

1.4.2 Sputtering 15

1.4.3 Chemical vapour deposition 15

1.4.4 Electroplating 16

1.4.5 Anodisation and pigmentation 16

1.4.6 Spray pyrolysis....16
1.4.7 Spray coating....17
1.4.8 Sol-gel....17
1.5 Objective of the study....18
1.6 Thesis outline....19
References....20
CHAPTER 2 : SOL-GEL PROCESS....24
2.1 Sol-gel process chemistry....24
2.2 Advantages of the sol-gel technique....27
2.3 Sol-gel coating processes....27
2.3.1 Dip coating....28
2.3.2 Spin coating....28
2.3.3 Spray coating....29
2.4 C-NiO fabrication process....29
References....30
CHAPTER 3 : EXPERIMENTAL PROCEDURES AND TECHNIQUES....31
3.1 Sample preparation....31
3.1.1 Procedure....31
3.1.2 Substrate preparation....33
3.1.3 Spin coater....33
3.1.4 Furnace....34
3.2 Characterisation techniques....35
3.2.1 Thermal characterisation of the precursor sol....35

3.2.1.1 Thermo-gravimetric analysis (TGA) 35
3.2.1.2 Differential scanning calorimetry (DSC) 36
3.2.2 Material characterisation 36
3.2.2.1 Raman spectroscopy 36
3.2.2.2 Scanning X-ray photoelectron spectroscopy (SXPS) 38
3.2.2.3 Scanning Electron Microscope with Energy Dispersive Spectroscopy 40
3.2.3 Optical characterisation 43

References 46
CHAPTER 4 : RESULTS AND DISCUSSION 47

4.1 Thermal characterisation of the precursor sol 47

4.2 Elemental characterisation 49

4.3 Morphology of C-NiO 52

4.4 Effect of sol-gel process parameters on C-NiO 53
4.4.1 Introduction 53
4.4.2 Effect of heat treatment temperature 54
4.4.3 Effect of PEG content in the sol 59
4.4.4 Effect of Sucrose content 62
4.4.5 Effect of spin coating speed 67
4.4.6 Summary of optical results 69

4.5 Cost estimations 71

References 72
CHAPTER 5 : CONCLUSIONS AND FUTURE WORK 73

5.1 Conclusions 73

5.2 Future work 74

LIST OF FIGURES

Figure 1.1: Distribution of world annual solar energy [1.2].....1

Figure 1.2: Schematic figure of a flat-plate collector showing various components [1.9].....4

Figure 1.3: The solar irradiance distribution for AM 1.5 (black solid curve) according to ISO standard 9845-1 [1.12], emitted radiation of black bodies at 100, 200 and 300 °C (dashed curves) and reflectance for an ideal spectrally selective solar absorber surface (Thick solid red curve).....7

Figure 1.4: Schematic structure of an intrinsic solar absorber. 10

Figure 1.5: schematic structure of a semiconductor-metal tandem absorber. 11

Figure 1.6: Schematic structure of multilayer tandem solar absorber. 12

Figure 1.7: Schematic diagram of a solar transmitting coating. 12

Figure 1.8: Schematic design structure of surface textured solar absorber. 13

Figure 1.9: Schematic structure of metalic-dielectric composite. 14

Figure 2.1: Sequence of basic steps in the sol-gel procedure [2.1]. 24

Figure 2.2: illustration of various pathways in so-gel technology showing fundamental principles of sol-gel processing and products.....27

Figure 3.1: Flow chart of the steps in the procedure for the preparation of the samples.....32

Figure 3.2: Set-up for the preparation of the final solution. It is a normal wet chemistry lab and easy to use set-up. 32

Figure 3.3: A photograph of Chemat spin coater (Model KW-4A) used in this study.....33

Figure 3.4: Furnace set up including (a) tube furnace, (b) nitrogen bottle as well as (c) furnace control and temperature monitoring unit. 34

Figure 3.5: Typical TGA curve for a C-NiO precursor sol. 35

Figure 3.6: Energy level diagram showing the states involved in Raman signal. The Rayleigh signal is usually the most intense [3.4].....37

Figure 3.7: Raman spectrum of a sample prepared from a typical precursor sol and heat treated at 450 °C. The two peaks at 1375 cm^{-1} and 1585 cm^{-1} are D and G bands of carbon respectively (discussed in section 4.2.2). 38

Figure 3.8: A Typical XPS spectrum of a C-NiO sample with 8 g SUC in the precursor solution. 39

Figure 3.9: Schematic illustration of the signals generated during the primary electron beam – specimen interaction.....40

Figure 3.10: Characteristic X-ray emission by an atom [3.5].....41

Figure 3.11: Scanning electron microscopy image of a typical sample used in this study showing surface morphology. 42

Figure 3.12: Energy dispersive spectroscopy spectrum of a typical sample used in this study showing elements found in the sample.....42

Figure 3.13: Typical reflectance spectrum in the UV to far infra-red range for a C-NiO coating on aluminium substrate.....43

Figure 3.14: A schematic of an Infra-red data collection set-up showing a Michelson interferometer in a Fourier Transform Spectrometer. A gold coated integrating sphere attachment is for total reflectance measurements.....44

Figure 4.1: Typical TGA (red curve) and DTGA (blue curve) curve for a C-NiO precursor sol consisting of a mixture of ethanol, nickel acetate, DEA, PEG, water and brown sugar. 48

Figure 4.2: DSC curve of a typical C-NiO precursor sol. 49

Figure 4.3: EDS of a C-NiO heat treated at 450 °C showing peaks for carbon, nickel, oxygen and aluminium.....50

Figure 4.4: Raman spectrum of a sample prepared from a typical precursor sol and heat treated at 450 °C. The two peaks at 1375.55 cm^{-1} and 1585.58 cm^{-1} are D and G bands of carbon respectively.....51

Figure 4.5: Schematic structure of G-band taken from [4.4].....51

Figure 4.6: Scanning electron image of a C-NiO sample on aluminium substrate showing surface morphology. There are popped-up pores, un-popped-up pores as well as cracks on the surface. 52

Figure 4.7: Scanning electron image of C-NiO coating on an aluminium substrate revealing pores on the cross section of C-NiO layer. 53

Figure 4.8: Schematic of a cross section of a porous C-NiO coating on an aluminium substrate. 53

Figure 4.9: α_{sol} and ε_{therm} as function of heat treatment temperature of the precursor sol. 55

Figure 4.10: Typical reflectance spectra in the UV-Vis to far infra-red range for C-NiO coatings heat treated at different temperatures. The dashed line is a reflectance of an ideal selective solar absorber. 56

Figure 4.11: Optical images of samples heat treated at different temperatures showing an increase in the darkness with increase in heat treatment temperature. 56

Figure 4.12: Raman spectra of C-NiO coatings heat treated at different temperatures. The dashed vertical lines indicate the positions of the Raman features at 1350 and 1580 cm^{-1}. The spectra are vertically shifted for clarity. 57

Figure 4.13: Variation of photo-thermal conversion efficiency with heat treatment temperature of coated films. 58

Figure 4.14: α_{sol} and ε_{therm} as function of the PEG content of the precursor sol. 59

Figure 4.15: SEM images if samples prepared from precursor sols with different PEG contents showing an increase in pore size and density as the PEG increases 60

Figure 4.16: Schematic of multiple absorption of light within a structural pore of an absorber material. 61

Figure 4.17: Schematic of light reflection off the substrate leading to reduced light absorption. 61

Figure 4.18: Variation of photo-thermal conversion efficacy with PEG content of the precursor sol for films heat treated at 450 °C. 62

Figure 4.19: Reflectance spectra of coatings heat treated in air to form pure NiO, and the following heat treated in nitrogen: 0 g SUC, 8 g SUC, 12 g SUC and 16 g SUC and a decant of 16 g sol (sol left after the precipitation of solutes).....63

Figure 4.20: α_{sol} and ε_{therm} as a function of SUC variation with water fixed at 8 grams.....64

Figure 4.21: Variation of photo-thermal conversion efficiency of C-NiO coatings with sucrose content of the sol. Also included is results for decant of the precipitated sol which contained 16 g SUC. 66

Figure 4.22: α_{sol} and ε_{therm} as a function of spin coater speed. 67

Figure 4.23: Variation of photo-thermal conversion efficiency of C-NiO coatings coated at different spin coater speeds. 68

Figure 4.24: Scatter graph of absorptance and emittance for representative C-NiO samples used in this study. Other coatings are included for comparison. 69

LIST OF TABLES

Table 1.1: Some examples of developed selective solar absorber coatings fabricated by various techniques with their optimum optical properties. 18

Table 4.1: Base fabrication parameters used in this study 54

Table 4.2: Variation of C-NiO Raman parameters with heat treatment temperature. 58

Table 4.3: Chemical composition of C-NiO composite surfaces with 8 g sucrose from XPS. 65

Table 4.4: Chemical composition of C-NiO composite surfaces without sucrose from XPS. .66

Table 4.5: Fabrication parameters for the samples with highest average efficiency. 70

Table 4.6: Comparison of optical properties and photo-thermal conversion efficiency for various solar absorber coatings. 70

Table 4.7: Cost estimations for C-NiO coating compared with other wildly used coatings also included is the cost estimation of another sol-gel derived coating. The values are given in cost/m^2. 71

CHAPTER 1 : INTRODUCTION

Due to increase in energy cost, environmental concern, and a need for off-grid power systems, scientists and engineers have been working on ways to harness the energy from the sun. Solar energy is cheap, clean and widely available on the earth. The solar power reaching the earth is nearly four orders of magnitude greater than the power consumption globally. Out of the power of the sunlight reaching the surface of the earth, of 1.2×10^5 TW, we only use about 13 TW [1.1]. If all the energy of the sun striking the earth was converted to a useful form of energy with maximum efficiency, the annual energy consumption by humans (4.6×10^{20} Joule/year) could be satisfied within one hour [1.1]. Figure 1.1 shows the distribution of solar energy globally [1.2]. The African continent is amongst the regions that receive a high solar energy flux while the majority of its people are not able to meet their energy needs. Most African countries receive approximately 325 days of strong sunlight throughout the year. Southern Africa has amongst the world's greatest solar resource (for example 2900kWh/year in Upington, South Africa) and with a distribution such that the worst areas receive 2/3rds of the radiation in best areas. This clearly suggests a greater need in harvesting solar energy in order to meet the energy demands on the African continent.

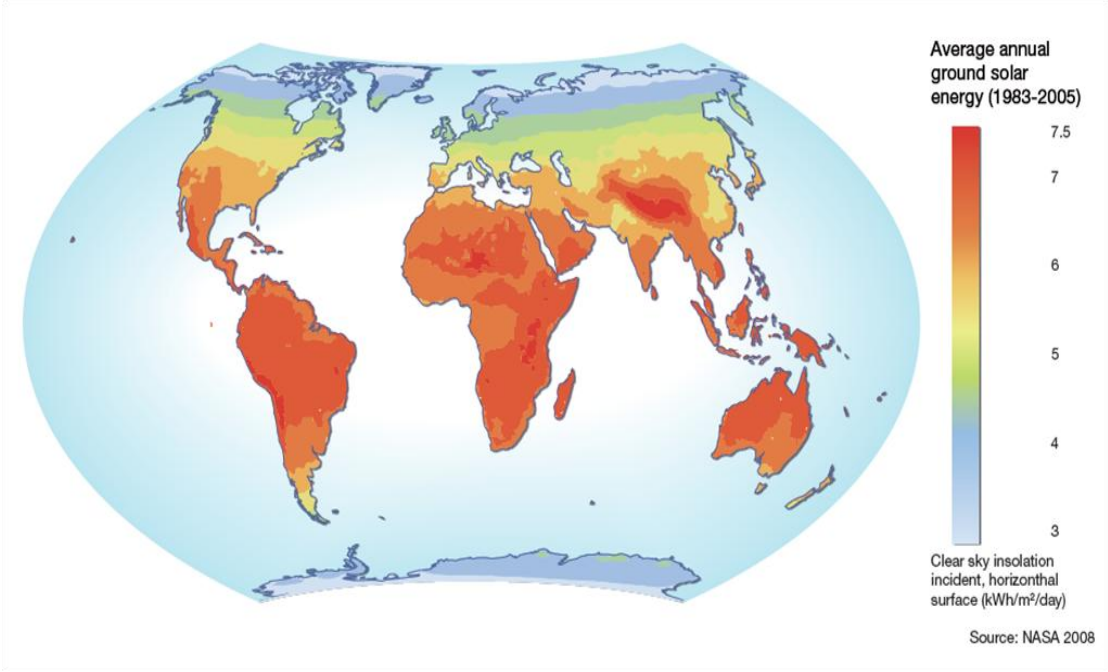

Figure 1.1: Distribution of world annual solar energy [1.2].

Solar energy can be converted into useful forms of energy through direct and indirect ways [1.3, 1.4]. Non-uniform heating of the earth's surface by solar energy causes air flow in the

atmosphere which can be used to generate wind power. Non-uniform heating of the water surface by the sun causes water circulation which can be used to generate hydroelectric/hydro mechanical power. In the biosphere, power from biomass and biogas uses solar energy through energy crops. These cases are regarded as indirect uses of solar energy [1.3, 1.4]. Direct use of solar radiation mainly consists of photovoltaic (PV) and photo-thermal energy conversion, and belongs to the type of technology in which solar energy materials play a key role. In PV technology, solar radiation is directly converted to electricity using semiconducting materials and finds many applications worldwide [1.5]. Photo-thermal devices actively convert solar radiation to heat energy in solar water heating and cooking technology.

Solar water heating technology is used as one of the most cost-effective means of heating water in the domestic sector [1.6]. It is also used in commercial sectors such as hotels, restaurants, etc. A typical solar water heating system consists of a solar collector and storage tank. The energy gain of a solar collector is the difference between the absorbed solar energy and the losses from the collector [1.7, 1.8].

An energy efficient solar collector should absorb incident solar radiation, convert it to thermal energy, and deliver the thermal energy to a heat transfer medium with minimum loss at each step. This means that solar absorption should be maximised and losses due to thermal emission should be avoided in order to maximise energy efficiency. A spectrally selective absorber surface is used to achieve this. The requirements for the optical properties of a spectrally selective solar absorber coating for high efficiency solar-thermal energy conversion are: a high spectral absorption (that means a low spectral reflectance) in the wavelength range of the solar radiation combined with low spectral absorption (that means a high spectral reflectance) in the wavelength range of the thermal radiation to reduce radiative heat losses [1.7]. To achieve this, the solar absorptance, α_{sol}, and thermal emittance, ε_{therm}, of the solar absorbing surface must be optimized.

1.1 Solar thermal collectors

Solar collectors are an important part of a solar water heating system. The collectors can be grouped into four main types: unglazed collectors, the concentrating collectors, the vacuum tube collectors, and the flat plate collectors [1.9].

The simplest and cheapest kind of solar collector is the unglazed type, which consists of the absorber without glazing or box. In such a system, thermal losses are high and it is therefore preferred for low temperature operation. The use of unglazed collectors for swimming pool heating is today the single most economically profitable solar collector application [1.9].

A concentrator collector consists of a parabolic reflector that concentrates incoming solar radiation onto an absorber. The advantage of this type of collector is the cost per unit area, since reflector material is less expensive than the absorber. Its added advantage is that it enables higher utilization of the low standing winter sun, as well as avoiding overheating in summer. However, only direct and not diffuse radiation can be focused on the absorber and to maximize the efficiency, an expensive solar tracking system is required [1.9].

In a vacuum tube collector the absorber is placed in an evacuated tube to make use of the insulating effect of vacuum, and the collector comprises several such tubes in a frame. The collectors cannot be integrated in the roof construction, but the absorber can easily be tilted inside the tube and does not need to follow the tilt of the roof. Due to the high vacuum that surrounds the outside of a tube, the heat loss to the outside by convection and conduction is greatly reduced. This results in high efficiency even at high temperature differences to the surroundings and at low solar irradiation. Vacuum tube collectors generally heat fluids to moderately high temperatures, up to 200 °C. Although vacuum tube collector efficiency is very high, they are expensive [1.9].

The flat-plate collector is more like the unglazed collector only it has a glazing and a box component in its design and is the dominantly used collector due to its simple and stable construction, well developed technique, low manufacturing costs, and easy integration onto building roofs etc. This system functions well for heating water to moderate temperatures of 35-100 °C and is suitable for domestic hot water heating [1.7, 1.9].

The absorber material studied in this work is aimed for an application on a flat plate collector because it is the most dominantly used type of collector.

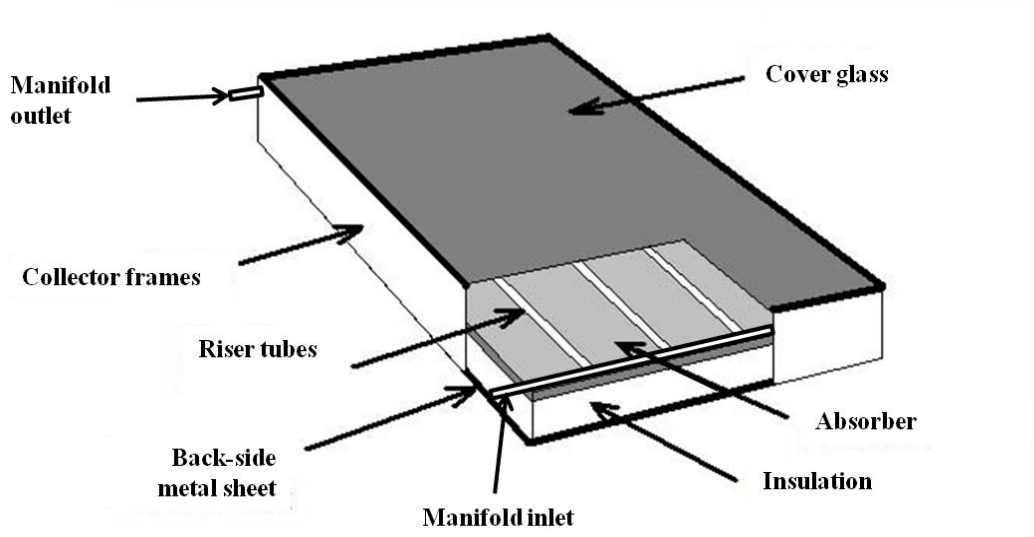

Figure 1.2: Schematic figure of a flat-plate collector showing various components [1.9].

Figure 1.2 shows a schematic design of a flat-plate collector showing various components. An absorber plate is placed in a metal case (comprises collector frames and backside metal sheet) which is insulated. Riser tubes carrying fluid (water) to be heated are running across the absorber from the manifold inlet to the manifold outlet. The case is covered by a glass with antireflection coating. The glass cover helps to reduce heat loss. In a flat-plate collector an absorber is the most important component because it is the part responsible for the conversion of solar radiation to heat. In a typical flat plate collector as the sun shines on the collector surface the sun's radiation passes through the glass cover and gets to interact with the absorber plate where it get converted to heat energy. A typical absorber consists of a highly reflective metal (aluminium, copper or stainless steel) sheet covered by a solar radiation absorbing layer.

The collector efficiency, η, is defined as the ratio between the power output from the collector, Q_u, and input power from the sun [1.7]:

$$\eta = \frac{Q_u}{A_c G_T}, \tag{1.1}$$

where A_c is the collector area and G_T is the total incident solar energy flux. The power output from the collector depends on the thermal energy losses from the collector. The simplified heat balance equation for a solar collector system is given by [1.10]:

$$Q_u = A_c[(\tau\alpha_{sol})_{eff} G_T - (HT + \varepsilon_{therm}\sigma T^4)], \quad (1.2)$$

where $(\tau\alpha)_{eff}$ is the effective transmittance-absorptance product (τ is the transmittance of the collector glass cover, while α_{sol} is the solar absorptance of the absorber surface), H is the coefficient of thermal losses by convection and conduction, ε_{therm} the coefficient of radiation losses (thermal emittance), $\sigma = 5.6697\times10^{-8}$ W m^{-2} K^{-4} is the theoretical Stephan-Boltzmann constant [1.7] while T is the absorber surface temperature. It shows that the useful energy output of a collector of area A_c is the difference between the absorbed solar radiation and thermal energy losses.

If the conduction and convection losses are minimised then the term HT in equation (1.2) tends to 0. Thus the heat balance equation becomes:

$$Q_u = A_c[(\tau\alpha_{sol})_{eff} G_T - \varepsilon_{therm}\sigma T^4]. \quad (1.3)$$

If the glass cover has a maximum transmittance in the solar wavelength range i.e. $\tau \approx 1$ then the heat balance of collector system is simplified to the following expression:

$$Q_u = A_c[\alpha_{sol} G_T - \varepsilon_{therm}\sigma T^4]. \quad (1.4)$$

The collector efficiency is thus given by:

$$\eta = \frac{Q_u}{A_c G_T} = \alpha_{sol} - \frac{\varepsilon_{therm}\sigma T^4}{G_T}. \quad (1.5)$$

It can be seen from equation (1.5) that the collector efficiency is dependent on the solar absorptance, α_{sol} and thermal emittance, ε_{therm} of the absorber surface. Therefore, for an efficient collector system, absorption of solar radiation incident on the absorber surface should be maximised, i.e. α_{sol} should be as high as possible and thermal radiative losses from the absorber surface be minimised, and i.e. ε_{therm} should be as low as possible. An absorber surface that is designed to have a high α_{sol} accompanied by low ε_{therm} is called a spectrally selective solar absorber or simply selective solar absorber.

1.2 Spectrally Selective solar absorber surfaces

1.2.1 Understanding spectrally selective absorber surfaces

The optical design of an absorber surface is determined by the spectral distribution of solar and thermal radiation. All heated objects emit electromagnetic radiation whose wavelength distribution and intensity are dependent on the temperature of the body. A blackbody is one that absorbs all wavelengths of the incident radiation and emits the maximum amount of energy for a given body temperature, *T*. It is an ideal surface whose emissive power, given by Planck's law [1.12] is used as a reference to compare with the properties of real surfaces. The spectral blackbody radiation is given by:

$$B(\lambda,T)=\frac{2\pi hc^2}{\left(e^{\frac{hc}{\lambda k_B T}}-1\right)\lambda^5}, \tag{1.6}$$

where h = 6.6260755×10^{-34} J s is the Planck's constant, c = 3×10^{8} m s^{-1} is the speed of light and k_B =1.3806488×10^{-23} J K^{-1} is the Boltzmann's constant. The total emitted energy can be obtained by integrating the Planck's spectrum over the whole wavelength range and result in Stephan-Boltzmann law for the total emitted energy for an ideal blackbody as:

$$B(T)=\sigma T^4. \tag{1.7}$$

As the temperature of the blackbody increases, the amount of the emitted energy increases and the peak power density shifts towards shorter wavelengths. The peak wavelength can be determined from the Wien's displacement law [1.7]:

$$\lambda_{max}\,T = 2897.8\ \mu\text{m K}, \tag{1.8}$$

where the constant 2897.8 μ m K is known as Wien's constant [1.12].

Terrestrial solar radiation G_T is spectrally confined between 0.3 and 2.5 μm wavelengths with the maximum solar radiation intensity at around 0.55 μm wavelength. The solar irradiance that reaches the earth's surface during a clear sky is shown in figure 1.3. This is adapted from the International Organisation for Standardization (ISO) for air mass 1.5 (AM1.5) [1.13, 1.14]. The spectral distribution of blackbody radiation at different temperatures is also included in figure 1.3. Temperatures between 35-100 °C correspond with the working

temperature of a flat plate collector and their spectral distribution is in the thermal infra-red (IR) range. It can be seen in figure 1.3 that spectral distributions of solar irradiance (solar spectrum) and blackbody at temperature 100 °C have their contribution in different wavelength ranges. It is therefore in principle possible for an absorber surface to absorb the maximum possible incident solar radiation, while not re-emitting the absorbed energy in the form of infrared radiation, if it is designed to have a high absorptance (low reflectance) in the solar spectrum and low emittance (high reflectance) in the thermal infrared. Such an absorber material is called a spectrally selective absorber. The reflectance of an ideal spectrally selective surface is included in figure 1.3 (red solid curve). It has a reflectance of zero in the solar wavelength range and unity in the thermal infrared wavelength range.

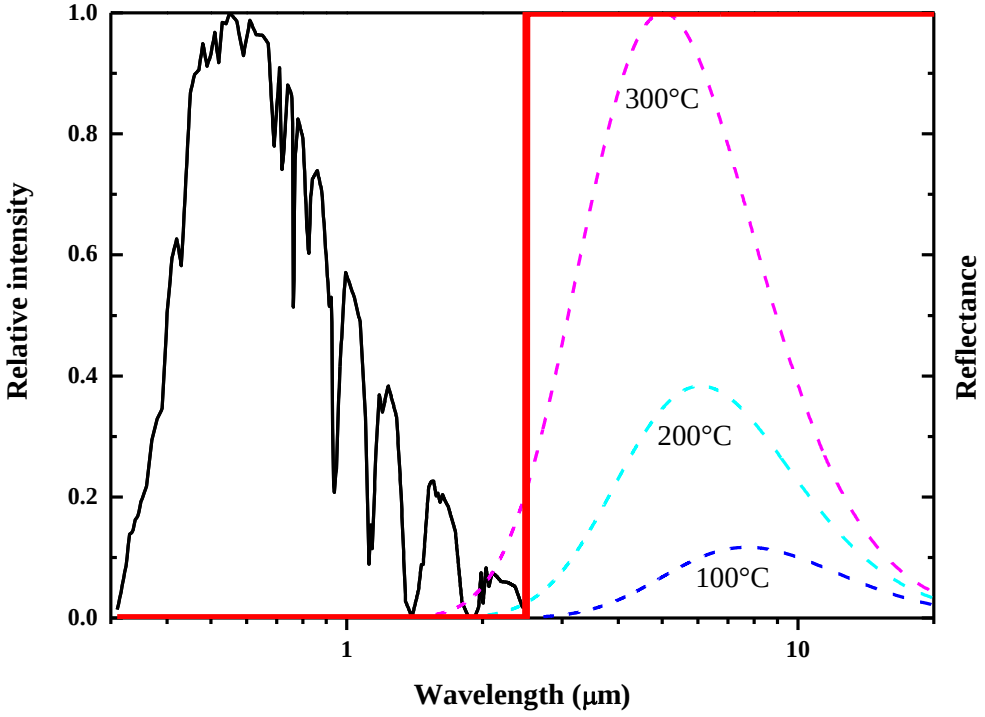

Figure 1.3: The solar irradiance distribution for AM 1.5 (black solid curve) according to ISO standard 9845-1 [1.12], emitted radiation of black bodies at 100, 200 and 300 °C (dashed curves) and reflectance for an ideal spectrally selective solar absorber surface (Thick solid red curve).

1.2.2 Optical characterisation of selective solar absorbers

The optical performance of a selective solar absorber material is characterised by its solar absorptance and thermal emittance. When radiation strikes a body, part of it is reflected, part is absorbed, and if the material is transparent, part is also transmitted. The fraction that is reflected is called reflectance, $\rho(\lambda)$, the fraction that is absorbed is called absorptance $\alpha(\lambda)$ and the fraction that is transmitted is called transmittance $\tau(\lambda)$. These fractions depend on the wavelength of the electromagnetic radiation and on the properties of the material and according to the law of the conservation of energy they should add up to 1 i.e.

$$\alpha(\lambda) + \rho(\lambda) + \tau(\lambda) = 1. \tag{1.9}$$

If one considers a radiation energy interchange when a body is placed in an isothermal enclosure and allowed to attain thermal equilibrium with the enclosure at temperature *T*, in order to avoid a violation of second law of thermodynamics which states that difference in temperature equilibrates in an isolated system, then according to Kirchhoff's law of radiation [1.7] spectral absorptance must be equal to spectral emittance i.e.

$$\alpha(\lambda) = \varepsilon(\lambda). \tag{1.10}$$

Equation (1.9) can now be written as

$$\alpha(\lambda) = \varepsilon(\lambda) = 1 - \rho(\lambda) - \tau(\lambda). \tag{1.11}$$

It is usual practice to measure the reflectance of the absorber material in order to determine its optical properties (i.e. solar absorptance and thermal emittance). For an opaque material the transmittance is zero thus spectral absorptance can be expressed in terms of the total reflectance as:

$$\alpha(\lambda) = \varepsilon(\lambda) = 1 - \rho(\lambda). \tag{1.12}$$

Solar reflectance measurements and infra-red reflectance measurements are usually performed in the wavelength ranges 0.3-2.5 μm and 2.5-20 μm respectively at near normal angle of incidence using standard spectrophotometers.

Normal solar absorptance α_{sol} can be found by weighing the spectral absorptance in the solar spectral range with spectral solar irradiance $G_T(\lambda)$ and integrating over the solar wavelength dependent spectrum to give [1.7]:

$$\alpha_{sol} = \frac{\int_{0.3\mu m}^{2.5\mu m} G_T(\lambda)(1-\rho(\lambda))d\lambda}{\int_{0.3\mu m}^{2.5\mu m} G_T(\lambda)d\lambda}. \tag{1.13}$$

The normal thermal emittance ε_{therm} is a weighted fraction between emitted radiation and Planck's black body radiation $B(\lambda,T)$ at a given temperature, T [1.7]:

$$\varepsilon_{th} = \frac{\int_{2.5\mu m}^{20\mu m} B(\lambda,T)(\lambda)(1-\rho(\lambda))d\lambda}{\int_{2.5\mu m}^{20\mu m} B(\lambda,T)d\lambda}, \tag{1.14}$$

where $B(\lambda,T)$ is given by equation 1.6. In this study the thermal emittance is determined for a temperature of 100 °C.

1.2.3 Selective solar absorber efficiency criteria

It was shown in section 1.1 that the photo-thermal conversion efficiency of the flat plate solar collector is dependent on the photo-thermal conversion efficiency of the absorber material. For an operating temperature, T = 100 °C (boiling temperature of water) and solar irradiance, G_T = 1000 W.m^2 the $\sigma T^4 / G_T$ term in equation 1.5 becomes approximately 1 i.e. the collector system has reached a steady state. Then equation 1.5 reduces to:

$$\eta = \alpha_{sol} - \varepsilon_{therm}. \tag{1.15}$$

This photo-thermal conversion efficiency will be the criteria used to evaluate the efficiency of materials fabricated in this study [1.15].

1.3 Selective solar absorber designs

In principle there are several ways of achieving selective solar absorbing surfaces. The choice of a selective solar absorber design depends on the operational temperature and application. An annotated bibliography of earliest (1955-1981) selective solar absorbing surfaces is reviewed by Nicklasson and Granqvist [1.16]. A review of mid to high temperature absorber materials up to year 2002 is found in ref [1.17] by Kennedy. According to Niklasson and Granqvist [1.18] and Kennedy [1.17], selective absorber surface coatings are categorised into six distinct types. These are: intrinsic absorber; semiconductor-metal tandem; multilayer absorber; selectively solar-transmitting coating on a blackbody-like absorber, textured surfaces and metal-dielectric composite coating. There are also selective paint coatings. In practice useful absorbers are based on two or more layers with different optical properties.

1.3.1 Intrinsic absorber

Intrinsic absorbers consist of a single material having intrinsic properties that result in a natural spectral selectivity. The structure of an intrinsic absorber is shown in figure 1.4. It consists of an intrinsic selective absorber material on a conducting substrate. There are some materials in nature that have moderate selectivity such as various semiconductors or transition metals [1.19]. These materials have been found not to show sufficient selective properties for spectrally selective applications. This is because the crossover from low to high reflectance occurs at too short wavelengths or that the slope at the transition wavelength is not sufficiently steep. Research in intrinsic absorbers has therefore not been very fruitful. The most notable intrinsic absorber materials CaF_2 and ZrB_2 have been investigated by Pellegrini [1.20] and Randrich and Allred [1.21], respectively.

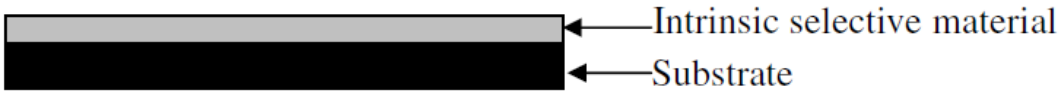

Figure 1.4: Schematic structure of an intrinsic solar absorber.

1.3.2 Semiconductor-metal tandem

Spectrally selective semiconductor coatings can be obtained by depositing a semiconductor, which has a low band gap so that it absorbs the solar radiation, on a highly infrared reflecting

metal substrate forming a semiconductor-metal tandem. A schematic structure of a semiconductor-metal tandem absorber is depicted in figure 1.5. A semiconductor coating material absorbs photons with energies greater than its band gap as a result raising the material's valence electrons into the conduction band. Photons with energies less than the band gap energy are transmitted through the coating unaffected. Common semiconductors have band gaps that are too large, corresponding to wavelengths that are too short. Lead sulphide has been found to be a suitable semiconductor with a band gap of 0.4 eV [1.22]. The disadvantage of using lead sulphide is that it is very poisonous, both for humans and for the environment. Most of the useful semiconductors usually have high refractive indices, which tend to yield high front reflection losses leading to low absorptance. However, the absorptance of a semiconductor coating can be enhanced by applying anti-reflection (AR) coatings [1.23]. Seraphin [1.24] has investigated $SiO_2/Si_3N_4/Si/CrO_3/Ag/CrO_3$ semiconductor coatings on steel and obtained solar absorptance of 0.85 and the thermal emittance of 0.07 at 500 °C. However, the low mechanical strength, low thermal conductivity and high cost of semiconductors makes them unsuitable for the entire collector material [1.25].

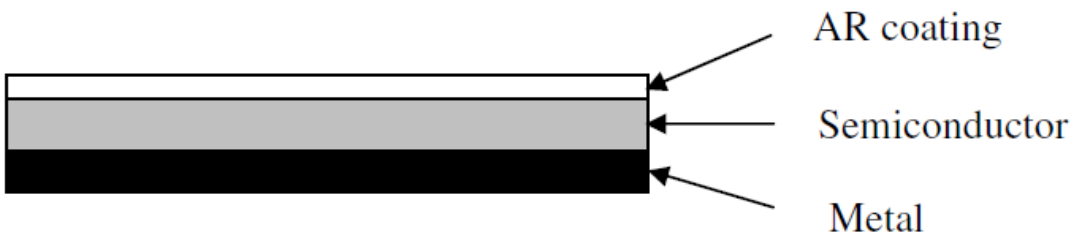

Figure 1.5: schematic structure of a semiconductor-metal tandem absorber.

1.3.3 Multilayer absorber

A multi-layer absorber shown schematically is figure 1.6 can be constructed out of several alternate layers of semitransparent metal and dielectric materials with an AR layer often put on top. A thin semitransparent reflective metallic layer D separates two quarter-wave dielectric layers, C and E. The bottom reflecting layer D has high reflectance in the IR region and is slightly less reflective in the visible region. The thickness of this dielectric determines the shape and position of the reflectance curve. An additional semitransparent thin metallic layer B further reduces the reflection in the visible region, and an additional dielectric layer A increases the absorption in the visible region and broadens the region of high absorption. One interesting example of a multilayer absorber is a triple layer of $Al_2O_3/Mo/Al_2O_3$, which has been produced by large area sputtering technology [1.18].

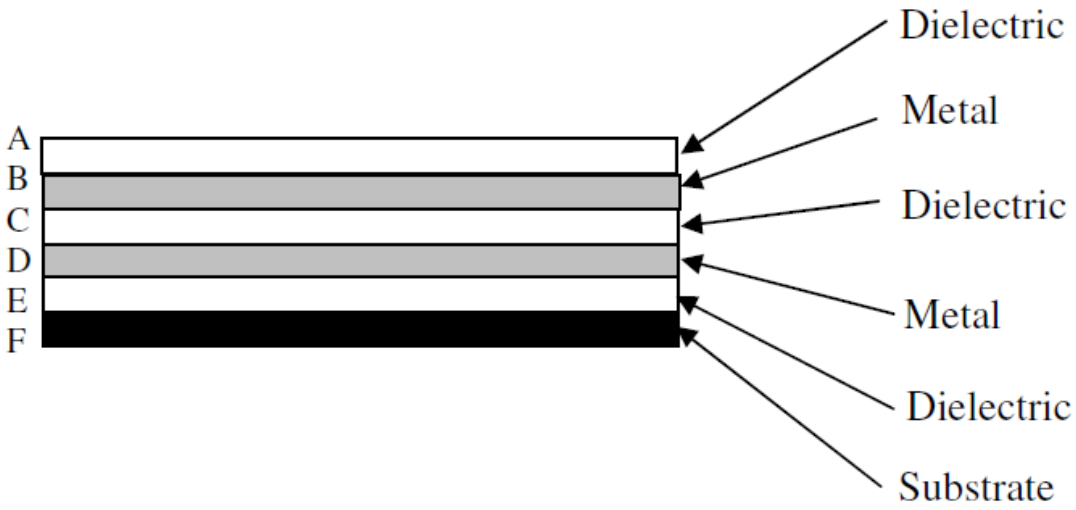

Figure 1.6: Schematic structure of multilayer tandem solar absorber.

1.3.4 Solar transmitting coating/blackbody-like absorber

A solar transmitting coating can be made by depositing a highly doped semiconductor such as SnO_2:F or ZnO:Al over an absorber with a proven long-term durability [1.26]. This structure is also called heat-mirror on black substrate absorber and is shown schematically in figure 1.7. The coating has to be highly reflective in the infrared wavelength interval and at the same time transparent to wavelengths in the solar spectrum i.e. a heat mirror. Some low-temp flat plate collectors have used black enamel as an absorber material [1.17].

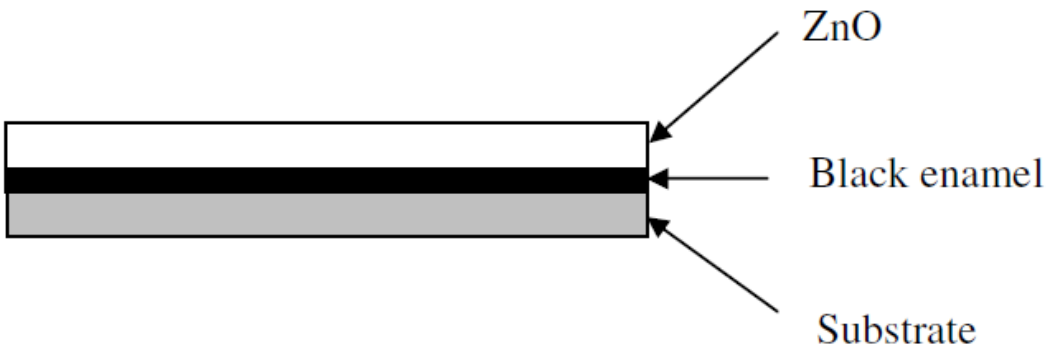

Figure 1.7: Schematic diagram of a solar transmitting coating.

1.3.5 Textured surfaces

Textured surfaces are produced by creating texture of suitable scale on a highly reflecting metal substrate like aluminium, copper or steel. A schematic design of a textured surface absorber is shown in figure 1.8. Textured surfaces can produce high solar absorptance by multiple reflections among needle-like, dendritic, or porous microstructures [1.22]. For long wavelength radiation, the surface looks fairly smooth thereby acting like a poor radiator of thermal energy (low ε_{therm}). A dendrite structure of rhenium, tungsten and nickel made by chemical vapor deposition and textured copper, nickel, and stainless steel made by sputter etching are examples of textured metal surfaces [1.27-1.31]. Al-Si alloy produced by simultaneous evaporation of the constituents from two electron-beam sources on a glass substrate and chemically etched in a NaOH solution form an irregular textured surface [1.32]. The textured surface is due to the preferential etching of the aluminum phase, which gives a dark appearance for an appropriate etching time. Konttinena *et al* [1.33] produced $C/Al_2O_3/Al$ surface by using a mechanical grinding method on aluminium.

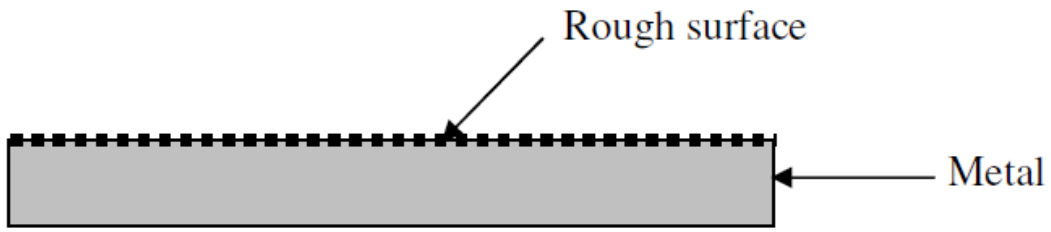

Figure 1.8: Schematic design structure of surface textured solar absorber.

1.3.6 Metal-dielectric composite

A metal-dielectric or cermet absorber consists of metal particles embedded in a dielectric matrix deposited on a highly infrared reflecting metal substrate [1.34]. A schematic structure of a metal-dielectric composite is shown in figure 1.9. The particles are usually transition metals embedded in an oxide matrix. The particles could either be uniformly distributed in the matrix or gradient index with decreasing content of the particles towards the front surface of the coating.

The metal-dielectric concept offers a high degree of flexibility because the solar selectivity can be optimised by proper choice of constituents, coating thickness, particle concentration,

size, shape and orientation [1.35, 1.36]. The solar absorptance can be boosted by a suitable choice of substrates, and AR layers. Due to the above mentioned reasons, metal-dielectric composites are the most useful design material in solar-thermal applications. Such composite

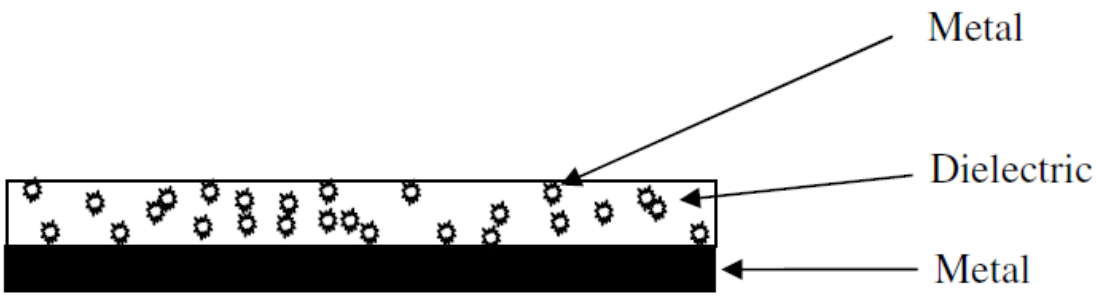

Figure 1.9: Schematic structure of metalic-dielectric composite.

coatings are widely studied [1.36-1.53] and they can be produced by a variety of techniques such as electroplating, anodization, inorganic colouration of anodized aluminium, chemical vapour deposition (CVD) and co-deposition of metal and insulator by evaporation, and painting. The material being studied in this work, a composite of carbon in a nickel oxide dielectric matrix (C-NiO) falls in this category and is produced by sol-gel technique.

1.3.7 Thickness sensitive selective solar paint coatings

Paint coatings can also be classified as the tandem type which consists of absorbing particles uniformly distributed in a matrix deposited on a metal substrate. Absorber particles are inorganic pigments while the matrix is a resin. It is a cheap and simple way of creating a solar selective absorbing surface [1.54]. The disadvantage in using this kind of absorber is the normal thermal emittance value is very high compared to thin film metal-dielectric compounds. Examples of solar absorbing paints that are on the market are Solarect-Z and SolkoteHI/SORB-IITM [1.55]. These are used for low temperature flat plate collectors.

1.4 Fabrication methods for selective solar absorbers

Various techniques generally used for fabrication of thin films are used for the fabrication of solar absorber materials.These include sputtering [1.56], chemical vapour deposition [1.57], physical vapour deposition [1.58], solution chemistry [1.48-1.54] etc.

1.4.1 Vacuum thermal evaporation

In vacuum thermal evaporation a material is converted thermally in vacuum into individual atoms or molecules which are then condensed onto a substrate. High vacuum is necessary to provide large mean free paths for the evaporation of species [1.56]. The microstructure and surface morphology of the resultant coating depends on the quality of the vacuum, evaporation rate, substrate type and temperature, distance between substrate and vapour distance, etc. This technique allows for precise control of thickness. The major disadvantage of this technique is that it requires expensive vacuum equipment. Another disadvantage is the difficulty to maintain the stoichiometry in the evaporation of multicomponent alloys and some compounds [1.56, 1.58].

1.4.2 Sputtering

In sputtering, atoms of a target material are ejected by bombardment with energetic particles. There are different types of sputtering and these include DC, RF, ion beam and magnetron sputtering. Due to availability of these different sputtering types many material types can be sputter deposited. Multicomponent composite films can be deposited by co-sputtering [1.56]. An advantage of sputtering is that it yields hard and adherent coatings that have the same composition as the target material. The disadvantage of this technique is that sputter coaters have very high purchase and running cost.

1.4.3 Chemical vapour deposition

In chemical vapour deposition (CVD) constituents of the vapour react chemically to form a solid film as a solid phase reaction product which condenses on the substrate. Chemical reaction can be activated by various means such as heat, high frequency electrical fields, light or catalytic action of the substrate [1.58]. One of the advantages of this technique is that it can form coatings which are thin, hard and adherent to the substrate. Its disadvantages are that it is difficult to control thickness uniformity of the coatings and that the reactive gases used for the deposition and the reaction by-products formed in the process are usually toxic.

1.4.4 Electroplating

Electroplating is a plating process in which metal ions in a solution bath are moved by an electric field to coat an electrode. The process uses electrical current to reduce cations of a desired material from a solution and coat a conductive object with a thin layer of the material, such as a metal. The microstructure, topography and composition of the coating depend on electroplating parameters such as acidity of the solution, current density, deposition time and bath temperature. The major advantage of this technique particularly for selective absorber coatings is that it is suitable for large area production. Its disadvantage is that the numerous process parameters of the technique make it difficult to reproduce and control the coatings. Another disadvantage is that it is limited to coating of conducting substrates only.

1.4.5 Anodisation and pigmentation

Anodisation is an electrolytic oxidation process in which a metal is used as an anode in a suitable electrolyte so that when an electric current is passed through the electrolyte, the metal surface is converted to its oxide. It is possible to grow a porous anodic oxide film by choosing an appropriate electrolyte and the correct operating conditions [1.59]. A black colouration of the porous oxide layer may be achieved by alternating current (a.c.) electrolysis in an appropriate metallic solution which is called the pigmentation stage. The final particles are embedded in the pores of the anodic layer. The properties of the coating depend on selected operating parameters such as composition of electrolyte, concentration, acidity, temperature and time.

1.4.6 Spray pyrolysis

Spray pyrolysis is spraying of droplets of an aqueous solution onto a heated substrate. The solution contains soluble salts of the constituent atoms of the desired compound. The droplets reaching the substrate undergo pyrolytic decomposition to form a single crystalline or a cluster of crystallites of the desired product. The heated substrate provides the thermal energy for decomposition and subsequent recombination of constituent species to form a thin film after going through sintering and recrystallisation. Excess solvent and other by-products escape in vapour phase [1.58]. The components of a spray pyrolysis set up are deposition chamber, spray nozzles, carrier gas and flow meters, thermocouple, substrate heater temperature controller. The spray nozzle enables the atomisation of the chemical solution into fine droplets with the help of the carrier gas. The solvent helps to carry the reactants and to

distribute them uniformly over the substrate. The properties of the coatings deposited by this technique depend on the process parameters such as substrate temperature, solution and gas flow rates, solution concentration and solution volume [1.58]. Advantages of this technique are that it is cheap and suitable for large scale production of coatings. Its disadvantage is that the substrate needs to remain inert at the spray temperature and sometimes corrosive atmosphere.

1.4.7 Spray coating

In spray coating a device sprays a coating through the air onto a surface using a combination of compressed air and a coating to atomise and direct coating particles towards a substrate [1.60]. It is a well known technique that is easy to use, does not require complicated instruments and is used in industries such as automotive. In the solar thermal industry it has been adapted to spray coating of ordinary black paints and thickness sensitive spectrally selective coatings [1.61, 1.62] onto various substrates. The major advantage of spray coating technique is that it can be used in large scale production and can be applied to substrates of various shapes. The material consumption per unit area of coating is relatively low therefore its cost per unit area is also very low. Its biggest drawback is that it is difficult to get coatings of uniform thickness.

1.4.8 Sol-gel

The sol-gel process involves dissolving a molecular precursor in a liquid solvent forming solid in liquid dispersion (sol) which is followed by formation of solid network filled with the liquid (gel). It is generally used for fabrication of various glassy materials, structures as well as thin films. More information about the sol-gel technique is presented in chapter 2.

Some examples of various composite selective absorbers fabricated by various techniques are given in table 1.1. Also included in the table are some practical commercial absorber coatings and some commercial paints. This table also gives the optimum optical properties (absorptance and thermal emittance), description, and the level of development (laboratory or commercial) for these coatings. It can be seen in the table that a great deal of progress has been made to obtain solar absorber coatings with good selectivity over the years.

Table 1.1: Some examples of developed selective solar absorber coatings fabricated by various techniques with their optimum optical properties.

Researcher/manufacturer	Technique	Level of development	Structure	α_{sol}	ε_{therm}	η
Fan [1.63]	R.F Sputtering	Lab.	Au-MgO	0.93	0.09	0.84
Energie solaire [1.64]	Electroplating	Commercial	Cr-Cr_2O_3 (Black chrome)	0.97	0.12	0.85
Inal [1.64]	RF sputtering	Lab.	Cr-Cr_2O_3	0.92	0.08	0.84
Sunselct [1.65]	DC magnetron sputtering	Commercial	CrN-Cr_xO_y	0.93	0.07 (100 °C)	0.86
Luz [1.66]	R.F Sputtering	Commercial	Mo-Al_2O_3	0.96	0.1 (350 °C)	0.86
Solel [1.17]	R.F Sputtering	Commercial	W-Al_2O_3	0.96	0.16	0.8
McKenzie [1.67]	Sputtering	Lab.	Cu-Al_2O_3	0.9	0.05	0.85
Techno term [1.68]	Sputtering	Commercial	Black nickel	0.95	0.13	0.82
Techno term[1.69]	Electroplating	Lab.	Graded Ni-Al_2O_3	0.85	0.08	0.77
Sunstrip [1.70]	Reactive sputtering	Commercial	Graded Ni-NiO_x	0.96	0.1	0.86
Anderson [1.71]	Electroplating	Lab.	Ni-Al_2O_3	0.96	0.2	0.76
Showa Aluminium[1.72]	Electroplating	Commercial	Ni-Al_2O_3	0.93	0.13	0.8
A. Vila [1.73]	Spray pyrolysis	Lab.	Co_3O_4/Ni	0.89	0.50	0.39
Katumba [1.51]	Sol-gel	Lab.	C-SiO_2	0.88	0.44	0.44
Bostrom [1.48]	Sol-gel	Lab.	Ni-Al_2O_3 with AR coating	0.97	0.06	0.91
Solerect-Z	Spray Painting	Commercial	Siloxane resin-$FeMnO_x$P320	0.92	0.25	0.67
Solkote [1.55]	Spray painting	Commercial	Silicone resin, xylene and some oxides	0.93	0.25	0.68

1.5 Objective of the study

An efficient solar thermal collector system requires a spectrally selective solar absorber. Other requirements for a spectrally selective absorber is that it should be relatively cheap i.e. it should cost a fraction of the whole solar collector and must be easy to apply on large scale substrates. The production of paint coatings is regarded as a cheap and easy technique for making selective solar absorber materials [1.54, 1.55] and they can also be applied at large scale. However, their thermal emittance values are very high compared to thin film metal-dielectric compounds. Metal-dielectric composites make favourable candidates for study as spectrally selective absorbers because they allow a great deal of flexibility [1.35, 1.36] (see section 1.3.6). Of the available deposition techniques, sol-gel technique has some advantages over a number of some of these techniques (see section 2.2) in that it is a relatively cheap technique that is easy to use and can be adapted to technologies that allow for large scale

production. The optical properties of a material fabricated by sol-gel technique depend on the sol-gel process parameters.

Katumba *et al* [1.50-1.53] have managed to fabricate selective solar absorber coatings of composite materials of carbon in nickel oxide (C-NiO), carbon in zinc oxide (C-ZnO) and carbon in silicon dioxide C-SiO_2 using a simple sol-gel technique that suggest a potentially low cost production process for these highly efficient solar selective absorbers. Of these materials, C-NiO has been shown to have better functionality. Nickel oxide is used as a transparent binder (dielectric) whereas carbon is used as a light absorbing component (metal).

The objective of this study to take further the work done on the carbon embedded in nickel oxide matrix by doing a detailed systematic study of the sol-gel fabrication process and optimisation of optical properties.

1.6 Thesis outline

This dissertation is outlined as follows: chapter 1 gives an introduction of the theoretical background of a solar absorber that is relevant to this work. The background to the fabrication process i.e. sol-gel is presented in chapter 2. The fabrication processes and a brief description of each of the experimental techniques used are given in chapter 3 while chapter 4 deals with the results and discussion. Finally, the dissertation is concluded with the summary of the main results and the salient deductions made from them as well as suggestions for future work.

References

[1.1] G.W. Crabtree and N.S. Lewis, *Sol. Energy. Con., Physics today* **60** (2007) 37.

[1.2] NASA. maps.grida.no/library/files/storage/0203_nrsolar_205.pdf. Accessed 17-02-2012.

[1.3] C.G. Granqvist, *J. Appl. Phys. A* **52** (1991) 83.

[1.4] C.G. Granqvist and V. Wittwer, *J. Sol. Energy Mat. & Solar Cells* **54** (1998) 39.

[1.5] H.A. Ossenbrink, *The Future for Renewable Energy II,* edited by EUREC Agency, *James and James (Scientific publishers) Ltd., London UK* (2002) ISBN 1 90291631X.

[1.6] Z. Yin, *J. Sol. Energy Mat. & Solar Cells*, **86** (2005) 427.

[1.7] J.A. Duffie and W.A. Beckman, *Solar Engineering of Thermal Processes. John Wiley & Sons, Inc., New York*, (1991). ISBN: 0-471-51056-4.

[1.8] J. Gordon, *Solar Energy: The state of the art. James and James (Scientific publishers) Ltd., London UK*, (2001). ISBN: 1902916239.

[1.9] M. Lundt, *DPhil Thesis, Uppsala University* (2009).

[1.10] M. Nejati, *DPhil Thesis, Saarland University* (2009).

[1.11] F.K. Richtmyer and E. H. Kennard, *Introduction to Modern Physics IV, McGraw-Hill, New York*, (1947).

[1.12] R.M. Tennent, *Science Data Book, Longman House, Oliver and Boyd, United Kingdom* (1993) ISBN: 0050024876.

[1.13] T. Tesfamichael, *DPhil Thesis, Uppsala University* (2000).

[1.14] ISO report no. **ISO 9845-1** (1992).

[1.15] Y. Mastai, S. Polarz, and M. Antonietti, *Adv. Funct. Mater.* **3** (2002) 197.

[1.16] G.A. Nikklasson and C.G. Granqvist, *J. Matt. Sci.* **18** (1983) 3475.

[1.17] C.E. Kennedy, N.R.E. L., Task No. CP02.2000, NREL/TP-520 (2002).

[1.18] G.A. Niklasson and C.G. Granqvist, *Material Science for Solar Energy Conversion Systems* edited by C.G. Granqvist, *Renewable Energy Series, Pergamon Press, Oxford* (1991). ISBN: 0080409377.

[1.19] B.O. Seraphin, *Thin Solid Films* **57** (1979) 293.

[1.20] G. Pellegrini, *J. Sol. Energy Materials* **3** (1980) 391.

[1.21] E. Randrich, D.D. Allred, *Thin Solid Films* **83** (1981) 393.

[1.22] O.P. Agnihotri, and B.K. Gupta, *Solar Selective Surfaces. John Wiley & Sons, New York* (1981). ISBN: 0471060356.

[1.23] D. Chen, Y. Yan, E. Westenberg, D. Niebauer, N. Sakatani and S.R. Chaudhuri, *J. Sol-Gel Sci.Tech.* **19** (2000) 77.

[1.24] B.O. Seraphin, *Thin Solid Films* **39** (1976) 87.

[1.25] J.W. Twidell and A.D. Weir, *Renewable energy resources, The University Press, Cambridge, London* (1986).

[1.26] F. Simonis, M. van der Leij, and C.J. Hoogendoorn, *J. Sol. Energy Mater.* **1 (**1979) 221.

[1.27] B.O. Seraphin and A. B. Meinel, *Optical Properties of Solids: New Developments*, edited by B.O. Seraphin *North Holland Publ. Co., Amesterdam* (1976). ISBN: 0444110054.

[1.28] J.J. Cuomo, J.F. Ziegler, and J.M. Woodale, *Appl. Phys. Lett.* **26** (1975) 557.

[1.29] G. D. Pettit, J.J. Cuomo and T. H. DiStefano and J.M. Woodall, *IBM J. Res. Dev.* **22** (1978) 372.

[1.30] D.P. Grimmer, K.C. Herr and W.J. McCreary, *J. Vac. Sci. Tech*. **15** (1978) 59.

[1.31] G.L. Harding and M.R. Lake, *J. Solar Energy Mater*. **5** (1981) 445.

[1.32] G.A. Niklasson and H.G. Craighead, *J. Appl. Phys.* **54** (1983) 5488.

[1.33] P. Konttinena, P.D. Lunda, R.J. Kilpib, *J. Sol. Energy Mat. & Solar Cells* **79** (2003) 273.

[1.34] R.A. Buhrman and H.G. Craighead, *Composite Film Selective- Absorbers, in Solar Materials Science*, edited by L.E. Murr, *Academic Press, New York*, (1980). ISBN: 0125111606.

[1.35] G.A. Niklasson and C.G. Granqvist, *Selectively Solar-Absorbing Surface Coatings: Optical Properties and Degradation, in Materials Science for Solar Energy Conversion Systems,* edited by C.G. Granqvist, *Pergamon Press, New York*, (1991). ISBN: 0080409377.

[1.36] E. Wäckelgård, G.A. Niklasson and C.G. Granqvist, *Selectively Solar- Absorbing Coatings, Solar Energy: The state of the art. James and James (Scientific publishers) Ltd., London UK*, (2001). ISBN 1902916239.

[1.37] H.G. Graighead, R. Bartynski, R.A. Buhrman, L. Wojcik, and A.J. Sievers, *J. Solar Energy Mater.* **1** (1979) 105.

[1.38] C. Sella, A. Kaba, S. Berthier and J. Lafait, *J. Solar Energy Mater*. **16** (1987) 143.

[1.39] G.A. Niklasson and C.G. Granqvist, *J. Appl. Phys.* **55** (1984) 3382.

[1.40] T.K. Vien, C. Sella, J. Lafait and S. Berthier, *Thin Solid Films* **126** (1985) 17.

[1.41] G.L. Harding, Z. Yin, S. Craig and S.P. Chow, *J. Solar Energy Mater.* **10** (1984) 187.

[1.42] Z. Yin and G.L. Harding, *Thin Solid Films* **120** (1984) 81.

[1.43] V. Teixeira, E. Sousa, M.F. Costa, C. Nunes, L. Rosa, M.J. Carvalho, M. Collares-Pereira, E. Roman, and J. Gago , *Thin Solid Films* **392** (2001) 320.

[1.44] J.C. Fan and S.A. Spura, *Appl. Phys. Lett.* **30** (1977) 511.

[1.45] W. Graf, F. Brucker, M. Köhl, T. Tröscher, V. Wittwer and L. Herlitze, *J. Non-Crystalline Solids*, **218** (1997) 380.

[1.46] M. Okuyama, K. Furusawa and Y. Hamakawa, *J. Solar Energy* **22** (1979) 479.

[1.47] H. G. Craighead and R. A. Buhrman, *Appl. Phys. Lett.* **31** (1977) 423.

[1.48] T. Bostrom, E. Wackelgard and G. Westin, *J. Solar Energy* **74** (2003) 497.

[1.49] T. Bostrom, *DPhil Uppsala University* (2006).

[1.50] G. Katumba, J. Lu, L. Olumekor, G. Westin and E. Wäckelgård, *J. of Sol-Gel Sci. & Tech.* **36** (2005) 33.

[1.51] G. Katumba. *DPhil. University of Zimbabwe* (2006).

[1.52] G. Katumba L. Olumekor, A. Forbes, G. Makiwa, B. Mwakikunga, J. Lu and E. Wäckelgård, *J. Sol. Energy Mat. & Solar Cells* **92** (2008) 1285-1292.

[1.53] G. Katumba, G. Makiwa, T.R. Baisitse, L. Olumekor, A. Forbes, and E. Wäckelgård, *Phys. Stat. Sol (c)* **2** (2008) 549.

[1.54] Z.C. Orel, *J. Solar Energy Mater. & Solar Cells.* **57** (1999) 291.

[1.55] Solec Solar Energy Corporation. www.solec.org/solkotehome.htm. Accessed 17-02-2012.

[1.56] L. Holland, *Vacuum deposition of thin films VI, Chapman and Hall Ltd, London* (1970). ISBN: 0412053802.

[1.57] B.A Joyce, *The chemical vapour deposition of single crystal films. The use of thin films in physical investigation, London: Academic Press*. (1966).

[1.58] K.L. Chopra, D.K. Pandya and L.K. Malhotra, *Solar selective coatings. Review of renewable energy resources II. Wiley Eastern, New Delhi* (1986). ISBN: 0470275324.

[1.59] E. Wäckelgård, *J. Phys.: Condens. Matter.* **8** (1996) 5125.

[1.60] http://en.wikipedia.org/wiki/Spray_painting. Accessed 2012-02-17.

[1.61] Z.C. Orel and M.K. Gunde, *Sol. Energy Materials & Solar Cells* **61** (2000) 445

[1.62] Z.C. Orel M.K. Gunde A. Lencek and N. Benz, *Solar energy* **69** (2000) 131.

[1.63] J.C. Fan, *Thin Solid Films* **80** (1981) 125.

[1.64] O.T. Inal and A. Sherer, *J. Mater. Sci.* **21** (1986) 729.

[1.65] K. Gelin, *DPhil, Uppsala University* (2004).

[1.66] M. Lanxner and Z. Elgat, *SPIE* **1272** (1990) 240.

[1.67] R.R. McKeczie, *Appl. Phys. Lett*. **34** (1974) 25.

[1.68] C.M. Lampert, *SPIE* **3138** (1997) 134.

[1.69] J. Salmi, J.P. Bonino and R.S. Bes, *J. Mater. Sci*. **35** (2000) 1347.

[1.70] E. Wäckelgård and G. Hultmark, *Sol. Energy mat. Sol. Cells* **54** (1998) 165.

[1.71] A. Anderson, O. Hunderi and C.G. Granqvist, *J Appl. Phy*. **51** (1980) 754.

[1.72] C.G. Granqvist, *Material Science for Solar energy Conversion Systems, Pergamon* (1991). ISBN 080409377.

[1.73] A.G. Vila, E.C Barrera, L.A. Huerta and S. Muhl, *Energy Mat. Sol. Cells* **82** (2004) 269.

CHAPTER 2 : SOL-GEL PROCESS

The sol-gel technique was used for the fabrication of the samples in this study. The sol-gel process involves dissolving a molecular precursor in a liquid solvent forming solid in liquid dispersion (sol) which is followed by formation of solid network filled with the liquid (gel). It is generally used for fabrication of various glassy materials, structures as well as thin films [2.1]. This chapter presents a review of the process chemistry, coating processes and application of the so-gel technique to the C-NiO fabrication process.

2.1 Sol-gel process chemistry

The sol-gel process is a wet chemical technique which occurs in liquid solutions of organometallic and salt precursors. Sol-gel can be broadly described as the preparation of ceramic materials by preparation of sol, gelation of sol and removal of solvent. Steps followed in the sol-gel process are shown in figure 2.1 [2.1]. The core steps include preparation of precursor solutions (sols), deposition of the sols onto substrates and drying. Preparation of sols involves hydrolysis and polymerisation of precursors. The drying process usually involves a heat treatment of the gel in various mediums.

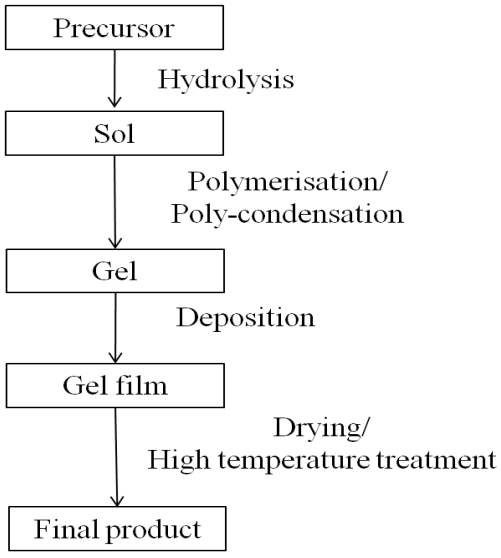

Figure 2.1: Sequence of basic steps in the sol-gel procedure [2.1].

The details of various chemistry processes involved in sol-gel have been reviewed by Brinker and Scherer [2.2]. In the sol-gel process, the precursors for preparation of a colloid (sol) consist of a metal or metalloid element surrounded by various ligands (appendages not including another metal or metalloid atom). A sol differs from a solution in that a solution is a single-phase system, while a sol is a suspension of small particles of one phase in another major (usually liquid) phase. The most popular precursors are metal alkoxides, because they react readily with water. Other precursors may be organic salts which can be dissolved in alcohols etc. This type of reaction is called hydrolysis. In hydrolysis a hydroxyl ion becomes attached to the metal atom, as in the following reaction:

$$M(OR)_n + H_2O \rightarrow M(OR)_{n-1}HO + ROH \quad (2.1)$$

M represents a metal, *n* is an integer number *R* represents a proton or other ligand (if *R* is an alkyl, then *OH* is an alkoxy group), and *ROH* is an alcohol.
Depending on the amount of water and catalyst present, hydrolysis may go to completion (so that all of the *OR* groups are replaced by *OH*):

$$M(OR)_n + nH_2O \rightarrow M(OH)_n + nROH \quad (2.2)$$

or stop while the metal is only partially hydrolysed to give $M(OR)_{n-x}(OH)_x$. Inorganic precursors can also be hydrolysed. The formation of a metal oxide involves connecting the metal centres with oxo (*M*-O-*M*) or hydroxo (*M*-OH-*M*) bridges, therefore generating a metal-oxo or metal-hydroxo polymers in the solution. Two partially hydrolysed molecules can link together in a condensation reaction, such as:

$$(OR)_3M\text{-}OH + HO\text{-}M(OR)_3 \rightarrow (OR)_3M\text{-}O\text{-}M(OR)_3 + H_2O \quad (2.3)$$

or

$$(OR)_3M\text{-}OR + HO\text{-}M(OR)_3 \rightarrow (OR)_3M\text{-}O\text{-}M(OR)_3 + ROH. \quad (2.4)$$

Condensation liberates a small molecule, such as water (equation 2.3) or alcohol (equation 2.4). This type of reaction can continue to build larger and larger molecules containing the metal by the process of polymerisation.

A polymer is a huge molecule (also called a macromolecule) formed from hundreds of thousands of units called monomers that are capable of forming at least two bonds. If a monomer can make more than two bonds, then there is no limit on the size of the molecule that can form. If one molecule reaches macroscopic dimensions so that it extends throughout the solution, the substance is called a gel. A gel may not differ from the parent sol in its composition and solid/liquid ratio or it may expulse part of the liquid and appear to be immersed in this liquid. The gel point is the time at which the last bond is formed that completes this giant molecule. Thus a gel is a substance that contains a continuous solid skeleton enclosing a continuous liquid phase. The continuity of the solid structure gives elasticity to the gel. If a sol does not gel, it usually is as stable as a solution. A sol may not gel because of the small size of the dispersed phase, which results in negligible gravitational forces.

Bond formation continues at the gel point. Segments of the gel network continue to move close enough together to allow further condensation and other bond forming processes. The smaller polymers or particles continue to attach themselves to the network. The term aging is applied to the process of change in structure and properties after gelation.

The removal of the remaining liquid requires a drying process which is accompanied by shrinkage and densification. A thermal treatment or firing is often necessary in order to favour future poly-condensation and enhance mechanical properties and structural stability via final sintering, densification and grain growth. The reactions in the sol-gel process depend on such parameters as the composition and concentrations of precursors and solvents used, type and concentration of catalyst used, additives, sequence in which component are added, time and type of mixing and temperature. The ultimate microstructure and properties of final component is influenced by changes imposed upon the structural template during the removal of the solvent. The properties can also be modified by various additives in the sol-gel phase [2.1-2.6]. For example structure directing templates can be added [2.5]; sugars have been used to change the density of the final films [2.6].

Various types of gels and films can be obtained from various sols for different applications. Figure 2.2 shows an illustration of various pathways and products in sol-gel technology. More details of the processes can be found in ref [2.2].

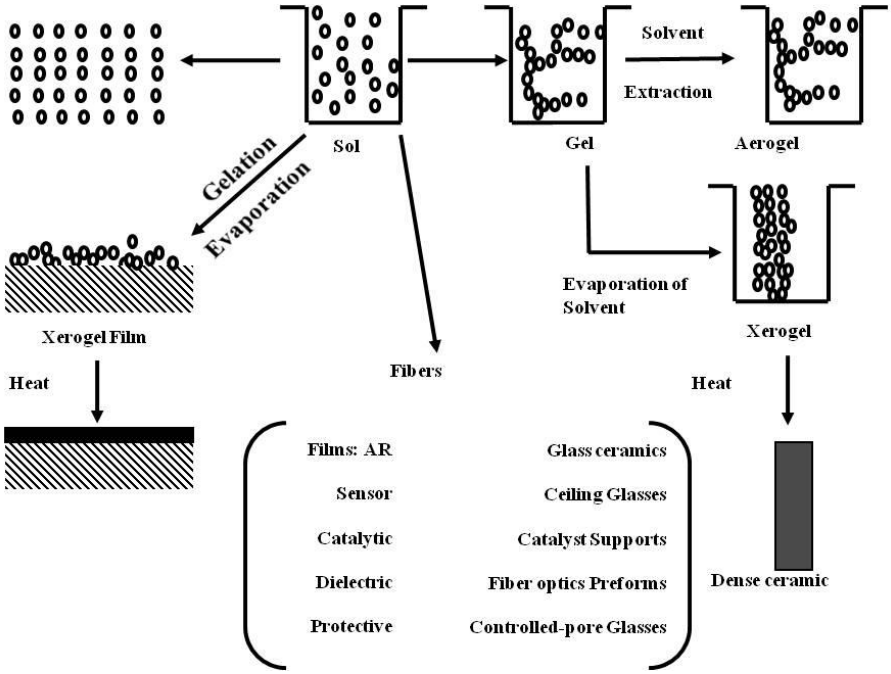

Figure 2.2: illustration of various pathways in so-gel technology showing fundamental principles of sol-gel processing and products.

2.2 Advantages of the sol-gel technique

The sol-gel technique has some advantages over a number of other fabrication techniques because of the following reasons:

- the ability to control the microstructure of the deposited film,
- formation products of high purity and homogeneity,
- opens a possibility of incorporating particles in a matrix,
- requires considerably less equipment,
- structures of different shapes can be fabricated using sol-gel procedure,
- can be adapted to other techniques such as spray coating, roll coating,
- and many more.

2.3 Sol-gel coating processes

In order to form films via the sol-gel process the prepared sols need to be coated on a suitable substrate. Common deposition processes are dip coating, spin coating or spraying. Various other coating processes can also be used. This work makes use of the spin coating process because it gives lab scale coatings of uniform thickness that are also easy to characterise.

2.3.1 Dip coating

This is the most commonly used deposition process because it is the easiest. It involves simply dipping a substrate into a sol then dragging it out covered by sol. Substrates of various shapes and sizes can easily be coated using this process. This coating process can be divided into five stages [2.7]: immersion, start up, deposition, drainage and evaporation. The thickness of the coating film produced with this process is determined by a complex competition between the following forces during the deposition stage: viscous drag upward on the liquid by the moving substrate, force of gravity, resultant force of surface tension in the concavely curved meniscus, inertial force of the boundary liquid layer arriving at the deposition region, surface tension gradient, and the disjoining or conjoining pressure.

2.3.2 Spin coating

The spin coating process involves ejecting a sol on a flat rigid substrate then spinning the substrate at high speed. The substrates used for this process are limited to a size that can be held down steadily for spinning at very high rotational speeds. The rotational speed varies between 1000 and 8000 revolutions per minute (rpm). The process is divided into four stages [2.8]: deposition, spin-up, spin-off, and evaporation. The first three stages are sequential, while the fourth normally proceeds throughout the coating process. In the deposition stage an excess amount of liquid is delivered to the substrate, which is at rest or spinning slowly. In the spin-up stage the liquid flows outward, driven by the centrifugal force generated by the rotating substrate. This stage generally occupies the time it takes the substrate being spun to reach a maximum speed. In the spin-off stage, excess fluid in the liquid film covering the substrate flows radially to the perimeter, accumulating there temporarily in unwanted swelling from which droplets form and fly off. As film becomes thin the remaining liquid slows. The evaporation stage generally continues after spin-off has stopped by solidification caused by the concentration of non-volatile solutes and particulates. Final film thickness is minimally affected by deposition and spin-up. The important stage of spin coating process is the spin off stage. Apart from the edge effect a film of liquid tends to become uniform in thickness as it thins by spin-off and remain so as it thins further, provided its viscosity is insensitive to shear and does not vary over the substrate. Film uniformity is the result of two counteracting forces: the rotation-induced centrifugal force, which drives radially outward flow, and the resisting viscous force, which acts radially inward.

The thickness of a spin coating is the result of the delicate transition by which evaporation takes over from spin-off. Non-volatile constituents can leave the substrate solely by flow. The final coating is made up of non-volatile constituents left when the film becomes thin and viscous enough that there is no further flow.

2.3.3 Spray coating

In spray coating a device sprays a coating through the air onto a surface using a combination of compressed air and a coating to atomise and direct coating particles [2.9]. The sol-gel technique can be adapted to spray coating process in order to scale up the fabrication of thin film coatings. Advantages of spray coating are that it can be applied at a rapid rate and gives good finish quality. The disadvantage of spray coating is that some coating particles bounce back as they reach the surface of the substrate which lowers transfer efficiency.

2.4 C-NiO fabrication process

Acetate sol-gel is used for the fabrication of the nickel oxide matrix. In acetate sol-gel a compound that comprises of acetate ligands attached to a metal centre is used as a precursor for the formation of the oxide of that metal. In this work nickel acetate is used as a precursor compound for the formation of the nickel oxide.

Metal salts are more suitable for large scale applications because of low cost, ease of use, and availability. Acetates in particular are more preferable salts because the acetate groups are decomposable during annealing, forming combustion volatile by-products [2.10]. Acetate sol-gel has been used before for the fabrication of metal oxide coatings, most popularly ZnO [2.11].

The idea of possibly incorporating carbon in a nickel oxide host matrix by mixing an oxide precursor sol with a carbon precursor sol is explored in this study. A template of poly ethylene glycol is used to direct the structure of the host matrix to form pores where the carbon would find a place to sit. A solution of sugar dissolved in water was used as a carbon precursor sol. Sugars are preferred precursors for elemental carbon [2.12]. Thermal combustion of sugar leads to the formation of carbon and water (see equation 2.5). It is possible to harness carbon if the thermal treatment is done in an oxygen free environment. In this study the thermal treatment was done in an inert (nitrogen) environment. The sol-gel technique for the preparation of NiO samples is related to the method described by Liu *et al*. [2.11] and adapted by Katumba *et al* [1.13, 1.14]. The following chemical equation shows the chemistry of the formation of carbon:

$$C_{12}H_{22}O_{11}\ \textit{(heat)} \rightarrow 12C + 11H_2O. \qquad (2.5)$$

The details of the procedure followed in fabricating C-NiO coatings is described in the next chapter.

References

[2.1] S.M. Attia, J. Wang, G. Wu, J. Shen and J. Ma, *J. Mater. Sci. Technol.* **18** (2002) 211.

[2.2] C.J. Brinker and G.W. Scherer, *Sol-Gel Science: The Physics and Chemistry of Sol-Gel Processing*, *Academic Press*, *San Diego* (1990). ISBN 0121349705.

[2.3] R.B. Pettit and C.J. Brinker, *J. Sol. energy mater*. **14** (1986) 269.

[2.4] Z. Liu, Z. Jin, W. Li and J. Qui, *Mater. Lett.* **59** (2005) 3620.

[2.5] K. Kajihara and T. Yao, *J. of Sol-Gel Sci. and Tech.* **19** (2000) 219.

[2.6] Y. Zhang, H. Jia, P. Li, F. Yang, and Z. Zheng, *Optics Communications* **284** (2011) 236.

[2.7] L. E. Scriven, *Mater. Res. Soc. Symp*. **1221** (1988) 717.

[2.8] D.E. Bornside, C.W. Macosko and L.E. Scriven, *J. Imaging Tech.* **13** (1987) 122.

[2.9] http://en.wikipedia.org/wiki/Spray_painting. Accessed 2012-02-17.

[2.10] L. Armelao, M. Fabrzio, S. Gialanella and F. Zordan, *Thin Solid Films* **394** (2001) 90.

[2.11] Z. Liu, Z. Jin, W. Li, and J. Qui, *J. Mater. Lett.* **59** (2005) 3620.

[2.12] Y. Mastai, S. Polarz, and M. Antonietti, *Adv. Funct. Mater.* **3** (2002) 197.

[2.13] G. Katumba L. Olumekor, A. Forbes, G. Makiwa, B. Mwakikunga, J. Lu, and E. Wäckelgård, *Sol. Energy Mat. & Solar Cells* **92** (2008) 1285.

[2.14] G. Katumba G. Makiwa, T. R. Baisitse, L. Olumekor, A. Forbes, and E. Wäckelgård, *Phys. Stat. Sol (c),* **2** (2008) 549.

CHAPTER 3 : EXPERIMENTAL PROCEDURES AND TECHNIQUES

In this chapter, the experimental details of the fabrication of C-NiO composite coatings used in this study will be presented. The coatings were deposited by a sol-gel technique. In section 3.1 the procedure followed for sample preparation will be discussed. The procedure includes sol preparation, substrate preparation, spin coating and heat treatment in a furnace. In section 3.2 techniques for characterisation will also be presented. These include thermal characterisation of the precursor sols as well as material and optical characterisation of the fabricated coatings.

3.1 Sample preparation

3.1.1 Procedure

The sample preparation procedure was done in a normal wet chemistry laboratory and easy to use set up. Figure 3.1 gives a flow chart of the steps in the procedure for the preparation of the samples while figure 3.2 shows the set-up for the preparation of the final solution used in this study.

The precursor sol was prepared by mixing the NiO and carbon precursor sols. The nickel oxide sol was prepared as follows:

- 7.5 g nickel acetate tetra hydrate [$Ni(CH_3COO)_2.4H_2O$] was added to a 500 ml plastic bottle containing 50 ml ethanol [(EtOH), CH_3CH_2OH]
- the mix was stirred using a magnetic stirrer until all the nickel acetate was dissolved
- 6.3 g diethanol amine [(DEA), $NH(CH_2CH_2OH)_2$] was added to stabilise the above solution
- then, the solution was ready to be mixed with a carbon precursor sol

The carbon precursor sol was prepared as follows:

- Selati Golden brown sugar purchased from Makro South Africa was added to a 250 ml separate plastic bottle containing 8 ml deionised water
- the mixture was stirred with a magnetic stirrer until all the sugar was dissolved

The carbon precursor sol was added to the NiO precursor sol and stirred further for 5 minutes. A structure directing template Polyethylene Glycol [(PEG), $HO(CH_2CH_2O)_nH$] was added to this solution to make the final solution.

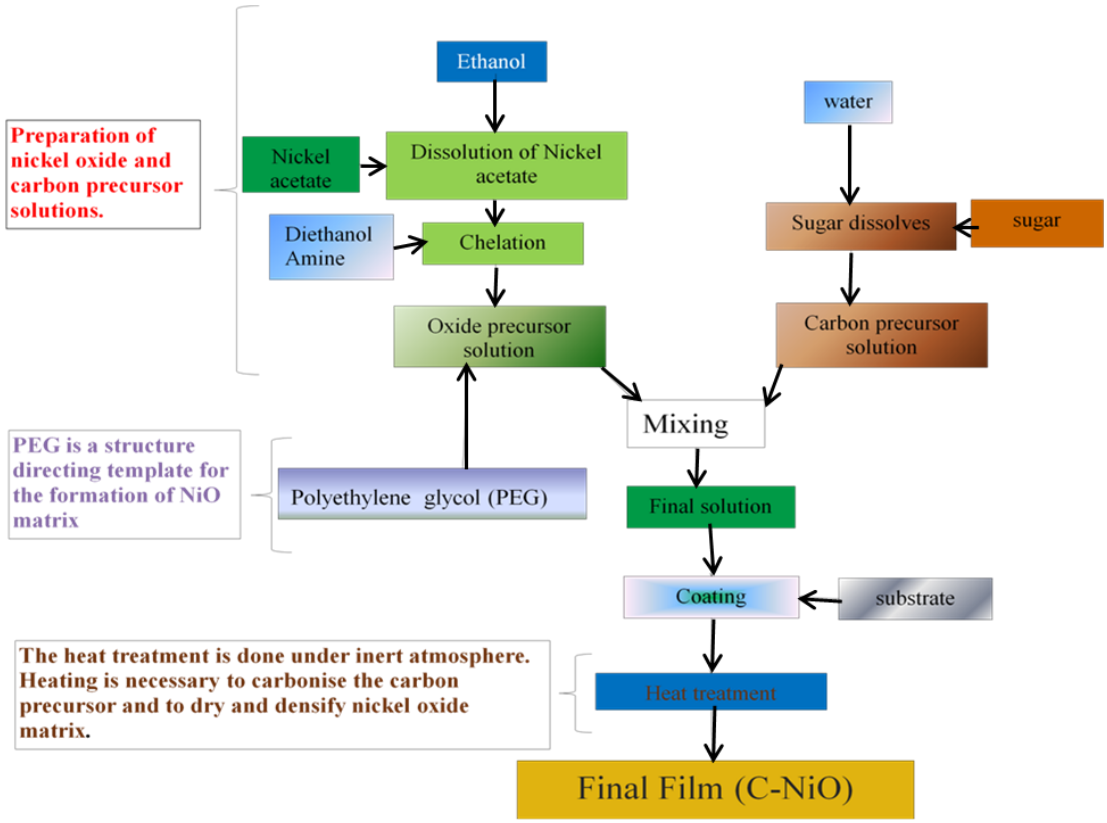

Figure 3.1: Flow chart of the steps in the procedure for the preparation of the samples.

Figure 3.2: Set-up for the preparation of the final solution. It is a normal wet chemistry lab and easy to use set-up.

The final solution was then spin coated on to pre-cleaned rough aluminium substrates. The spin-coated samples were heat treated in a tube furnace in flowing nitrogen gas for 1 h to carbonise the carbon precursor and also to dry and sinter the oxide matrix.

3.1.2 Substrate preparation

Rough aluminium substrates were used in the sample fabrication process. Aluminium was chosen because of its high optical reflectivity. Aluminium substrates used in this study which were 55×55 cm^2 were cut from a 2×1 m^2 aluminium sheet. In order to ensure that the sol adheres on the substrates, substrate pre-treatment was necessary. The substrates were thoroughly degreased by washing with liquid soap followed by rinsing in water. In order to remove the protective oxide (alumina) on the aluminium surface an etching solution made of 8:1 volume ratio of water and phosphoric acid was used. The substrates were etched for 20 minutes at 50 °C. Thereafter, the substrates were rinsed in deionised water and dried by blowing with nitrogen on the surface.

3.1.3 Spin coater

A spin coater was used for coating the substrates with a precursor sol. A detailed background on spin coating process is given in section 2.3.2. The spin coater used was model KW-4A manufactured by Chemat technology Inc. Figure 3.3 shows a picture of the spin coater used in this study. It has controls for coating (timer and speed dial) and drying (timer and speed dial) stages.

Figure 3.3: A photograph of Chemat spin coater (Model KW-4A) used in this study.

The rotation speed of this spin coater is displayed in revolutions per minute (RPM) units. The coating stage has low rotation speeds (between 0 and 500 RPM) while drying stage has a high rotation speeds (1000-8000 RPM). The sample is placed on the vacuum chuck and vacuum is applied in order to keep the sample stationary when the chuck is rotating. The coating solution is egested on to the rotating substrate during the coating stage. Then the spin coater moves to the drying (high rotation speed) stages to complete the process.

3.1.4 Furnace

A quartz tube furnace model GVC 12/1200 from Carbolite was used for heat treatment. The furnace used was used for heat treatment. Figure 3.4 shows the furnace the set up used in this study which consists of tube furnace, nitrogen bottle as well, furnace control and temperature monitoring unit. During the heating process, the furnace temperature is ramped at 5 °C/min to a desired temperature and then dwells at the desired temperature for an hour. Once the heat treatment was done, the samples were allowed to cool down naturally back to room temperature. The dwell temperature is what will be referred to as heat treatment temperature throughout this dissertation. During the heating process, nitrogen gas was flowing (flow rate 5 L min^{-1}) through the tube containing the samples to ensure they are heated in an inert atmosphere.

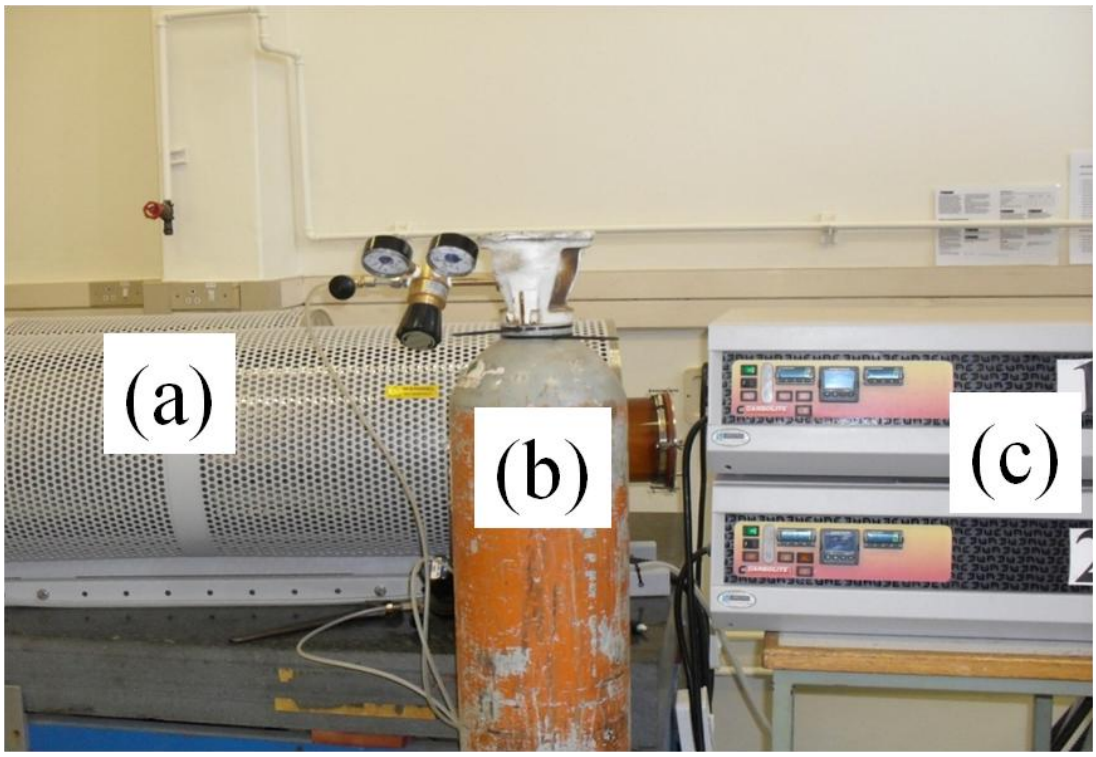

Figure 3.4: Furnace set up including (a) tube furnace, (b) nitrogen bottle as well as (c) furnace control and temperature monitoring unit.

3.2 Characterisation techniques

3.2.1 Thermal characterisation of the precursor sol

3.2.1.1 Thermo-gravimetric analysis (TGA)

Thermo gravimetric analysis was used to determine the final heat treatment temperature for coatings used in this study. TGA is a type of analysis performed to determine the change in weight of materials in relation to change in temperature or time in a controlled atmosphere. Measurements are used primarily to determine the composition of materials and to predict their thermal stability at temperatures up to 1000 °C. The technique can characterize materials that exhibit weight loss or gain due to chemical changes induced by changes in temperature. TGA analysis was performed by raising the temperature of the sample while measuring its weight change.

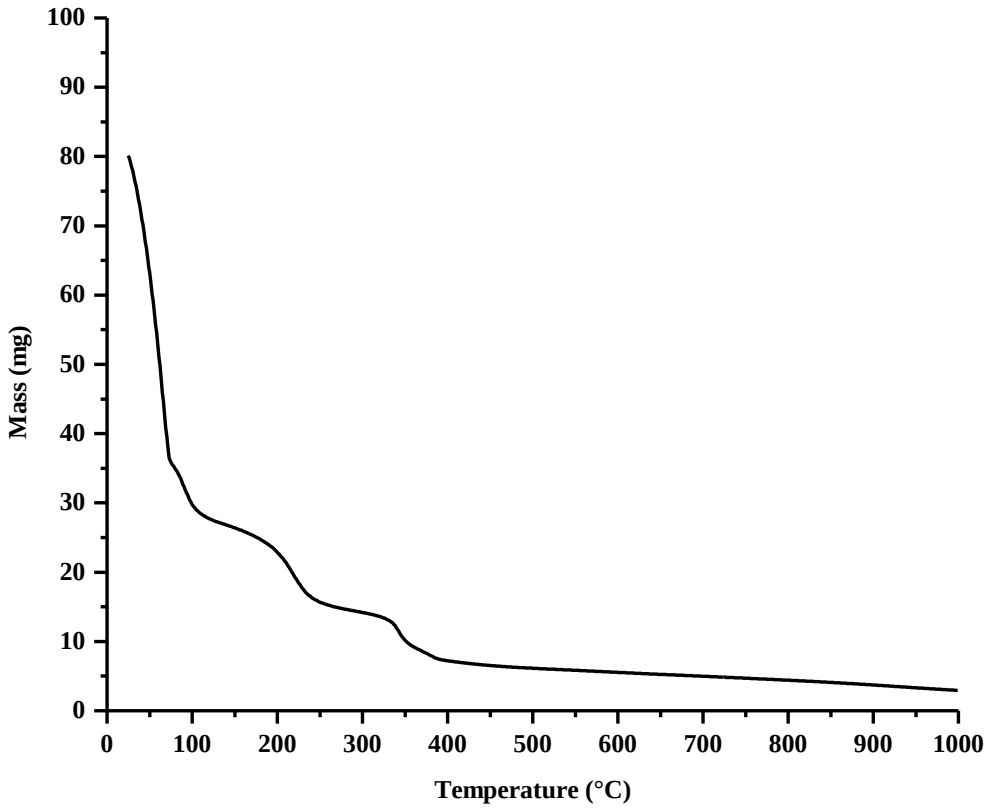

Figure 3.5: Typical TGA curve for a C-NiO precursor sol.

The thermo-gravimetric measurements (TGA) were done on Perkin-Elmer TGA 4000 thermo-gravimetric analyzer. Approximately 80 mg final mixture of C-NiO precursor solution was placed in open 190 μL alumina pan and heated from 25 °C to 980 °C at a heating rate of 5 °C min^{-1} in nitrogen atmosphere (flow rate 50 mL min^{-1}). A typical TGA curve of a final C-NiO mixture collected from 25 °C to 980 °C is shown in figure 3.5.

3.2.1.2 Differential scanning calorimetry (DSC)

Differential scanning calorimetry is a thermo-analytical technique in which the difference in the amount of heat required to increase the temperature of a sample and a reference is measured as a function of temperature. Both the sample and a reference are maintained at nearly the same temperature throughout the experiment. Generally, the temperature program for a DSC analysis is designed such that the sample holder temperature increases linearly as a function of time.

The basic principle underlying this technique is that when a thermal event occurs in the sample such as decomposition, melting, crystallisation etc more or less heat will need to flow to it than a reference to maintain both at the same temperature. Whether less or more heat must flow to the sample depends on whether the process is exothermic or endothermic. The data collected in the DSC will be a difference in heat flow between a reference and a sample over a chosen temperature range.

The DSC results were collected on Mettler Toledo DSC 1 instrument. Approximately 30 mg final mixture of C-NiO precursor solution was placed in an open pin-hole 40 μL aluminium pan; heated from 25 °C to 600 °C at a heating rate 5 °C min^{-1} in N_2 (flow rate 50 mL min^{-1}).

3.2.2 Material characterisation

3.2.2.1 Raman spectroscopy

Raman spectroscopy is a widely used technique for characterisation of carbonaceous and carbon containing nano-composite materials [3.1, 3.2]. This technique is based on an inelastic scattering experienced by light passing through a material, which involves absorption or emission of one or more phonons. The energy difference between the incident light and the emitted light is equal to the difference in vibrational and rotational energy levels of the molecule. Inelastic scattering must satisfy conservation of energy and momentum which is given by:

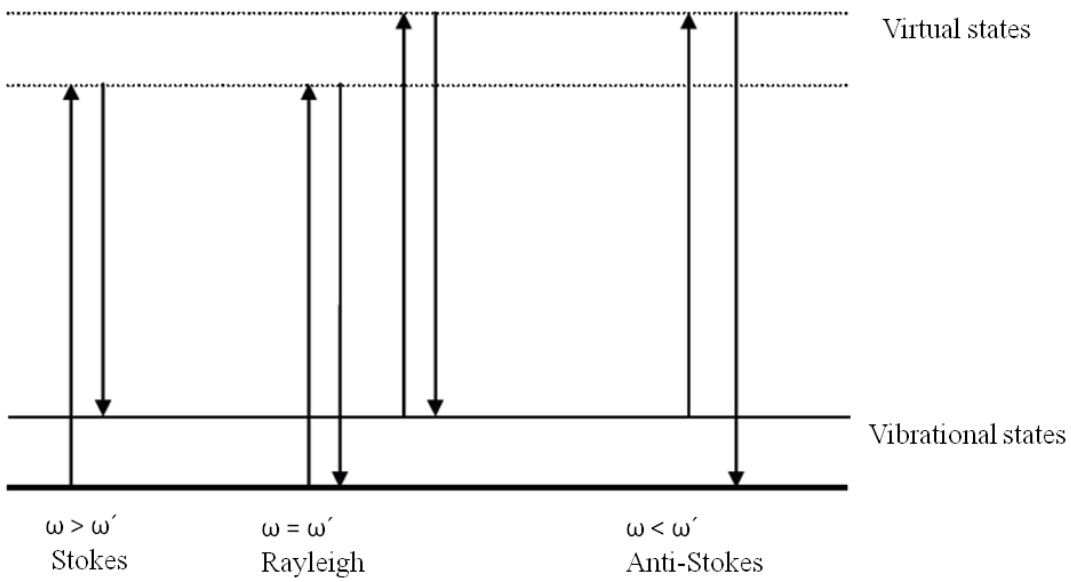

Figure 3.6: Energy level diagram showing the states involved in Raman signal. The Rayleigh signal is usually the most intense [3.4].

$$\omega_s = \omega - \omega', \tag{3.1}$$

$$k_s = k - k', \tag{3.2}$$

where ω, ω´ - frequencies of the incident light and scattered light

k, *k´* - wave vectors of incident light and scattered light

ω_s, k_s - scattering frequency and wave vector of the phonon involved.

Figure 3.6 is an energy level diagram showing the states involved in Raman signal. The line thickness is roughly proportional to the signal strength from the different transitions.
For ω > ω´ the process is called Stokes shift, which involves emission of phonons.
For ω < ω´ the process is called anti-Stokes shift which involves absorption of phonons.
For ω = ω´ the process is known as Rayleigh scattering.

The most intense scattering process is Rayleigh scattering process since most photons (one quantum of light energy) scatter in this manner. Usually Raman scattering is only recorded to give Stokes scattering, since this signal is much more intense than the anti-Stokes scattering signal because at room temperature not a lot of molecules are in the excited state.

In crystals only specific phonons are allowed by the periodic structure, so Raman scattering can only appear at certain frequencies showing sharp peaks on the Raman spectrum. For amorphous materials, more photons are allowed and thereby the discrete spectral lines

become broad. More details about the Raman technique can be found in reference [3.3], and further Raman description in relation to carbonaceous materials is given under discussion in section 4.2.2.

Raman spectra were collected using a Raman spectroscopy (Jobin-Yvon T64000 spectroscope), equipped with an Olympus BX-40 microscope attachment. An Ar+ laser (514.5 nm) with energy setting 1.2 mW from a Coherent Innova Model 308 was used as an excitation source. Figure 3.7 shows a typical Raman spectrum for the samples used in this study.

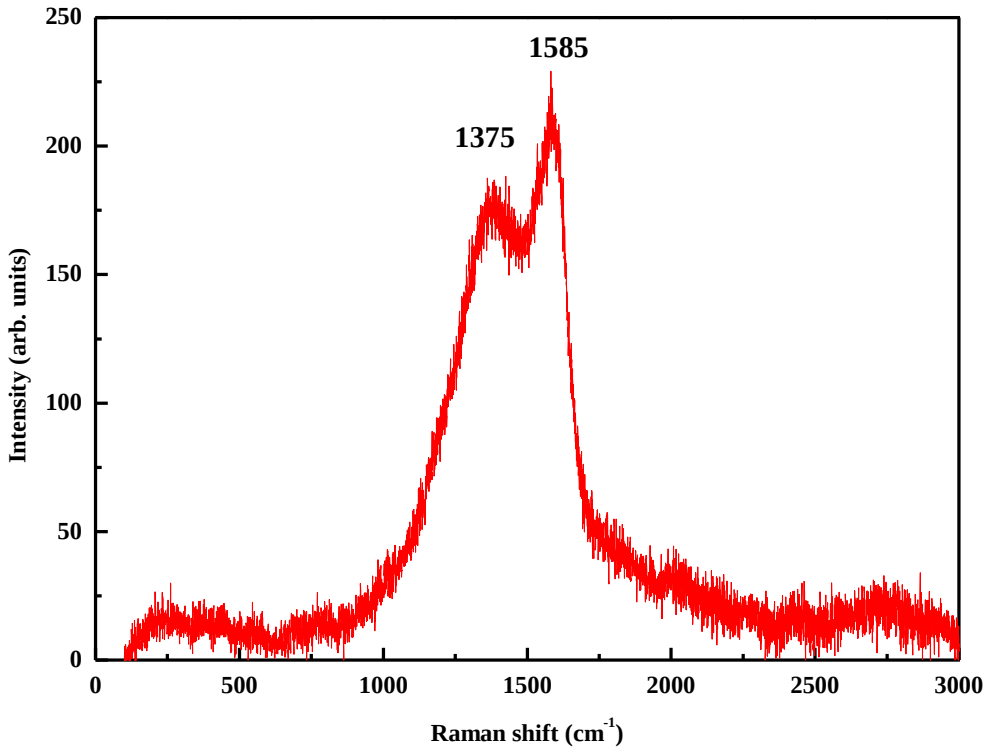

Figure 3.7: Raman spectrum of a sample prepared from a typical precursor sol and heat treated at 450 °C. The two peaks at 1375 cm^{-1} and 1585 cm^{-1} are D and G bands of carbon respectively (discussed in section 4.2.2).

3.2.2.2 Scanning X-ray photoelectron spectroscopy (SXPS)

Scanning X-ray photoelectron spectroscopy (SXPS) was used to perform quantitative analyses of carbon in this study. SXPS consists of irradiating a surface with X-rays in order to extract photo-electrons. Knowing the energy of the X-ray photons and measuring the kinetic

energy of the extracted electrons, one can determine the binding energy of the extracted electrons. This quantity is unique and can be used to identify the elements from which the electrons were extracted. The technique can detect all of the elements except hydrogen and helium, as well as compounds, because the binding energy of an element differs from compound to compound. It is primarily a surface technique, as the escape depth of the photoelectrons ranges from 2 to 5 nm. The detection limit of XPS is approximately 0.1 at %. Information from subsequent layers beneath the outer surface can be obtained by sputtering the surface with energetic argon ions, while monitoring the binding energy regions of specific elements.

The samples were analysed as prepared. X-ray photoelectron spectroscopy analysis was conducted by a Quantum 2000 spectrophotometer (Physica electronics) using a monochromatized Al Kα X-ray source (1486 eV photons). A typical XPS spectrum of C-NiO composite with 8 g SUC the precursor solution is displayed in figure 3.8.

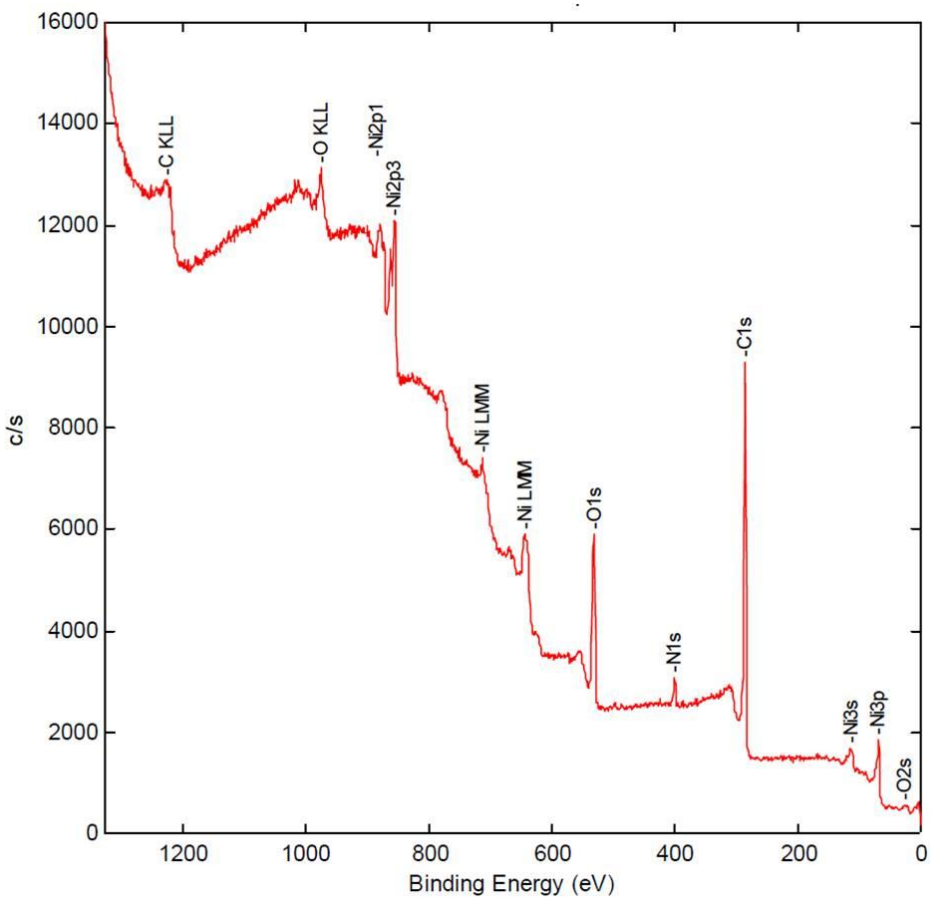

Figure 3.8: A Typical XPS spectrum of a C-NiO sample with 8 g SUC in the precursor solution.

3.2.2.3 Scanning Electron Microscope with Energy Dispersive Spectroscopy

The Scanning Electron Microscopy (SEM) is an analytical technique that uses scientific instruments with energetic electrons to examine materials at very fine scale, i.e. nanometer (nm) to micrometer (μm). The advantage of using the SEM includes higher magnification, larger depth of focus, greater resolution, and ease of sample observation. In an electron microscope, a stream of electrons is produced by an electron gun in vacuum, and then accelerated towards a specimen using a positive electrical potential. This stream of electrons is focused into thin, focused monochromatic beam by metal apertures and magnetic lenses. As this beam of electrons reaches the specimen, beam material interactions occur. During these interactions other electrons are ejected from the sample. These are either backscattered or secondary electrons. Detectors collect the secondary or backscattered electrons, and convert them to a signal that is sent to a monitor producing an image.

Other signals are possible during electron beam material interaction. These are summarised in figure 3.9 which shows a schematic illustration of the signals generated during the primary electron beam-specimen interaction. For this study the focus will be on characteristic X-rays

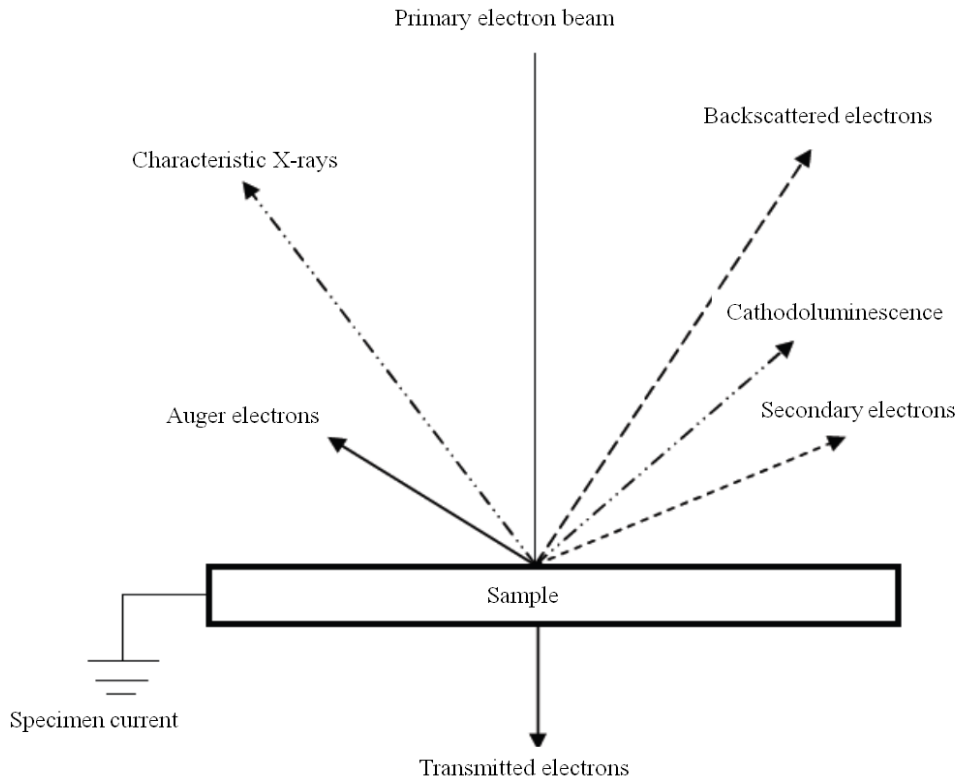

Figure 3.9: Schematic illustration of the signals generated during the primary electron beam – specimen interaction.

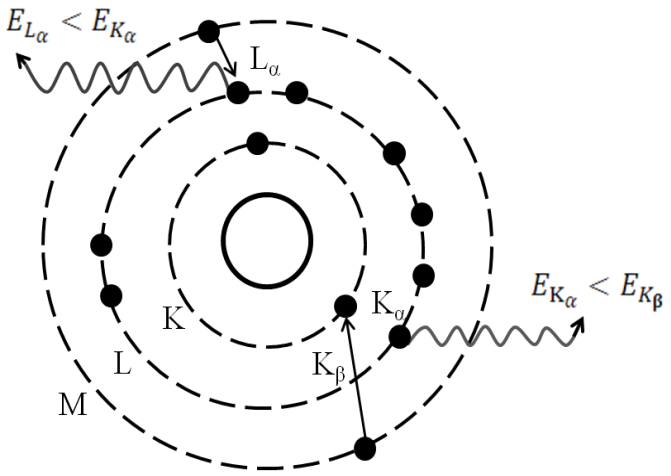

Figure 3.10: Characteristic X-ray emission by an atom [3.5].

which are useful for elemental characterisation of the samples studied. Figure 3.10 shows a schematic of characteristic X-ray emission of an atom.

The energy levels surrounding the nucleus of an atom are termed 'shells'. These shells are labelled K, L, M, … corresponding to the principle quantum number, n = 1, 2, 3. Upon interaction of the electron beam with this atom, it may dislodge one of the inner electrons, e.g. the atom in shell K. When this happens the atom is in an excited state. To return to its normal, ground state, an electron from one of the outer shells (e.g. L or M) needs to fill the vacancy left behind in the K shell. The difference in energy undertaken by the outer shell electron is a discrete amount, characteristic of the atom and is emitted as X-rays. When an electron from the L shell fills the K shell vacancy, the resulting X-ray is termed K_α, whereas when an M shell electron fills the vacancy K_β X-rays are emitted. The same nomenclature applies when an electron from an outer shell (e.g. L) is knocked out.

The phenomenon pictured in Figure 3.10 forms the basis for energy dispersive spectroscopy (EDS). The technique employs energy dispersion, which is the separation of X-rays according to their energy. This separation of energy is accomplished with the help of a semiconductor detector. When an X-ray strikes a semiconductor crystal, electrons in the crystal absorb a given amount of energy and are thus excited. The greater the X-ray energy, the greater the amount of electrons excited. The absorbed energy is then converted to an electronic signal, which is emitted and amplified. The strength of the current from the crystal is proportional to the X-ray energy. The amplified electrical pulses from the semiconductor are converted to

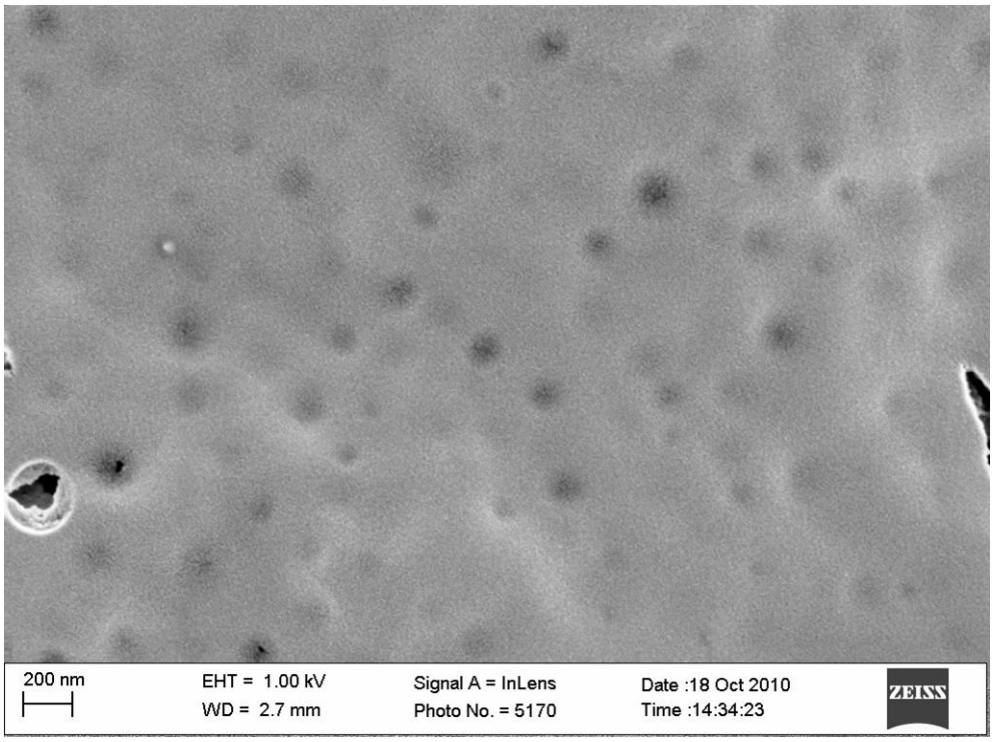

Figure 3.11: Scanning electron microscopy image of a typical sample used in this study showing surface morphology.

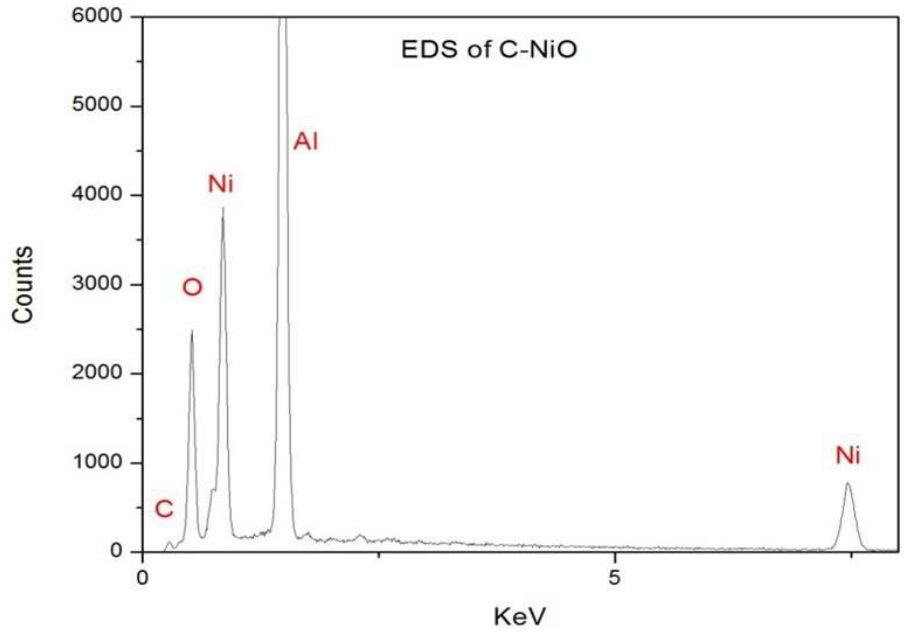

Figure 3.12: Energy dispersive spectroscopy spectrum of a typical sample used in this study showing elements found in the sample

digital form and fed into a multi-channel analyzer (MCA). The MCA sorts these signals and, in effect, counts the number of X-rays at each energy level that strikes the crystal. This information is then plotted as a spectrum.

The surface morphology of the thin films was investigated using a ZEISS ULTRA plus FEG-SEM scanning electron microscopy. Figure 3.11 is a scanning electron microscopy image of a C-NiO sample showing surface morphology. The Energy Dispersive Spectroscopy (EDS) analysis was done using a JEOL- JSM 7500F Scanning Electron Microscope. Figure 3.12 is a typical EDS spectrum for samples used in this study showing elements present in the sample.

3.2.3 Optical characterisation

For determining the optical performance of the spectrally selective solar absorber, the total reflectance was measured in the solar and infrared wavelength ranges between 0.3 and 20 µm. Figure 3.13 shows merged reflectance spectra for a typical sample used in this study. These

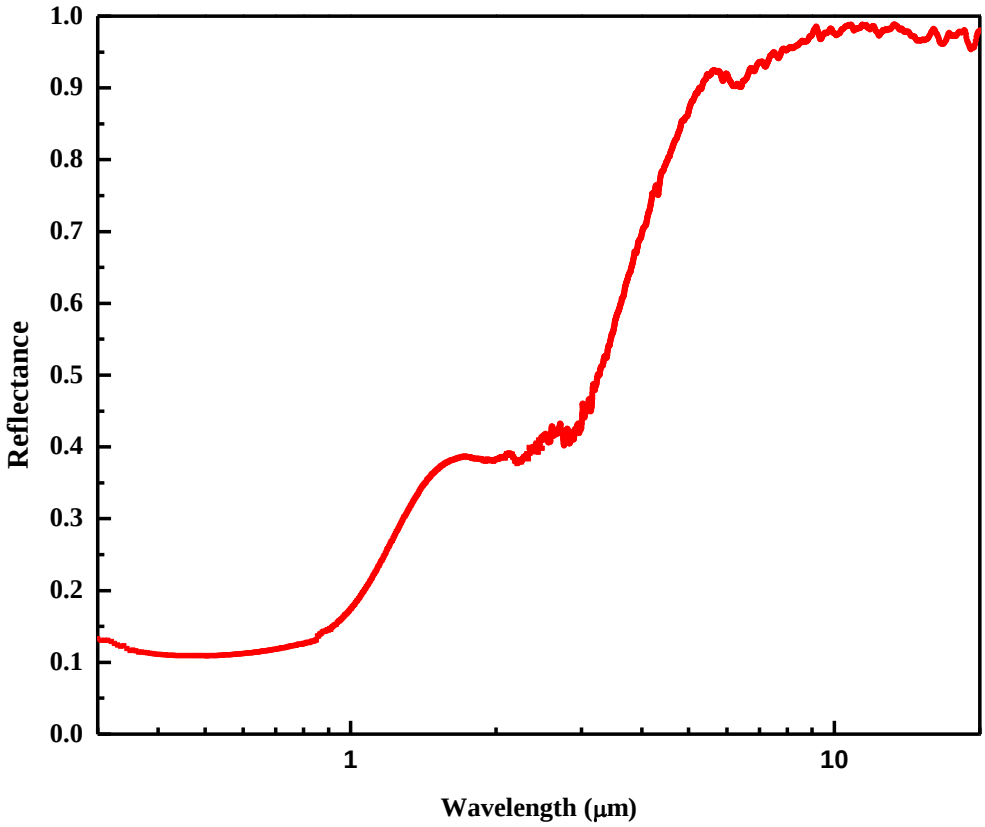

Figure 3.13: Typical reflectance spectrum in the UV to far infra-red range for a C-NiO coating on aluminium substrate.

data were used to calculate solar solar absorptance (α_{sol}) and thermal emittance (ε_{therm}) according to equation (1.13) and (1.14).

The instrument used for measurements in the solar spectral range was a Perkin-Elmer Lambda 900 UV/VIS/NIR double beam spectrophotometer. It is a dispersive type which uses a white light source and a few grating monochromators to create light with a specified wavelength. A detector collects the reflected or transmitted part of the light according to its setting and transfers it to the connected computer for further processing. The instrument is equipped with an integrating sphere to allow for measurements on the rough rolled aluminium sheets [3.6]. A Spectralon sample was used as the reference.

A type of Fourier Transform Infrared Reflectance (FTIR) spectrometer was used for measurements in the infrared range. FTIR spectrometry is essentially based on a Michelson interferometer, as shown in figure 3.14. The Michelson interferometer preserves the frequency and intensity information. It consists of a beam splitter, a fixed mirror and a moving mirror. The beam splitter takes the incoming infrared beam and splits it into two

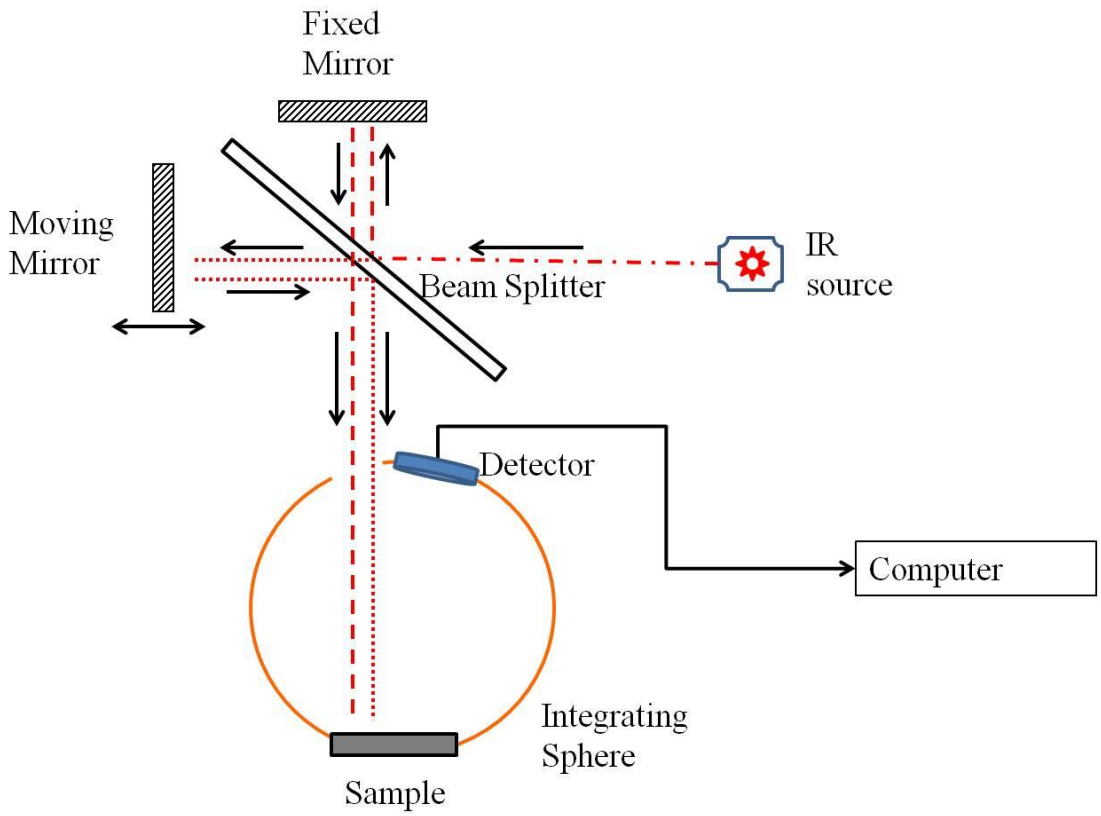

Figure 3.14: A schematic of an Infra-red data collection set-up showing a Michelson interferometer in a Fourier Transform Spectrometer. A gold coated integrating sphere attachment is for total reflectance measurements.

beams of nearly equal intensity. Half of the infrared beam is transmitted through the beam splitter and directed onto the fixed mirror. The other half reflects off the beam splitter and is directed onto the moving mirror. The beams reflect off the surfaces of the two mirrors and recombine at the beam splitter. Due to the changes in the relative position of the moving mirror to the fixed mirror, an interference pattern is generated. The resulting beam moves towards the sample absorption, reflection and transmission takes place. The light coming from the sample goes to the detector. The detected signal, called the interferogram as a function of the moving mirror is fed to a computer. Fourier Transformation converts the interferogram to the final infrared spectrum.

Infra-red data in reflection mode was collected with a TENSOR 27 from Bruker optic equipped with an integrating sphere coated with gold. The wavelength range was from 2.5 to 22 μm.

References

[3.1] A.C. Ferrai and J. Robertson, *Phys. Rev. B* **61** (2000) 1409.

[3.2] A. Jorio, M.A. Pimeta, A.G. S Filho, R.Saito, G. Dresselhaus and M.S. Dresselhauus, *New J. Phys.* **5** (2003) 139.

[3.3] E. Smith and G. Dent, *Modern Raman Spectroscopy: A practical approach', Wiley and Sons Ltd., Great Britain* (2005).ISBN: 0470011823

[3.4] C. Kittel, *Introduction to Solid State Physics VII, John Wiley and sons, New York* (1996). ISBN: 0471111813

[3.5] P. J. Goodhew and F. J. Humphreys, *Electron Microscopy and Analysis II, Taylor & Francis, London* (1988). ISBN: 0850664144

[3.6] A. Roos, *Sol. Energy Mat. & Solar Cells*, **30** (1993) 77.

CHAPTER 4 : RESULTS AND DISCUSSION

In this chapter experimental results are presented and discussed. These include thermal characterisation of precursor sol, elemental characterisation, and morphology of fabricated samples as well as optical properties at various process parameters. The chapter is concluded with comparison of different solar thermal coatings in terms of their thermal conversion efficiency and cost estimations.

4.1 Thermal characterisation of the precursor sol

The process used for fabrication in this study involves heat treatment of the C-NiO precursor sol in order to form the composite. Therefore, in order to determine a suitable temperature range for the heat treatment of the sols used in this study, thermo-gravimetric analysis was done. Figure 4.1 shows a typical TGA curve for C-NiO precursor sol consisting of a mixture of ethanol, nickel acetate, DEA, PEG, water and sugar. The differential of the TGA (DTGA) is also included. The DTGA curve shows a peak where there is a noticeable slope change on the TGA curve and indicates a weight change. The noticeable weight change stages in the DTGA curve are illustrated by dashed circles and numbered 1-5. All the weight changes in the curve are negative i.e. they are related to weight loss of the investigated sol. The stages are around temperatures: 31-57 °C, 75-144 °C, 144-295 °C, 295 -341 °C and 382 °C. The initial weight loss constituted 50 % and can be attributed to evaporation of the most volatile and abundant constituent of the sol, ethanol. Ethanol readily slowly vaporises at around a temperature of 35°C, strongly vaporises at 50 °C and boils at a temperature around 80 °C [4.1, 4.2]. The second and third weight loss constituted approximately 15 and 10 % and could be attributed to evaporation of water and degradation of some of the organic constituents such as PEG [4.3] and SUC [4.4]. Water boils at 100 °C and vaporises above that temperature. Previous study has shown that that SUC decomposition in a tin oxide-carbon composite fabrication took place between 225 °C and 502 °C [4.4]. A study of the thermal decomposition of PEG in nitrogen found that it decomposes between 200 °C and 389 °C [4.3]. The fourth weight loss constituted approximately 13 % of the total weight loss and is likely due to further degradation of remnant organic constituents such as PEG and SUC. From the fifth weight loss at 382 °C to higher temperatures the weight gradually decreases continuously. This indicates the degradation of a fairly thermally stable material which could be the formed C-NiO.

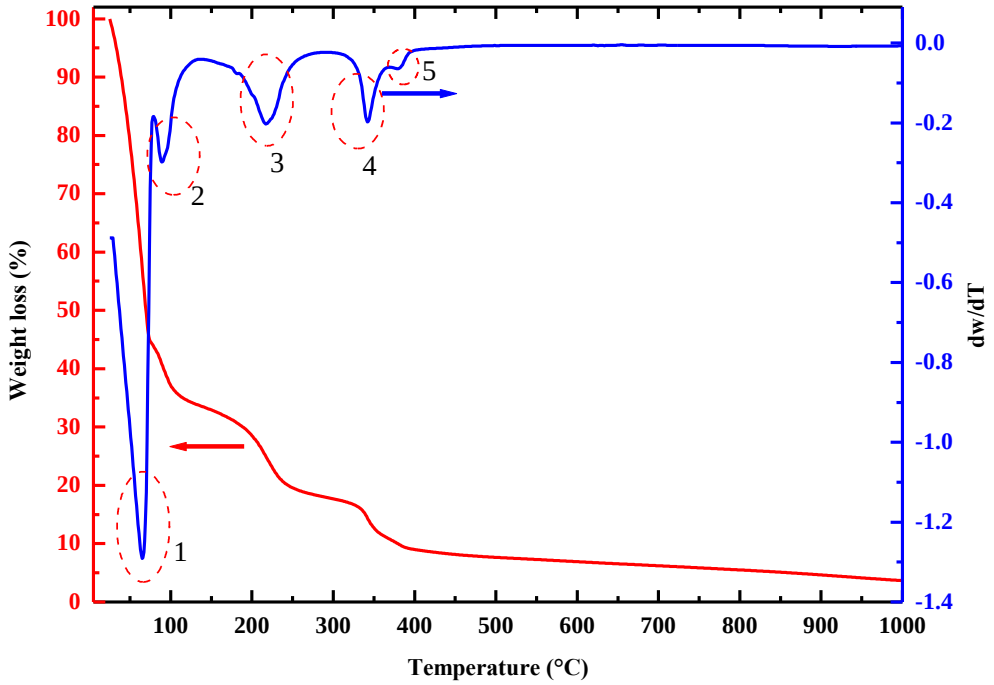

Figure 4.1: Typical TGA (red curve) and DTGA (blue curve) curve for a C-NiO precursor sol consisting of a mixture of ethanol, nickel acetate, DEA, PEG, water and brown sugar.

Figure 4.2 shows a DSC curve of a typical precursor sol consisting of a mixture of ethanol, nickel acetate, DEA, PEG, water and sugar. The heat flow at temperatures below 200 °C is generally less than 0 mW. There is a very broad endothermic peak numbered 1 from 0 °C to around 135°C. Within that peak is another sharp endothermic peak numbered 2 at 83 °C. Then there are 4 exothermic peaks numbered 4-6 at 210 °C, 262 °C, 342 °C and 436 °C. The positions of these peaks except for the last one correspond with weight loss positions observed in the DTGA curve (figure 4.1). The DSC peak at 436 °C does not correspond with any of the weight losses observed in the DTGA curve, but rather with the gradual weight loss above 382 °C which can be seen on the TGA curve of figure 4.1. Therefore the peak at 436 °C can be attributed to degradation of the remnants of SUC since it was shown to still decompose at such temperatures [4.4]. It must be noted that a DSC signal can show the energetic nature of thermal events that are not necessarily accompanied by huge weight loss events [4.5].

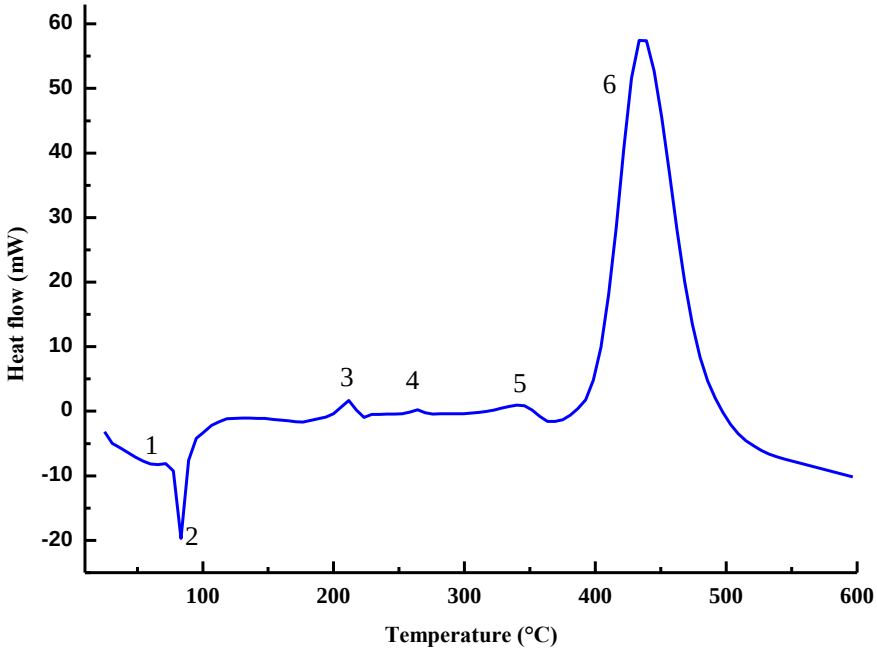

Figure 4.2: DSC curve of a typical C-NiO precursor sol.

From these thermal studies it was deduced that the final C-NiO material is formed at 436 °C. Therefore a temperature of 450 °C was chosen as a base heat treatment throughout this study.

4.2 Elemental characterisation

In order to determine the elemental composition of the fabricated material in this study, EDS analysis was conducted. Figure 4.3 shows an EDS spectrum of a sample fabricated from a sol prepared by mixing 50 ml ethanol, 7.5 g nickel acetate, 6.3 g DEA, 1 g PEG, 8 ml water and 8 g sugar and heat treated at 450 °C for 1 hour. Nickel, oxygen and carbon peaks are clearly visible and this indicates that C, and NiO are present in the sample. The Al peak is from the substrate used.

The signature of carbon present in the material was studied by Raman spectroscopy technique. Figure 4.4 depicts a typical Raman spectrum of the sample used for EDS. The spectrum shows two characteristic carbon peaks. The first peak at around 1585.58 cm^{-1} is the G-band which corresponds to planar vibrations of carbon atoms and is present in most

graphite-like materials [4.6]. Figure 4.5 shows a picture showing schematic atomic vibrations for G-band modes.

The second peak located at 1375.55 cm^{-1} is the D-band and is attributed to defects, curved graphite sheets and lattice distortions in the carbon structures [4.6]. It is evident that the intensity of the G-band is stronger than the D-band which suggests that there are fewer defects in the carbon present in the sample, therefore it is predominantly graphitic.

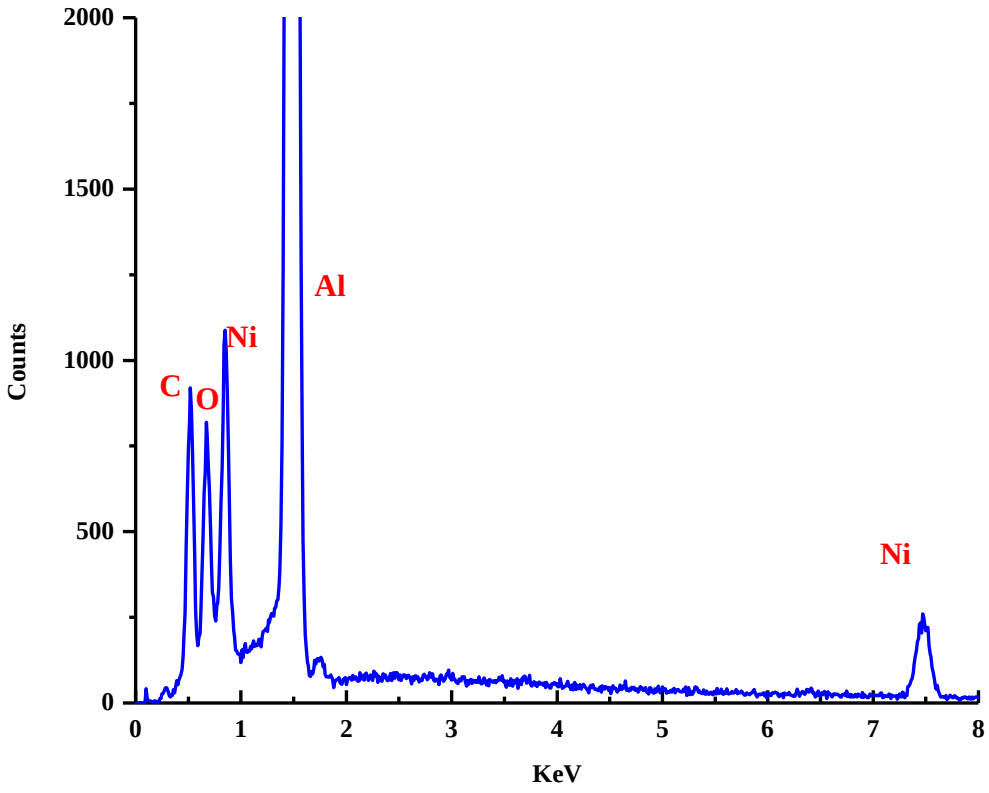

Figure 4.3: EDS of a C-NiO heat treated at 450 °C showing peaks for carbon, nickel, oxygen and aluminium.

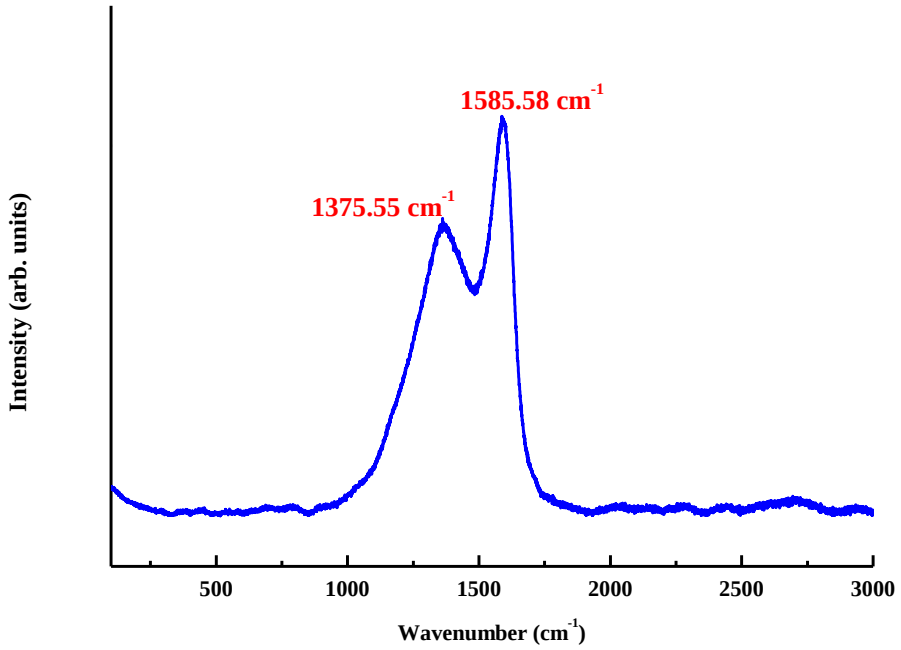

Figure 4.4: Raman spectrum of a sample prepared from a typical precursor sol and heat treated at 450 °C. The two peaks at 1375.55 cm^{-1} and 1585.58 cm^{-1} are D and G bands of carbon respectively.

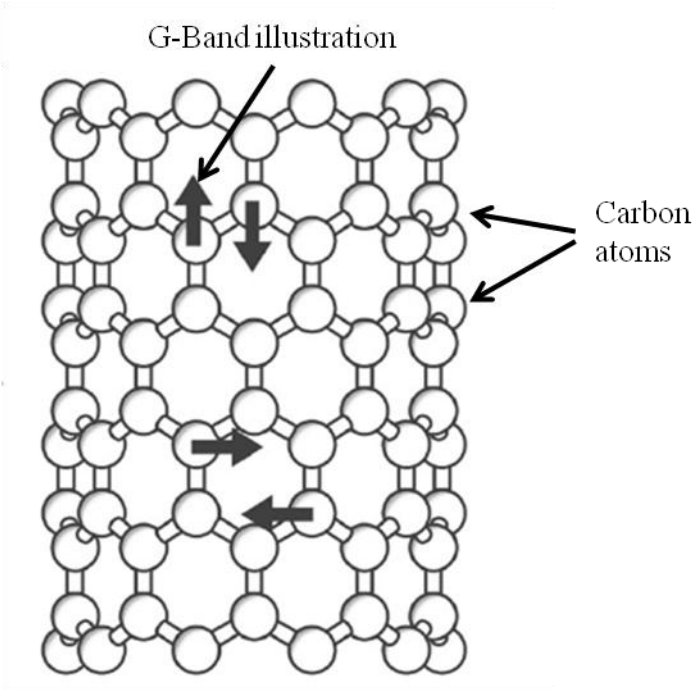

Figure 4.5: Schematic structure of G-band taken from [4.4].

4.3 Morphology of C-NiO

The morphology of the films was studied by scanning electron microscopy (SEM). Figure 4.6 shows a SEM image of a C-NiO sample deposited on to aluminium substrate. It can be seen that the coating is compact with round nano-pores and cavities. Figure 4.7 shows a cross section SEM image of a C-NiO coating which also shows round nano-pores on the cross section SEM image of a C-NiO coating which also shows round nano-pores on the cross section of the coating on an aluminium substrate. From these figures it can be deduced that the coatings consisted of a porous carbon and nickel oxide composite. This is illustrated schematically in figure 4.8 which depicts a schematic cross-sectional view of the coating. It is interesting to note that carbon is not necessarily sitting in the pores, contrary to expectations (see section 2.4). However, the presence of pores in the material is expected to enhance absorption through a multiple reflection and reflection phenomenon inside the pore. This is explained in section 4.4.3.

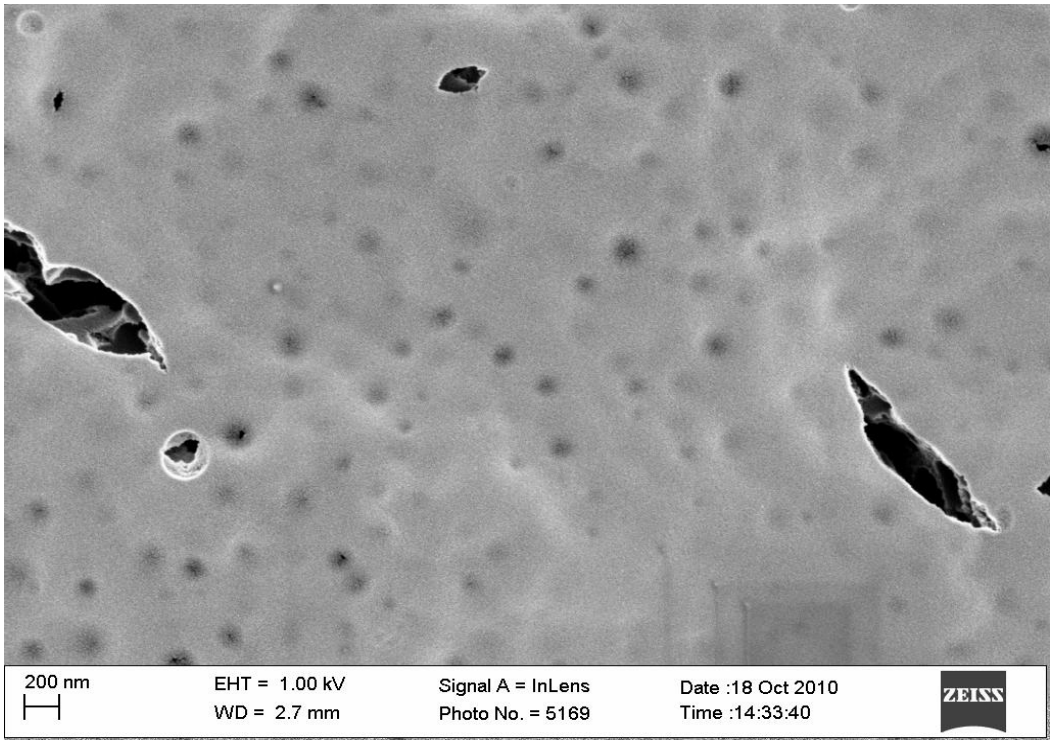

Figure 4.6: Scanning electron image of a C-NiO sample on aluminium substrate showing surface morphology. There are popped-up pores, un-popped-up pores as well as cracks on the surface.

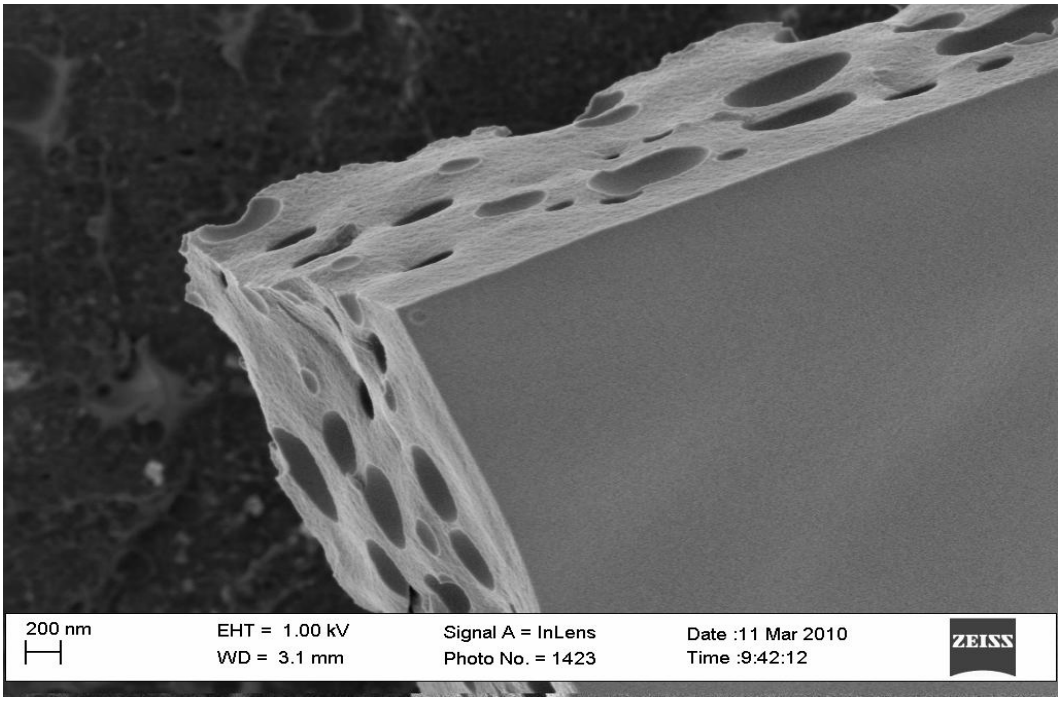

Figure 4.7: Scanning electron image of C-NiO coating on an aluminium substrate revealing pores on the cross section of C-NiO layer.

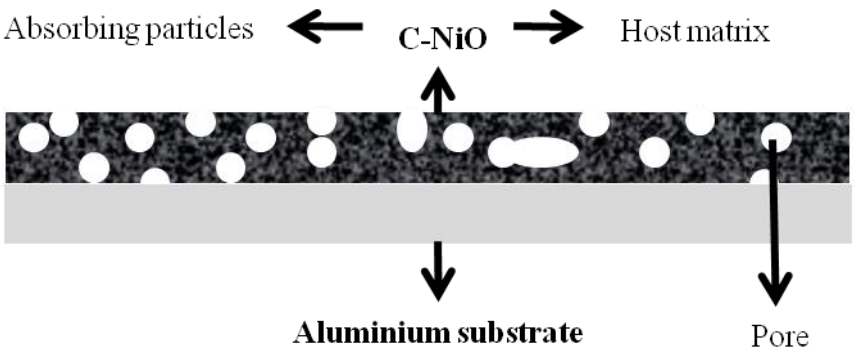

Figure 4.8: Schematic of a cross section of a porous C-NiO coating on an aluminium substrate.

4.4 Effect of sol-gel process parameters on C-NiO

4.4.1 Introduction

The main purpose of this study was to fabricate C-NiO solar absorber coatings with high photo-thermal conversion efficiency. The efficiecy is determined from the optical properties i.e. solar absorptance (α_{sol}) and thermal emittance (ε_{therm}). The properties of the sol-gel fabricated materials depend on the fabrication process parameters used. Table 4.1 shows a set of base fabrication parameters used in this study. Some of these parameters (highlighted red)

Table 4.1: Base fabrication parameters used in this study

Ethanol (ml)	Ni(Ac) (g)	DEA (g)	PEG (g)	Sucrose (g)	Water (ml)	Temp (° C)	Speed (RPM)
50	7.5	6.3	1	8	8	450	3000

were varied in order to show their effect on the properties of the fabricated material. For the material investigated in this study the process parameters that were varied were heat treatment temperature, PEG content, carbon precursor (SUC) content and coating speed. A given parameter would be varied and its effect was being investigated while the rest of the parameters were kept constant. For each of the parameters investigated there were 10 samples per data point, making a total of 400 tests. For heat treatment temperature it was decided to investigate 150 °C below and 100 °C above the base parameter of 450 °C. Therefore the range chosen was 300-550 °C with an increment of 50 °C. For the investigation PEG effect, the range chosen with respect to base sol parameters was 0 g - 5 g with an increment of 1 g. It was difficult to dissolve PEG contents higher than 5 g. For the investigation of the effect of SUC content a range of 0 g – 16 g with an increment of 2 g was chosen. It was observed that it was difficult to handle SUC content above 16 g because it quickly formed precipitates and led to unstable sol. For coating speed investigation, a range of 1000 RPM – 8000 RPM with an increment of 1000 was chosen. This choice of range was determined by the speed limits of the spin coater model used.

4.4.2 Effect of heat treatment temperature

Figure 4.9 shows a graph of α_{sol} and ε_{therm} calculated using equations (1.13) and (1.14) respectively as function of heat treatment temperature. It can be seen from the figure that α_{sol} increases with an increase in temperature from 300 °C to 450 °C. A further increase in temperature from 450 °C to 550 °C does not show a change in α_{sol} values. The ε_{therm} stabilises at around a value 0.1 with an outlier at 350 °C.

The change in optical properties as a function of heat treatment temperature observed above can be explained in terms of chemical composition and evolution of carbon as the heat treatment temperature changes. Therefore results from UV-Vis and IR reflectance and Raman techniques were used to explain the change. Figure 4.10 shows typical reflectance spectra of

C-NiO coatings heat treated at different temperatures. The dashed line is a reflectance of an ideal selective solar absorber. The reflectance of C-NiO decreases with increase in temperature in the UV-Vis range indicating an increase in the absorptance in this range due to an increase in the content of light absorbing element (carbon). This is evident from the fact that the darkness of the samples increases with an increase in temperature (see figure 4.11). This explains an increase in α_{sol} in the range between 300 °C and 450 °C. No significant change is observed between the samples heat treated at 450 °C and 550 °C. The reflectance increases with an increase in heat treatment temperature in the infrared range due to degradation of infrared active (absorbing) species (bands in the spectra between 6 μm and 7 μm attributed to OH vibrations [4.7, 4.8]) in the coating resulting in a 'purer' carbon containing NiO matrix as temperature increases hence ε_{therm} tends to be stable at low values at high treatment temperature. Thermo-gravimetric analysis of the precursor sol (section 4.1) showed that the thermal decomposition of these sols stabilise at around 430 °C. One would expect the sample at 300 °C to have a high emittance as the one at 350 °C because they both suffer from infrared absorption. The sample at 300 °C though suffering from infrared absorption has fairly high reflectance as its absorption edge is found at shorter wavelengths. This is due to the fact that its carbon content is low. This will be explained by Raman studies below.

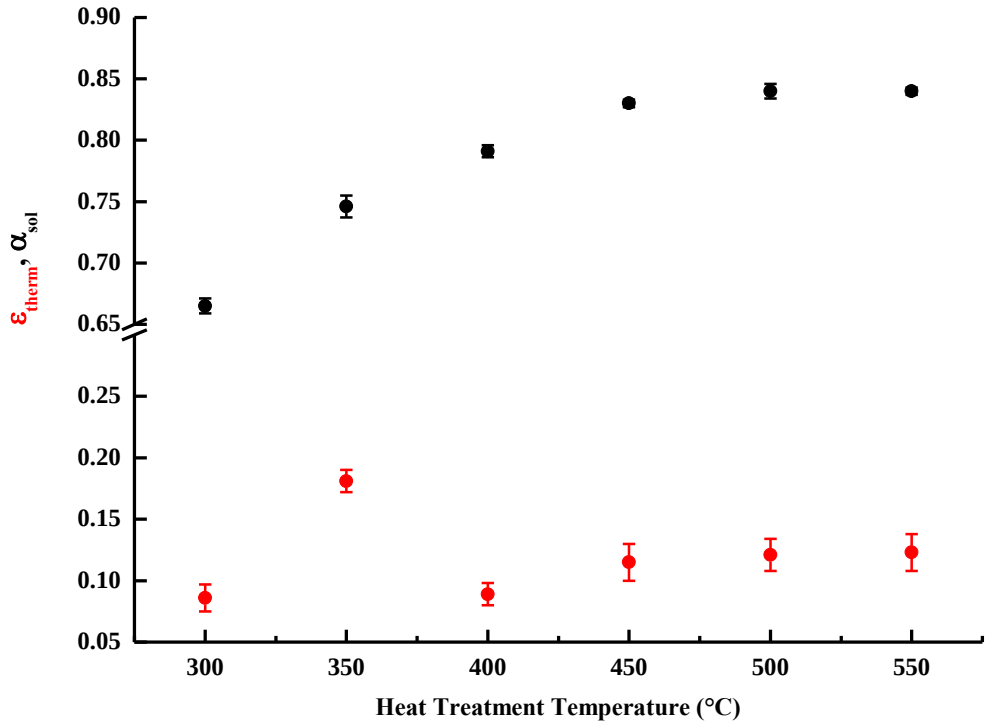

Figure 4.9: α_{sol} and ε_{therm} as function of heat treatment temperature of the precursor sol.

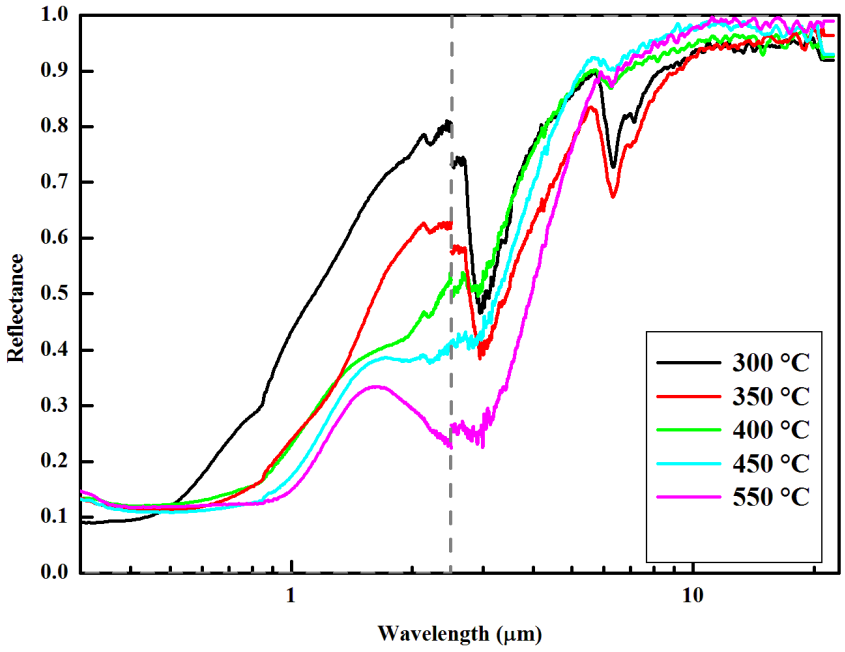

Figure 4.10: Typical reflectance spectra in the UV-Vis to far infra-red range for C-NiO coatings heat treated at different temperatures. The dashed line is a reflectance of an ideal selective solar absorber.

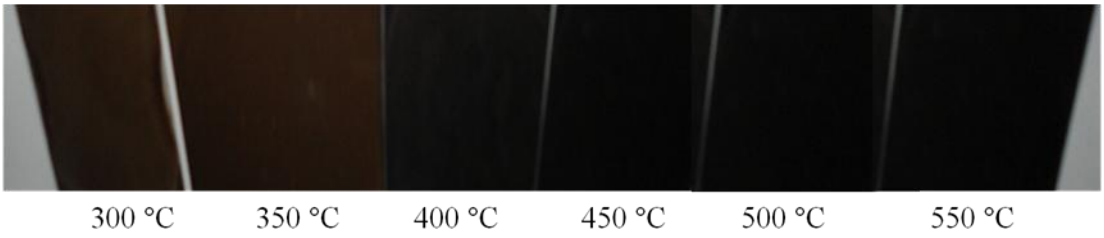

Figure 4.11: Optical images of samples heat treated at different temperatures showing an increase in the darkness with increase in heat treatment temperature.

The Raman technique was used in order to study the evolution of carbon in the C-NiO coatings as a function of temperature. Figure 4.12 shows Raman spectra of coatings heat treated at different temperatures. The dashed vertical lines indicate positions of the D and G bands. The features of the Raman spectrum are commonly related to the nanometric scale structure of the carbon containing films [4.6, 4.9]. The following parameters were extracted from the Raman spectra in figure 4.12: the position (ω_i), width (Γ_i) and intensity (I_i) determined from the areas of the peaks of the D and G bands by Lorenzian fitting, while the mean size (L_a) of the graphitic nanocrystallite was estimated from the formula [4.10, 4.11]:

$$L_a \approx 44\left[I_D / I_G\right] nm\,. \qquad (4.1)$$

The variation of the above mentioned parameters with heat treatment temperature of the C-NiO coatings is presented in table 4.2. The mean size of graphitic nanocrystallites is comparable for all heat treatment temperatures above 300 °C. There is no clear trend in terms of the position (ω_D) and width (Γ_D) of the D band with increase in heat treatment temperature. However, there is a progressive shift towards higher frequencies in terms of position (ω_G) and width (Γ_G) narrowing for G band. The shift towards higher frequencies of position (ω_G) and width (Γ_G) narrowing for G band is an indication of increase of the number and/ or size of the graphitic domain [4.6, 4.9]. This suggests a progressive increase of the graphitic domain in C-NiO coatings with an increase in heat treatment temperature. This is in good agreement with the increase in darkness (figure 4.11) and improvement in optical properties (figure 4.9) of C-NiO coatings as the heat treatment temperature increases.

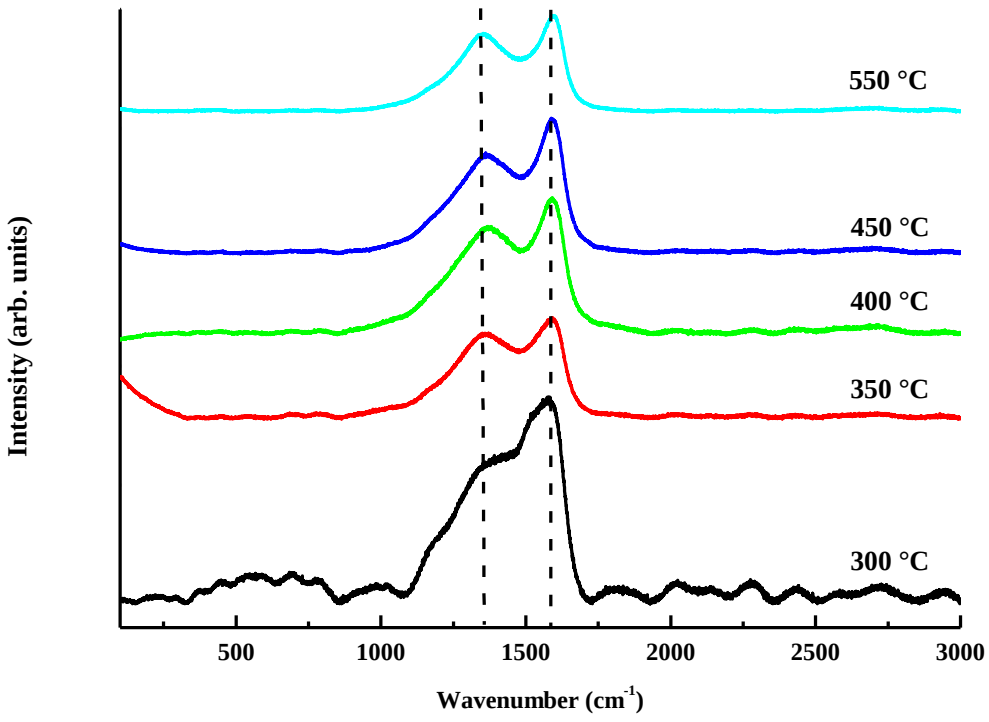

Figure 4.12: Raman spectra of C-NiO coatings heat treated at different temperatures. The dashed vertical lines indicate the positions of the Raman features at 1350 and 1580 cm^{-1}. The spectra are vertically shifted for clarity.

Table 4.2: Variation of C-NiO Raman parameters with heat treatment temperature.

Treatment temperature (°C)	ω_D (cm^{-1})	Γ_D (cm^{-1})	ω_G (cm^{-1})	Γ_G (cm^{-1})	I_D/I_G	L_a (nm)
300	1373.5	192	1579.7	467	0.4	18
350	1365.4	370	1587.4	122	3.5	154
400	1370.3	359	1591.3	111	3.2	143
450	1367.4	341	1588.7	91	3.5	154
550	1357	306	1590	87	3.4	150

Figure 4.13 shows a variation of photo-thermal conversion efficacy of the C-NiO coatings with heat treatment temperature for samples presented in figure 4.9. The efficiency for samples heat treated at 300 °C and 350 °C is low as compared to those at higher temperatures. The efficiency for samples at higher temperatures is comparable within reasonable error. The best heat treatment temperature in this series is found between 450 °C and 550 °C. A heat treatment of 450 °C would be recommended given the cost implications of heating at higher temperatures.

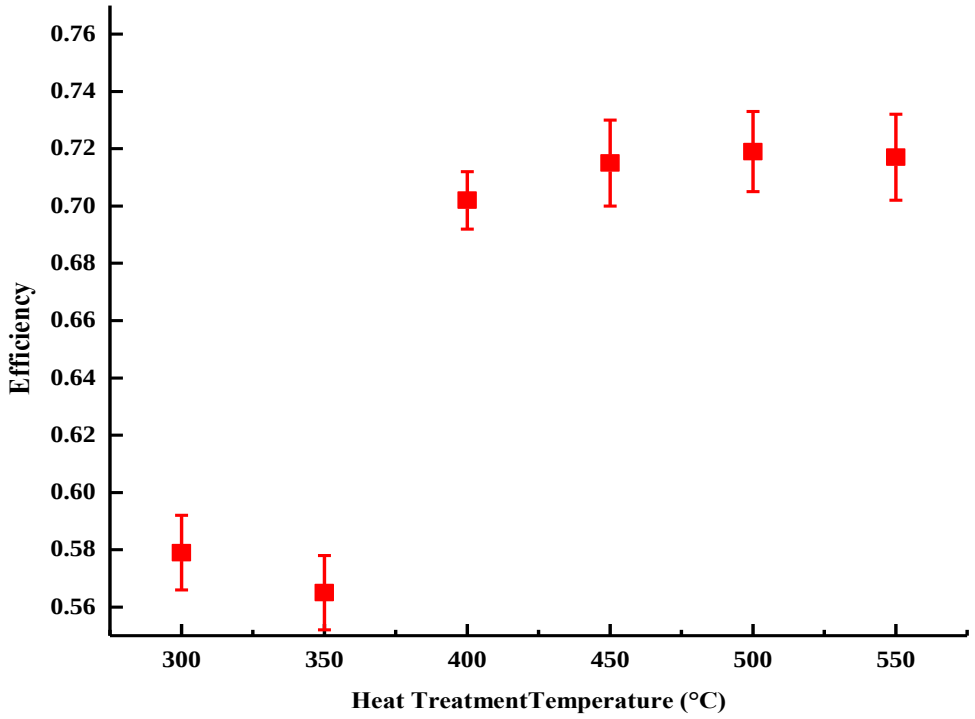

Figure 4.13: Variation of photo-thermal conversion efficiency with heat treatment temperature of coated films.

4.4.3 Effect of PEG content in the sol

Films that were formed from precursor sols with PEG as an additive were observed to have pores. According to Sun *et al* [4.12] a PEG molecule is a long zigzag chain structure. However, it will become a ring-network structure when it is dissolved in water. There is a similar change of the chain structure in ethanol. In the formed inorganic-organic network configuration of the precursor sol the PEG plays a role as the structure-directing agent [4.13]. Liu *et al* [4.14] fabricated porous zinc oxide thin films using a similar method as the one adopted in this study using PEG as a structure directing template. The mechanism for the formation of the pores is proposed in reference [4.15]. It is therefore expected that the porosity will affect the optical properties of the coatings investigated in this study. Figure 4.14 shows a graph of α_{sol} and ε_{therm} as function of the PEG content in the sol. The optical absorptance increases slightly with an increase in PEG content from 0 to 2 g PEG then visibly drops at 3 g and varies little onwards. The highest absorption was found at 2 g PEG content. The phenomenon observed in figure 4.14 can be explained in terms of the occurrence of pores on the samples and an increase in their size and density.

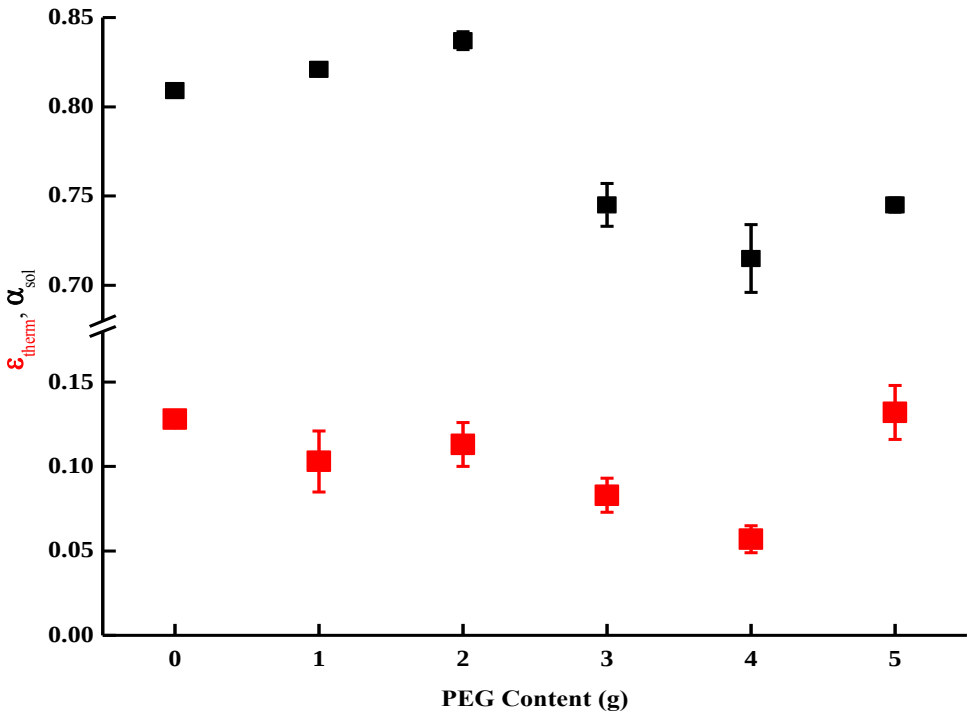

Figure 4.14: α_{sol} and ε_{therm} as function of the PEG content of the precursor sol.

Figure 4.15 shows SEM images of samples prepared from precursor sols with different PEG contents. The slight increase in absorptance from 0 g to 2 g (figure 4.14) is due to an increase in the number and size of pores as the PEG content increases. From figure 4.15 it can be observed that the film with 0 g PEG is compact while pore size and density increases as the

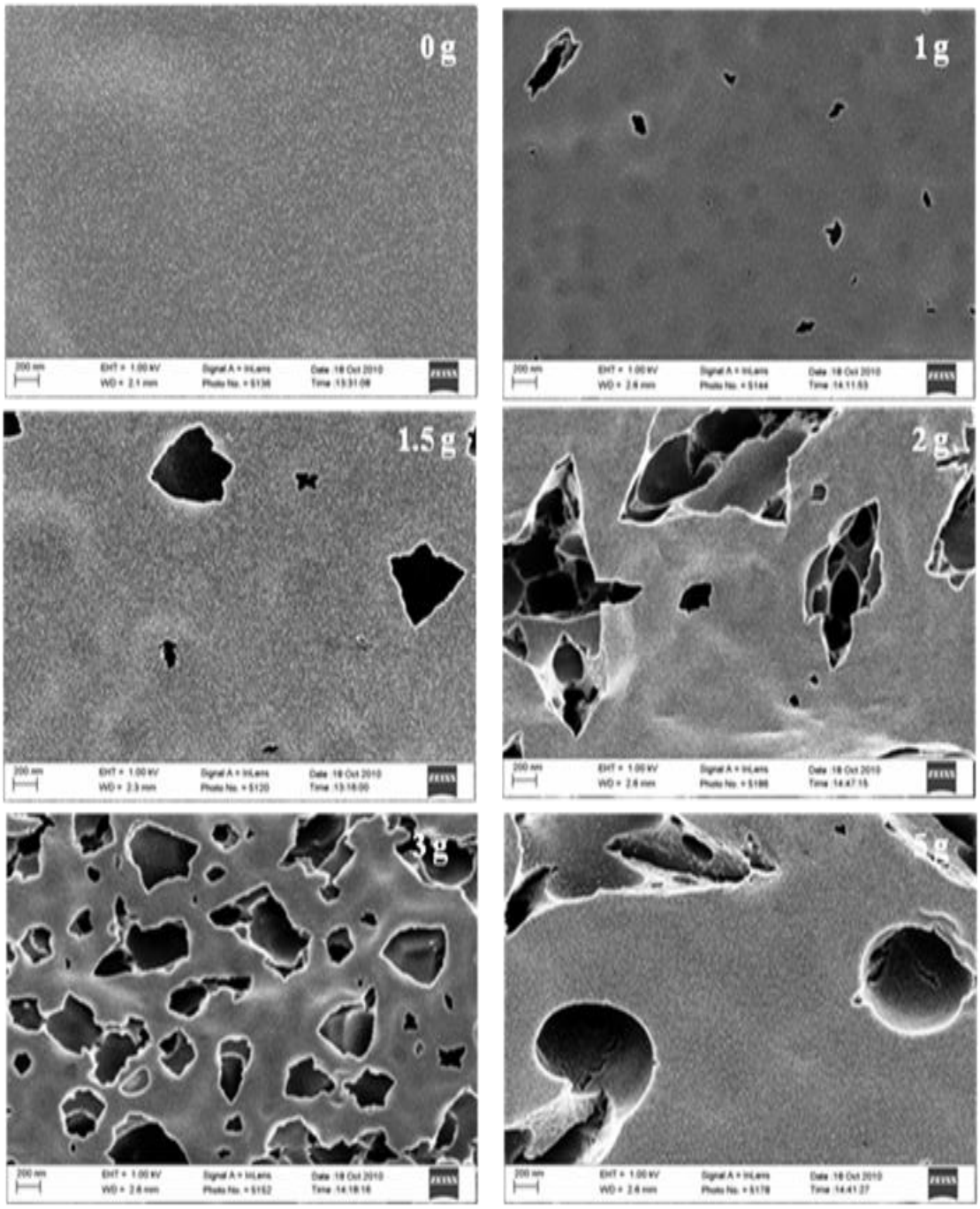

Figure 4.15: SEM images if samples prepared from precursor sols with different PEG contents showing an increase in pore size and density as the PEG increases

PEG content increases. Nano-pores cause multiple reflection of light inside the pore. On a non-porous absorber film, a light wave undergoes a mechanism known as normal absorption [4.16]. Whereas, for porous structures light waves can however be trapped by structural pores. This mechanism is known as multiple absorption [4.17, 4.18], and is depicted by figure 4.16. The reflected waves consecutively encounter the walls of the pores and enter into the absorber layer again. Under this circumstance, the light wave's energy is partially absorbed during each contact resulting in higher solar absorption. However if the pore size and density is too big then light absorption should drop. The visible drop in the absorptance values above a PEG of 2 g is due to the fact the pores are big and dense such that large part of the oncoming light gets reflected off the substrate and does not contribute to absorption by the absorber. This phenomenon is illustrated in figure 4.17.

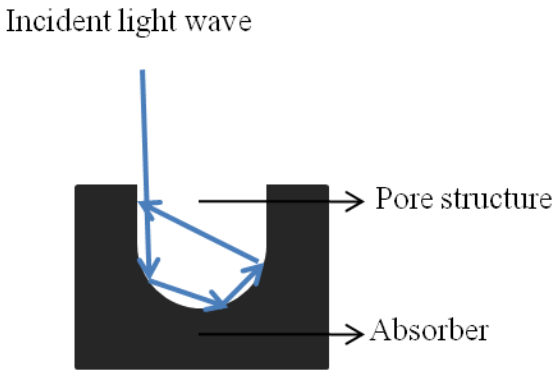

Figure 4.16: Schematic of multiple absorption of light within a structural pore of an absorber material.

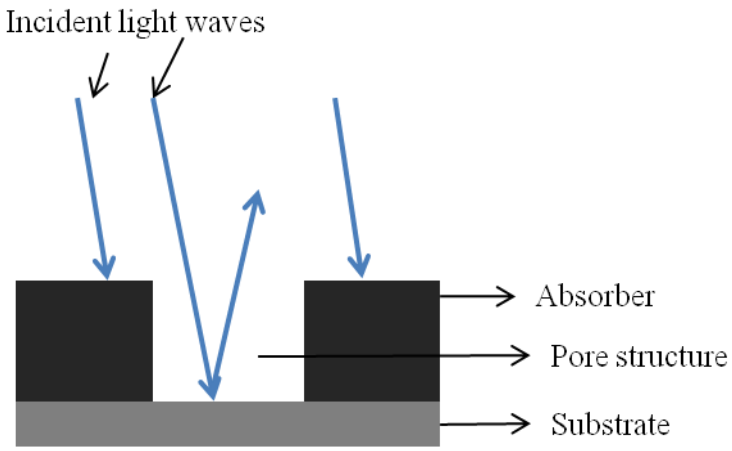

Figure 4.17: Schematic of light reflection off the substrate leading to reduced light absorption.

Figure 4.18 shows the variation of photo thermal conversion efficiency with PEG content for samples presented in figure 4.14. The efficiency increases with increase in PEG content from 0-2 g and drops with further increase in PEG content. PEG contributes only a fraction of the total cost of the sol and therefore given that an introduction of an amount of PEG (1 and 2 g) to the C-NiO precursor sol increases the absorber efficiency by 0.04 (4 %) use of PEG would be recommended. From figure 4.14 the PEG content that gave the highest efficiency was 1 g and 2 g. A PEG value between 1 and 2 g would therefore be recommended.

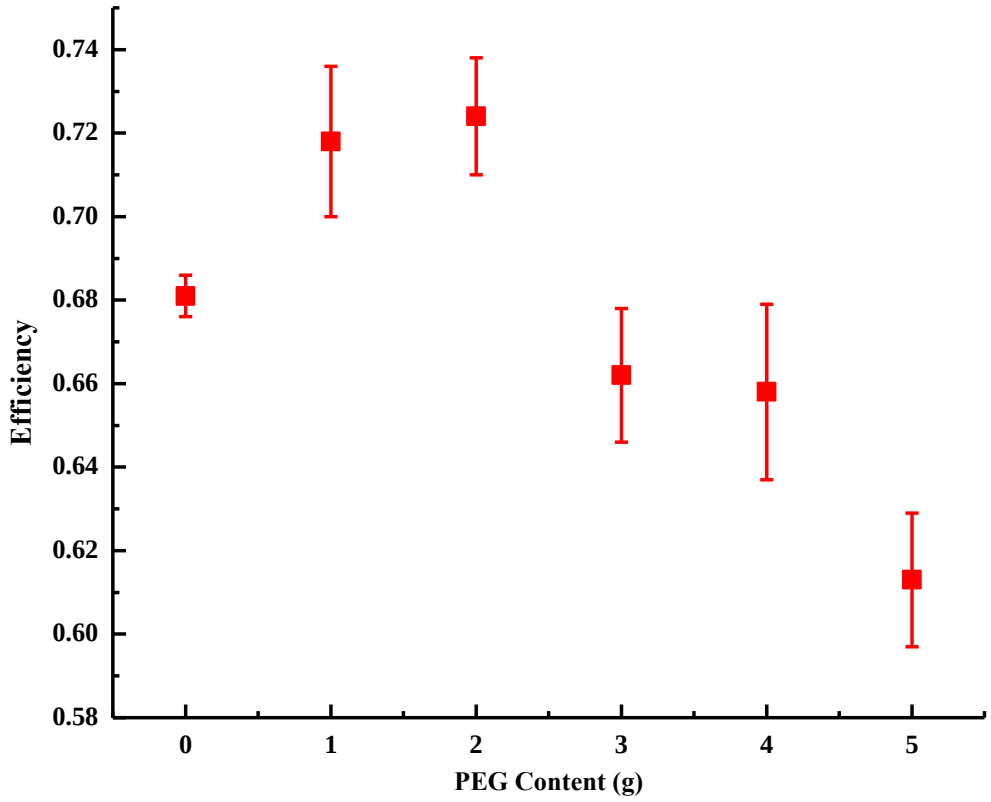

Figure 4.18: Variation of photo-thermal conversion efficacy with PEG content of the precursor sol for films heat treated at 450 °C.

4.4.4 Effect of Sucrose content

Figure 4.19 shows reflectance spectra of coatings heat treated in air to form quasi pure NiO with carbon deficiency, and the rest heat treated in nitrogen: 0, 8, 12 and 16 g SUC and a decant of 16 g SUC sol (sol left after the precipitation of solutes). The sample which was heat treated in air i.e. quasi pure NiO shows the highest reflectance in both the infra UV-Vis and IR range. The reflectance of samples with 0 to 12 g SUC content is similar in the UV-Vis

region. The absorption edge tends to move towards longer wavelengths for samples that contain SUC which could mean that they are slightly thicker than the ones that do not contain SUC. This is expected since the addition of SUC should result in increased viscosity of sols. It is observed that the samples that contain SUC tend to suffer from absorption in the infra red region and this is what affects their thermal emittance. This absorption found between 6 μm and 7 μm is due to O-H bending vibrations [4.7, 4.8].

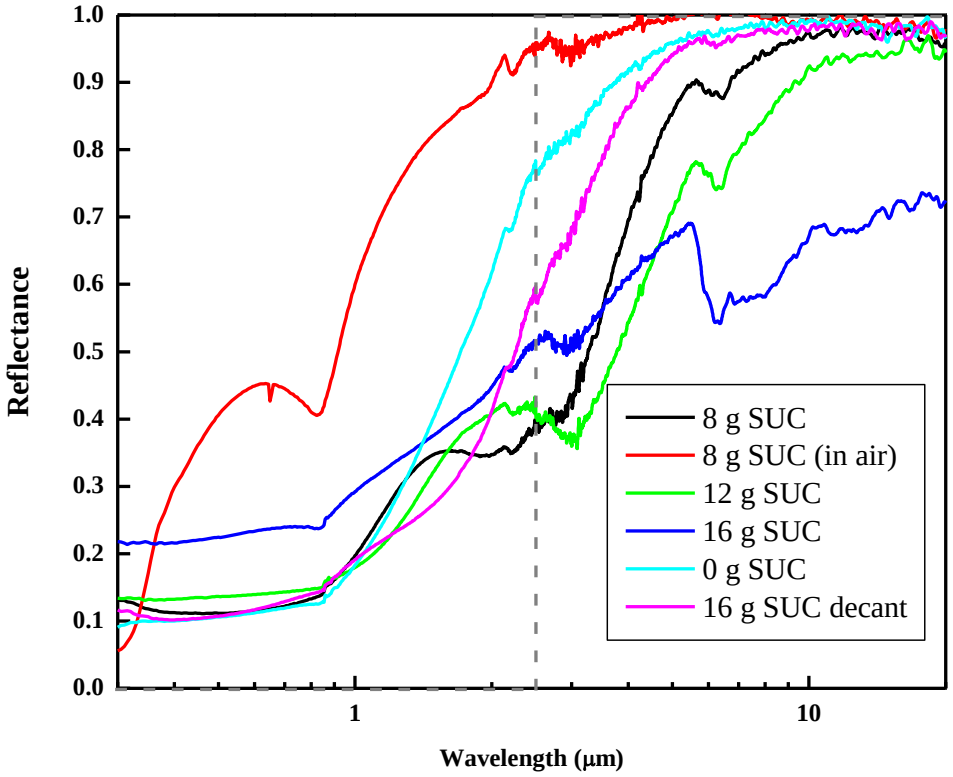

Figure 4.19: Reflectance spectra of coatings heat treated in air to form pure NiO, and the following heat treated in nitrogen: 0 g SUC, 8 g SUC, 12 g SUC and 16 g SUC and a decant of 16 g sol (sol left after the precipitation of solutes).

Figure 4.20 shows a graph for variation of α_{sol} and ε_{therm} with SUC variation. The SUC in the C-NiO coating is used to vary the amount of carbon since sugars are known to be good precursors (sources) of carbon [4.19]. Varying the SUC content in the solution can also change the viscosity and stability of the sol. The α_{sol} is generally stable at around 0.82 for SUC contents between 0 and 12 g and decreases at SUC contents above 12 g. The ε_{therm} is lower and is approximately 0.07 for 0 g SUC compared to higher SUC contents between 0 and 8 g where it is stable at around 0.12. From 10 g to higher SUC content ε_{therm} starts to increase.

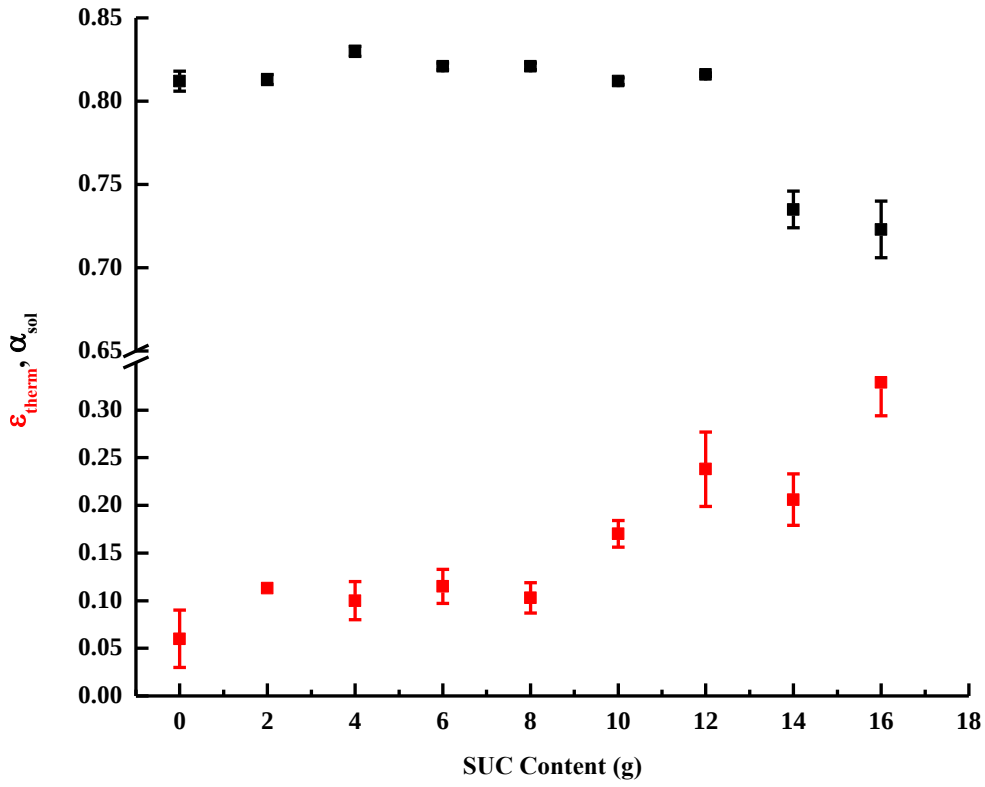

Figure 4.20: α_{sol} and ε_{therm} as a function of SUC variation with water fixed at 8 grams.

One would expect the addition of SUC to result in improved solar absorptance but this is not the case. As observed form figure 4.19 the reflectance of samples is similar in the UV-Vis range and the absorption edge moves towards longer wavelength with addition of SUC. This does not affect α_{sol} because it is a property determined by weighting the reflectance data against solar spectrum and the solar spectrum is most intense at 0.55 μm (see figure 1.3) than in the NIR region hence similarity in the absorptance properties.

The possible reason for change in optical properties after the addition of SUC content greater than 8 g is that at that stage the sol becomes unstable and difficult to spin coat. The change in the SUC content of the precursor sol below 8 g does not seem to have an effect on the optical properties of C-NiO absorber. The constituents of the sols used in this study are carbon based (organic and metal organic) and therefore it seems that their thermal decomposition forms a significant amount of carbon which then remains in the formed NiO matrix.

Quantitative analyses of carbon in the samples with 0 and 8 g SUC content was done in order to find out why the optical properties do not change when SUC is added. The surface composition of the composite materials has been quantitatively determined from scanning x-ray photoelectron spectroscopy (SXPS) analysis. The chemical compositions of C-NiO composite materials with 8 g SUC and without SUC in the precursor solution determined by the XPS are listed in tables 4.3 and 4.4, respectively.

The atomic concentration of carbon in the film with 8 g SUC is 68.6 % whereas the concentration of O is 19.8 % and that of Ni is 8 %. About 3.5 at % N is also found in the composite. This is from the N_2 gas used during heat treatment. For the film without sucrose the concentration of C is 60.1 % whereas the concentration of O is 27.0 % and that of Ni is 7 %. About 4.4 at. % N, and small amounts of impurities (1 at. % Na, and 0.7 at. % S) which could be from mishandling of the sample is also determined from the measurement. These SXPS results show that the difference in the amount of carbon between the sample containing 8 g SUC and the sample without SUC is 8.5 %. Therefore the carbon that is derived from SUC adds little impact in terms of optical properties because it does contribute very little to the final composite.

Table 4.3: Chemical composition of C-NiO composite surfaces with 8 g sucrose from XPS.

Sample	**Element**	**Atomic concentration (%)**	**Binding Energy (eV)**	**Probable bonds/Compounds**
C-NiO composite with 8 g sucrose	C	68.6	284.8 (83.1 %) 286.6 (11.8%) 287.6 (1.5 %) 287.0 (3.7 %)	C-(C,H) C-O C=O O-C=O
	O	19.8	529.6 (22.3 %) 531.9 (77.7 %)	NiO O-(C,H)
	Ni	8.0	854.2	O-(C,H)
	N	3.5	400.1	N

Table 4.4: Chemical composition of C-NiO composite surfaces without sucrose from XPS.

Sample	Element	Atomic concentration (%)	Binding Energy (eV)	Probable bonds/Compounds
C-NiO composite without sucrose	C	60.1	284.8 (73.8 %) 286.5 (13.7%) 287.5 (3.1 %) 288.6 (9.4 %)	C-(C,H) C-O C=O O-C=O
	O	27.0	529.6 (11.0 %) 531.9 (89.0 %)	NiO? O-(C,H,S);Ni_2O_3; $Ni(OH)_2$
	Ni	7.0	855.9	Ni_2O_3; $Ni(OH)_2$
	N	4.2	399.8	N-(C,H,O)
	Na	1.0	1071.8	Na
	S	0.7	168.9	S-(Ni,Na,O)

Figure 4.21 shows variation of photo-thermal conversion efficiency with SUC content. It can be seen from the figure that the photo-thermal conversion efficiency values from 0 g to 8 g SUC contents are comparable within experimental error and they deteriorate with further

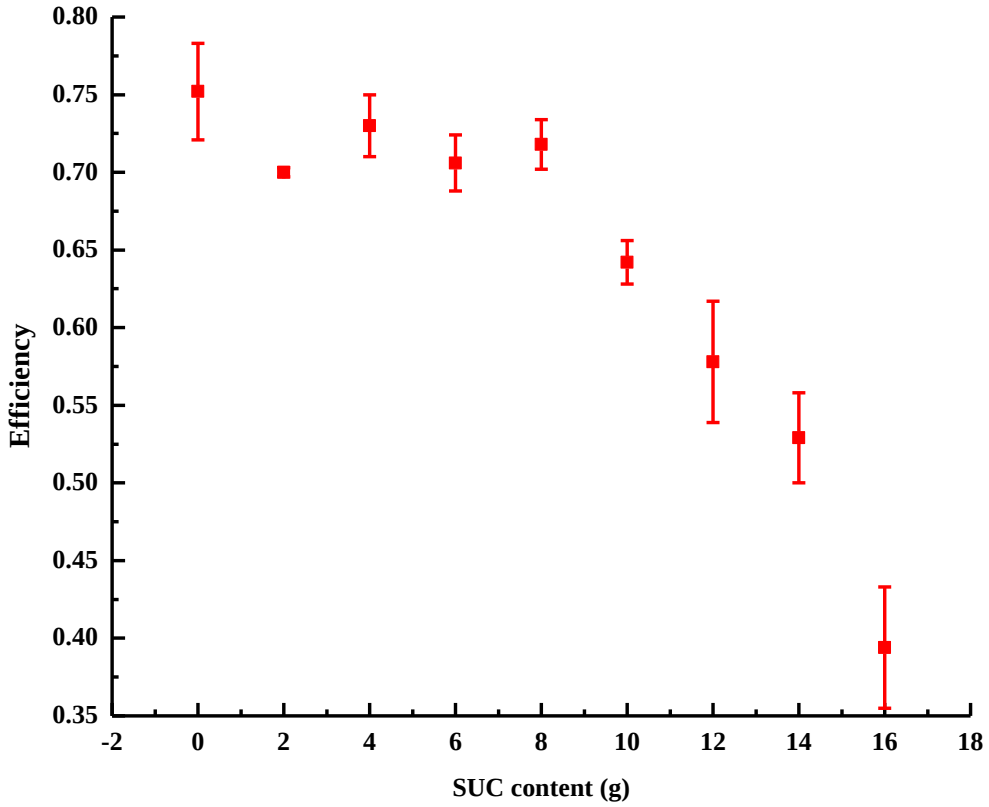

Figure 4.21: Variation of photo-thermal conversion efficiency of C-NiO coatings with sucrose content of the sol. Also included is results for decant of the precipitated sol which contained 16 g SUC.

increase in SUC content. At high SUC content the sols become unstable and results in the formation of sugar precipitate. A SUC content of 0 g would therefore be recommended. When a decant of the precipitated sols was spin coated at 3000 RPM and heat treated at 450 °C α_{sol} and ε_{therm} values of as much as 0.84 and 0.05 respectively were obtained. The UV-Vis and infrared reflectance of a typical such sample is presented in figure 4.19. The photo-thermal conversion efficacy for these samples is 0.790±0.010. This is the best efficacy achieved in this study.

4.4.5 Effect of spin coating speed

Figure 4.22 shows a graph of α_{sol} and ε_{therm} as a function of spin coater speed. The absorptance is generally constant except for the two outlier points at 5000 and 6000 RPM. The thermal emittance values decrease with increase in coating speed at speeds between 1000 and 5000 RPM then slightly increase from 6000 to 8000 RPM.

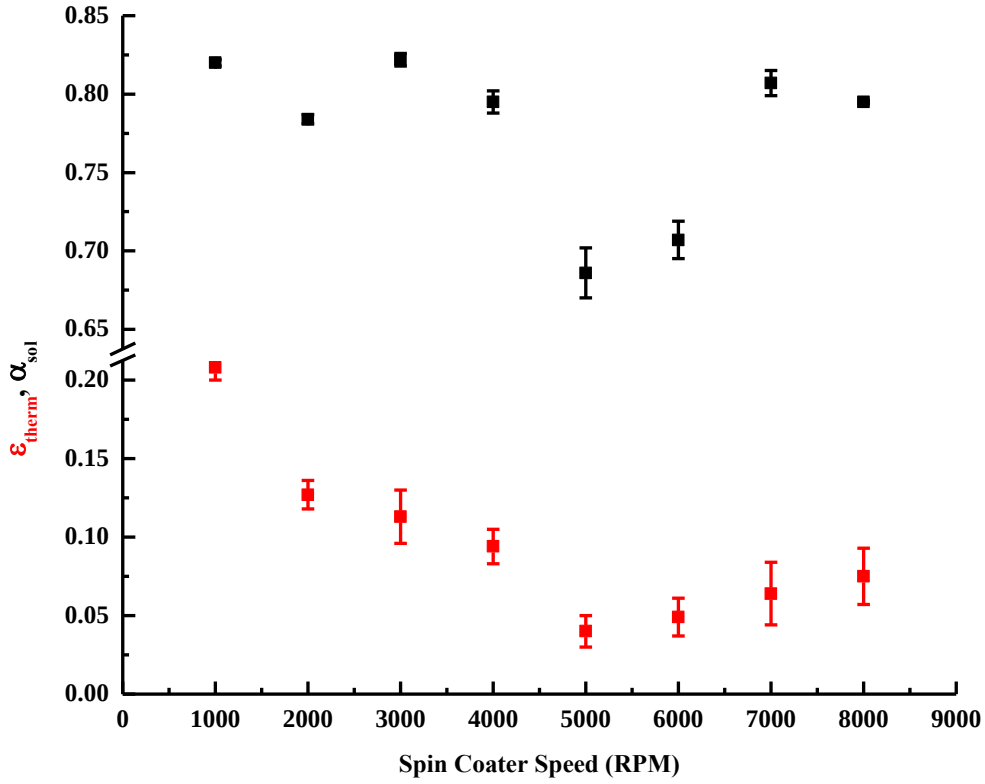

Figure 4.22: α_{sol} and ε_{therm} as a function of spin coater speed.

One would expect the optical absorptance to decrease with an increase in coating speed because an increase in spin coater speed results in decrease of the coating thickness [4.20]. However, this is not the case. One has to bear in mind that the coating speed of the spin coater also affects the drying process of the precursor sol with volatile solvents during the coating stage. This is because the drying of the coated film affects its flow on the substrate and may prevent further thinning of the coated film thus causing unexpected properties at different speeds.

Figure 4.23 shows the variation of photo-thermal conversion efficiency with spin coater speed for samples presented in figure 4.22. The photo-thermal conversion efficiency generally increases with an increase in coating speed and the highest efficiency is found at 7000 RPM.

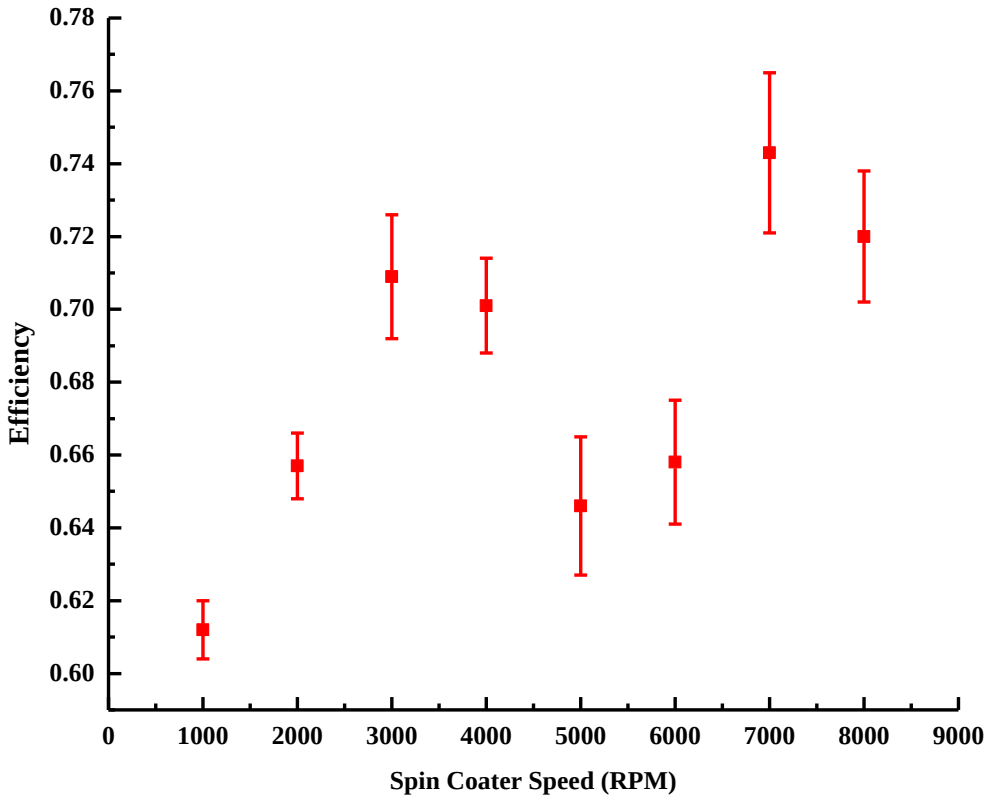

Figure 4.23: Variation of photo-thermal conversion efficiency of C-NiO coatings coated at different spin coater speeds.

4.4.6 Summary of optical results

Figure 4.24 shows a graph of absorptance against emittance for samples fabricated in this study showing how the absorptance and emittance combinations scattered. Other coatings are included for comparison. The quadrants were formed from a rule of thumb that a good selective absorber should have a solar absorptance of at least 0.8 and a thermal emittance of

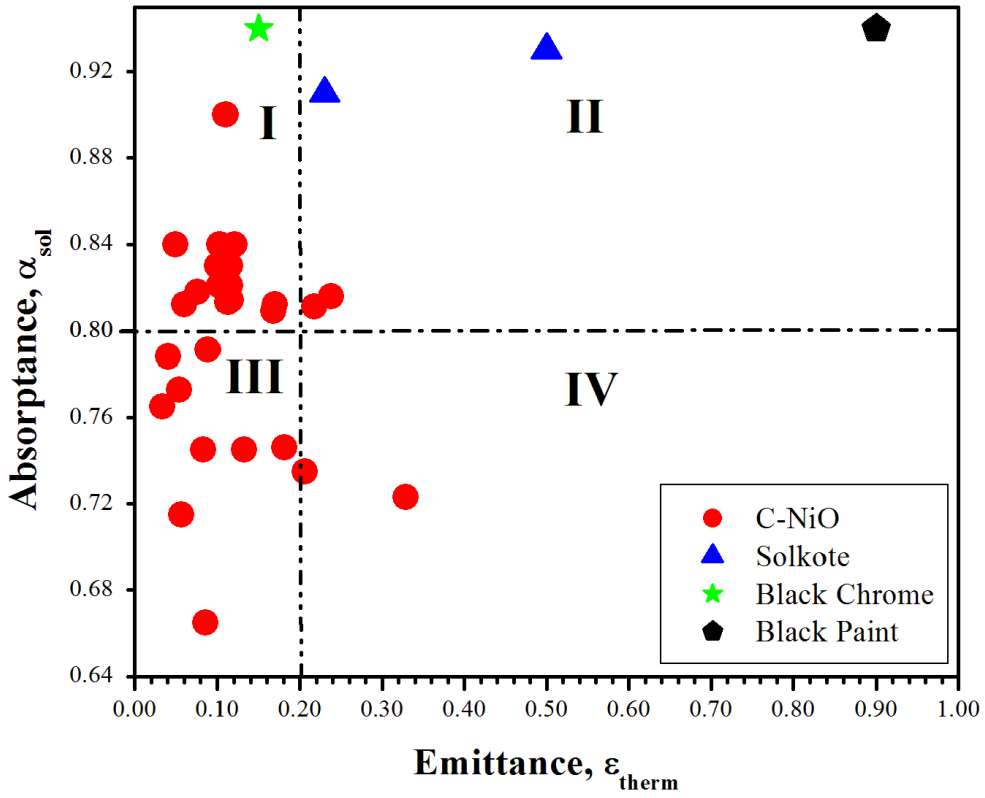

Figure 4.24: Scatter graph of absorptance and emittance for representative C-NiO samples used in this study. Other coatings are included for comparison.

less than 0.2. An efficient solar absorber should have absorptance values that are as close to 1 as possible while having emittance values as close to 0 as possible. Such absorbers fall into quadrant I of the graph shown in figure 4.24. From figure 4.24 it can be seen that the upper limit of solar absorptance for sol gel fabricated C-NiO in this study is 0.90 while the lower limit is 0.65. The upper limit of thermal emittance is 0.35 while the lower limit is 0.05. The sample that had the best combination of absorptance and emittance and thus the best photo-thermal conversion efficiency had an average absorptance of 0.81 and an average thermal emittance of 0.06 giving a photo-thermal conversion efficiency of 0.75. These optical properties compare well with the optimal Ni-Al_2O_3 sample of similar design as samples in this study fabricated by Bostrom [4.20] using the sol-gel technique on rough aluminium

substrates. The sol-gel fabrication parameters for best samples in this study are given in table 4.5. These parameters are comparable to the base fabrication parameters chosen in table 4.1 with the exception of SUC content parameter which is 0 g. An added advantage of this choice of parameters is that the sols prepared using these parameters (particularly 0 g SUC) are stable i.e. they do not form precipitates.

Table 4.5: Fabrication parameters for the samples with highest average efficiency.

Ethanol (ml)	Ni(Ac) (g)	DEA (g)	PEG (g)	Sucrose (g)	Water (ml)	Temp (° C)	Speed (RPM)
50	7.5	6.3	1	0	8	450	3000

The photo-thermal conversion efficiency of the coating fabricated with parameters presented in table 4.5 above was compared to widely used non-selective (black matt paint), selective (Solkote) and highly selective (black chrome) coatings in the South African solar thermal industry for water heating. The comparison was done by measuring their optical properties (α_{sol} and ε_{therm}) and the results are presented in Table 4.6.

Table 4.6: Comparison of optical properties and photo-thermal conversion efficiency for various solar absorber coatings.

Sample	α_{sol}	ε_{therm}	$\eta = \alpha_{sol}-\varepsilon_{therm}$
C-NiO	0.81±0.01	0.06 ±0.03	0.75±0.03
Black matt Paint (non-elective)	0.94	0.90	0.04
Solkote (selective)	0.93	0.25	0.68
Black chrome (highly selective)	0.93	0.15	0.78

Compared to black matt paint coating which is a non-selective absorber, the efficiency of the best C-NiO composite found in this study exceeds by far. Although a black paint coating has

very high absorptance, it also has very high emittance which makes it highly inefficient. The best coating found in this study showed photo-thermal conversion efficiency which is better than Solkote. Although Solkote has a desirably higher absorptance of up to 0.93 compared to the best C-NiO in this study (0.81) it also suffers from high thermal emittance. Of the three coatings compared with best C-NiO coating in table 4.6, black chrome has the highest photo-thermal conversion efficiency. The problem with black chrome is its higher cost compared to other coatings listed in table 4.6 (see table 4.7).

4.5 Cost estimations

The cost per square meter of C-NiO absorber coatings was calculated assuming a thickness of 1 μm and compared to other solar absorber technologies used in South Africa and another potential sol-gel derived coating (nickel-alumina). These costs are presented in table 4.7. The cost is given in cost/m^2 of the solution and heat treatment where applicable and excludes the cost of the substrate.

Table 4.7: Cost estimations for C-NiO coating compared with other wildly used coatings also included is the cost estimation of another sol-gel derived coating. The values are given in cost/m^2.

Coating	**cost/m^2**
Coating	cost/m^2
C-NiO	~R 0.50
Solkote	~R 12
Black Paint	~R 4
Black Chrome	~R 20
Nickel-Alumina [4.21]	~R 1.50

The cost/m^2 for C-NiO is relatively low compared to other widely used technologies. Nickel-Alumina [4.21] another sol derived technology is projected to cost relatively low proving that the so-gel route is a relatively cheap fabrication process for selective solar absorbers. It must be remembered though that the all the cost displayed above are a very small fraction of the total cost of the whole solar collector.

References

[4.1] M. Richard, *The 100 most important chemical compounds: a reference guide. Westport, Conn: Greenwood Press,* (2007). ISBN: 9780313337581.

[4.2] http://scifun.chem.wisc.edu/chemweek/pdf/ethanol.pdf. Accessed 07-03-2011.

[4.3] J. Lin and S. Shan, K. Wei, *J. of Polymer degrade. and stabil.* **70** (2000) 171.

[4.4] J. Read, D. Foster, J. Wolfenstine and W. Behl, *J. power sources* **96** (2001) 277.

[4.5] P. Gabbott, *principles and Application of Thermal analysis*, *Wiley and sons*, (2008). ISBN: 0470698128.

[4.6] R.O Dillon, J.A Woolman, and V. Katkanat, *Phys. Rev*. B. **29** (1984) 3482.

[4.7] A.V. Rao, R.R. Kalesh, and G.M. Pajonk, *J. Mater. Sci.* **38** (2003) 4407.

[4.8] G. Katumba, J. Lu, L. Olumekor, G. Westin, and E. Wäckelgård, *J. Sol-Gel Sci. and Tech.* **36** (2005) 33.

[4.9] G. Mariotto, F.L. Freire Jr. and C.A. Achete, *Thin Solid Films* **241** (1994) 225.

[4.10] A.C. Ferrai and J. Robertson, *Phys. Rev*. B **61** (2000) 1409.

[4.11] R.J. Nemanich and S.A. Solin, *Phys. Rev*. B **20** (1979) 392.

[4.12] J. Sun, Z. Li and W. Fan, *Chin. J. Chem. Phys*. **12** (1999) 570.

[4.13] K. Kajihara and T. Yao, *J. Sol–Gel Sci. Tech*. **19** (2000) 219.

[4.14] Z. Liu, Z. Jin, W. Li, and J. Qui, *Mater. Lett*. **59** (2005) 3620.

[4.15] Z. Liu, J. Li a, J. Ya, Y. Xin, and Z. Jin, *J. Mat. Lett*. **62** (2008) 1190.

[4.16] S. Zhao and E. Wackelgard, *Sol. Energy Mater. Sol. Cells* **90** (2006) 243.

[4.17] J.A. Duffie, W.A. Beckam, *Sol. Engineering of Thermal Processes, John Wiley and Sons*, New York, 1991. ISBN 0-471-51056-4.

[4.18] O.P. Agnihotri and B.K. Gupta, *Solar Selective Surfaces, John Wiley & Sons*, (1981). ISBN 0471060356.

[4.19] Y. Mastai, S. Polarz, and M.S. Antonietti, *J. Adv. Funct. Mater*. **3** (2002) 12.

[4.20] T. Bostrom, *DPhil Uppsala University* (2006).

[4.21] T. Bostrom, E. Wackelgard and G. Westin, *J. Sol Energy* **74** (2003) 497–503.

CHAPTER 5 : CONCLUSIONS AND FUTURE WORK

5.1 Conclusions

In the present work a simple and cheap way of preparing spectrally selective solar absorber coatings was investigated, developed and optimized. The absorbing material consists of carbon nanoparticles embedded in a nickel oxide matrix. A sol-gel technique was used to deposit the coatings on aluminium substrates using a spin coater. The coatings were prepared from alcoholic sols based on Ni-acetate using diethanolamine as a chelating agent and polyethylene glycol (PEG) as an organic template. Sucrose was used as a carbon source. The impact of the sol-gel process parameters on the optical properties and photo-thermal conversion efficiency were systematically investigated.

Thermo-gravimetric analysis on the precursor sol showed that the weight loss of the precursor sol stabilizes at around 450 °C. This temperature was used for heat treatment of the samples during further optimization. The presence of nickel, oxygen, and carbon in the composite were confirmed by energy dispersive x-ray spectroscopy. Additional confirmation for the presence of carbon in the composite is found from the Raman signature of carbon. The surface morphology of the samples consisted of porous carbon-nickel oxide nano-composite.

The absorption and emission properties of the C-NiO nano-composite coatings were characterised by UV-Vis and FTIR spectrophotometers. The solar absorptance increased with the increase in heat treatment temperature from 300 – 450 °C and stayed constant with further increase in temperature to 550 °C. Raman measurements suggest a progressive graphitization of the composite films, with graphitic nano-clusters increasing in size and/or number with heat treating temperature. The thermal emittance is found to be the same in the temperature range studied.

It is found that the films without PEG are compact and the film become porous with increase in average size of the pores as the PEG concentration increases. The solar absorption increases with addition of PEG up to 2 g in the sol due to an increase in the number and size of pores as the PEG content increases which results in multiple reflection of light inside the pores. Further increase in PEG concentration above 2 g resulted in the drop of the absorptance values due an increase in size and density of the pores in which the large part of the oncoming light gets reflected off the substrate and does not contribute to absorption. No clear trend is observed when the coating speed is varied.

It was found that sucrose does not change the optical properties. This is because sucrose does contribute very little to the composite as verified by SXPS analysis. This suggests that most of the carbon in the composite is from the carbon in the precursor materials used in the preparation of the composite.

The best thermal conversion efficiency of the C-NiO composite coating in this study is found to be 0.75 ± 0.03. This is a very competitive result for selective solar absorbers especially when compared to commercially available paints found in the market in South Africa.

For a solar thermal technology to be more accessible in places such as rural parts of Africa where the majority of the people are poor and still depend on traditional forms of energy such as fire wood, the cost of the production of the absorbers should decrease significantly. Thus, the results discussed in this work highlight a novel approach of using simple and cost-effective deposition technique for future possible use as solar absorbers in solar collectors. Adaptation of this technique to large-scale production could ultimately assist in addressing the energy challenges in developing countries.

5.2 Future work

Although this study focused on the optimization of the sol-gel process parameters, there are still some outstanding work that needs to be done in order to successfully develop this C-NiO material for solar absorber applications. The following work is recommended as future outlook to this study:

- To study the long term durability of this C-NiO material.
- To optimise process parameters to meet a combination of durability and thermal conversion efficiency requirements.
- To adapt this technology to large scale coating techniques. This can be achieved by adapting this sol-gel technology to existing large scale coating techniques such as spray coating.